

MULTIPLE INVERSE-DIFFUSION FLAME SYNTHESIS OF
CARBON NANOMATERIALS

by

NASIR K. MEMON

A Dissertation submitted to the
Graduate School-New Brunswick
Rutgers, The State University of New Jersey
in partial fulfillment of the requirements

for the degree of

Doctor of Philosophy

Graduate Program in Mechanical and Aerospace Engineering

written under the direction of

Professor Stephen D. Tse

and approved by

New Brunswick, New Jersey

October, 2012

ABSTRACT OF THE DISSERTATION

Multiple Inverse-Diffusion Flame Synthesis of Carbon Nanomaterials

By NASIR K. MEMON

Dissertation Director:

Professor Stephen D. Tse

Carbon nanomaterials exhibit many remarkable electrical and physical properties. An ongoing challenge associated with specific novel carbon nanomaterials, such as graphene, is the development of large-scale production methods at low cost. The broad objective of this work is to investigate flame synthesis of carbon nanomaterials, specifically graphene and carbon nanotubes (CNTs), using open-atmosphere processing, with an eye towards scalability. An experimental study using a novel setup, based on multiple inverse-diffusion flames is undertaken to investigate the direct flame-synthesis of CNTs and graphene on metal substrates.

Few-layer graphene (FLG) is grown on copper and nickel substrates at high rates using the novel flame-synthesis burner. Substrate material (i.e. copper, nickel, cobalt, iron, and copper-nickel alloy), along with its temperature and hydrogen pretreatment, strongly impacts the quality and uniformity of the graphene films. The growth of FLG occurs in the temperature range 750-950°C for copper and 600-850°C for nickel and cobalt. For iron, the growth of graphene is not exclusively observed.

CNT growth is observed on a number of substrates. Transitional growth between CNTs and graphene films occurs on nickel and nickel alloys, depending on composition and temperature. For nickel, copper-nickel, nitinol, and Inconel substrates, CNTs grow at 500°C. The transitional growth to few-layer graphene is observed on nickel, copper-nickel and Inconel by changing the substrate temperature to 850°C. The growth of graphene is not observed on nitinol for the examined experimental conditions.

The growth of few-layer graphene films and CNTs are also investigated using various metal-oxide spinels as catalysts. The growth of CNTs is examined on NiAl_2O_4 , CoAl_2O_4 and ZnFe_2O_4 using counterflow diffusion flame and multiple inverse-diffusion flames, while the growth of graphene is examined on CuFe_2O_4 using multiple inverse-diffusion flames.

Finally, the growth of CNTs and iron oxide is studied on stainless steel. At low temperatures (500°C) the growth of $\alpha\text{-Fe}_2\text{O}_3$ is observed, while at higher temperatures (850°C) the growth of CNTs is observed. Additionally, by following a two-step growth process, where the temperature is changed from 500°C to 850°C, the growth of CNTs and $\gamma\text{-Fe}_2\text{O}_3$ occurs.

Preface

Much of the content in Chapters 4, 5, 6, 7, and 8 is verbatim from published or soon to be submitted for publication papers [1-4]; and I have obtained permission from the co-authors to include them in my thesis. Additionally, other chapters have wording similar to or identical to that found in the papers referenced below.

References

- [1] Memon, N., Tse, S., Al-Sharab, J., Yamaguchi, H., Goncalves, A., Kear, B., Jaluria, Y., Andrei, E., and Chhowalla, M., "Flame Synthesis of Graphene Films in Open Environments," *Carbon*, 2011; 49(15):5064–70.
- [2] Memon, N., Kear, B., Chhowalla, M., and Tse, S., "Role of Substrate, Temperature, and Hydrogen on the Flame Synthesis of Graphene Films" submitted to *Proceedings of the Combustion Institute*.
- [3] Memon, N., A., Kear, B., Tse, S., "Transitioning Growth from Carbon Nanotubes to Graphene Films on Nickel Alloys in Open-Atmosphere Flame Synthesis," manuscript in preparation.
- [4] Memon, N., Dunham, S., Xu F., A., Kear, B., Tse, S., "Flame Synthesis of Carbon Nanotubes and Graphene Films using Metal-Oxide Spinel," manuscript in preparation.

Acknowledgements

I would like to express my sincere thanks to my two MAE advisors, Professor Stephen Tse and Professor Yogesh Jaluria, and to my IGERT co-advisor, Professor Manish Chhowalla. Dr. Tse's knowledge, intelligence, and creativity provided me with a rich and productive graduate experience. I thank him for allowing me to explore my research in a collaborative environment, which motivated me to work at a higher level. I am also very fortunate to have Dr. Jaluria as an advisor. In addition to his expert advice, I am very thankful for the guidance and encouragement he gave me since I joined Rutgers as a Masters student. I owe a great deal to Dr. Chhowalla, who, in addition to providing fundamental advice and expertise throughout my doctoral work, broadened my mind to the impact of research and how to make ideas leap from lab to life. I also owe thanks to Professor Jerry Shan and Professor Bernard Kear for their assistance in my research work.

My sincere thanks are due to the numerous people who helped me through my research work. Firstly, I would like to thank Dr. Jafar Al-Sharab for all his counseling and his assistance with TEM. I would also like to thank Hadi Halim, Jonathan Doyle, and Zhizhong Dong for being excellent lab mates, I really appreciate all the support you guys gave me. I also want to thank Dr. Gang Xiong, whom I greatly benefited from, even though we worked together for only a few months. Finally, I want to thank John Petrowski for his assistance in building my experimental setup.

I am extremely thankful to the NSF-IGERT program (Grant 0903661, Nanotechnology for Clean Energy IGERT) for providing me with two years of financial

support and the chance to learn from disciplines outside my research area. Special thanks are due to Dr. Johanna Bernstein for managing the IGERT. I also want to thank the MAE department for supporting me as a teaching assistant prior to the IGERT. Finally this work was also supported by the ARO (Grant W911NF-08-1-0417), and the ONR (Grant N00014-08-1-1029).

I am also extremely thankful to my family for supporting me in my decision to leave my job to become a graduate student. Thank you Mom and Dad for your endless support and encouragement as I pursued my dreams. Special thanks to my wife, who never wavered in her support of me. Also, I would like to thank my two little boys for helping me get my mind off research. Most importantly, I am grateful to God for all the blessings He has bestowed on me.

Table of Contents

ABSTRACT OF THE DISSERTATION	ii
Preface.....	iv
Acknowledgements.....	v
Lists of tables	xii
List of illustrations	xiv
1. Introduction.....	1
1.1 Motivation	2
1.2 Research Innovation and Direction	3
1.3 Research Objective.....	4
1.4 Approach	7
1.5 Outline of this dissertation	8
1.6 References	8
2. Literature Review.....	9
2.1 Introduction	9
2.2 Graphene Background.....	11
2.2.1 Graphene structure and properties	11
2.2.2 Graphene synthesis	17
2.3. Carbon Nanotube Background.....	29
2.3.1 Carbon Nanotubes structure and properties.....	29
2.3.2 CNT Synthesis	31

2.4	Applications of Graphene and Carbon Nanotubes	34
2.4.1	Sensors	34
2.4.2	Transparent Conductive Films	35
2.4.3	Clean energy devices	37
2.4.4	Field effect transistor	39
2.5	Flame Synthesis.....	43
2.5.1	Flame Synthesis of CNTs	43
2.5.2	Flame Synthesis of Graphene	51
2.5.3	Scalable Flame Synthesis of Metal Oxides.....	53
2.6	Summary	53
2.7	References	54
3.	Experimental Setup.....	63
3.1	Multiple Inverse-Diffusion Burner Setup	63
3.2	Thermocouple (TC) and its coating	66
3.3	Experimental procedures.....	66
3.4	Numerical Techniques.....	66
3.5	Sample Preparation	66
3.6	Characterization techniques	67
3.6.1	Raman spectroscopy	68
3.6.2	X-ray photoelectron spectroscopy (XPS)	71

3.6.3 Atomic Force Microscopy (AFM)	73
3.6.4 Field-Emission Scanning Electron Microscopy (FESEM)	73
3.7 References	75
4. Structure, Property, and Thickness of Graphene Films Prepared Using Open Atmosphere Flame Synthesis.....	76
4.1 Introduction	76
4.2 Experiment	79
4.3 Results and Discussion.....	81
4.3.1 Flame Synthesis of FLG on Cu.....	81
4.3.2 Flame Synthesis of FLG on Ni	86
4.4 Concluding Remarks	91
4.5 References	91
5. Role of Substrate, Temperature, and Hydrogen on the Flame Synthesis of Graphene Films	94
5.1 Introduction	94
5.2 Experimental Procedure	97
5.3 Results and Discussion.....	97
5.3.1 Effect of substrate material	97
5.3.2 Effect of substrate temperature	103
5.3.3 Effect of hydrogen	106

5.4	Concluding Remarks	108
6.	CNT Synthesis on Transitional Metal Alloys	112
6.1	Introduction	112
6.2	Experimental Setup	114
6.3	Results and Discussion.....	114
6.4	Concluding Remarks	118
6.5	References	119
7.	Transitioning Growth from CNTs to Graphene Films on Nickel Alloys	121
7.1	Introduction	121
7.2	Experiment	122
7.3	Results and Discussion.....	123
7.4	Concluding Remarks	129
7.5	References	130
8.	Synthesis of CNTs and Graphene Films using Metal-Oxide Spinel.....	132
8.1	Introduction	132
8.2	Experiment	135
8.2.1	Spinel preparation.....	135
8.2.2	Spinel coating onto the support substrates	136
8.2.3	Flame setup	137
8.2.4	Characterizations of the spinels, as-grown CNTs and FLG	138

8.3	Results and Discussion.....	139
8.3.1	XRD analysis of as-prepared spinels	139
8.3.2	CNT Synthesis	139
8.3.3	Graphene Synthesis.....	145
8.4	Concluding Remarks	148
8.5	References	149
9.	CNT and Iron Oxide Flame Synthesis on Stainless Steel.....	153
9.1	Introduction	153
9.2	Experiment	154
9.3	Results and Discussion.....	156
9.3.1	High Temperature Growth on Stainless-Steel	156
9.3.2	Low Temperature Growth on Stainless-Steel	158
9.3.3	Two-step Growth Process on Stainless-Steel	161
9.4	Concluding Remarks	163
9.5	References	163
10.	Concluding Remarks.....	166
10.1	Summary of results and conclusion.....	166
10.2	Suggestions for future work	171
10.3	References	173
	Curriculum Vita	174

Lists of tables

Table 2.1 Chronology and Development of Carbon (reproduced from [3]).	10
Table 2.2 Mechanical properties of graphene (reproduced with caption from [11]).	14
Table 2.3 Thermal conductivity of graphene and graphene oxide based materials (reproduced with caption from [11]).....	16
Table 2.4 Summary of CVD conditions reported in the literature to grow graphene on copper (reproduced with caption from [38]).....	27
Table 2.5 Comparison of sheet resistances of graphene based transparent conductive films (reproduced with caption from [74]).	36
Table 2.6 Comparison of sheet resistances from SWNT based transparent conductive films (reproduced with caption from [74]).	37
Table 2.7 Comparison of the EDLCs based on different carbon materials (reproduced with caption from [78]).....	38
Table 2.8 Thermal conductivity enhancement in nanocarbon composites (reproduced with caption from [22]).....	41
Table 2.9 Summary of different flame configurations used for CNT synthesis (reproduced from [62]).	50
Table 3.1 List of substrates investigated.	67
Table 3.2 List of characterization techniques.....	67
Table 5.1 Properties of the different metals and alloys examined as substrates for graphene growth.....	95
Table 6.1 Catalytic metal alloys investigated.....	114

Table 9.1 Applications, compositions and functions of CNTs-oxides hybrid materials	
[8].	154

List of illustrations

Figure 1.1 General approach used for nanomaterial synthesis	7
Figure 2.1 Various forms of pure carbon (reproduced from [2]).....	9
Figure 2.2 Monte Carlo simulation of rippled graphene. The arrows are ~8 nm long (reproduced with caption from [4]).....	11
Figure 2.3 Bandgap in graphene devices. Schematic diagrams of the lattice structure of monolayer (a) and bilayer (b) graphene. The green and red colored lattice sites indicate the A (A1/A2) and B (B1/B2) atoms of monolayer (bilayer) graphene, respectively. The diagrams represent the calculated energy dispersion relations in the low-energy regime, and show that monolayer and bilayer graphene are zero-gap semiconductors (for bilayer graphene, a pair of higher-energy bands is also present, not shown in the diagram). (c) When an electric field (E_{\perp}) is applied perpendicular to the bilayer, a bandgap is opened in bilayer graphene, whose size (2Δ) is tunable by the electric field (reproduced with caption from [6]).	13
Figure 2.4 (A) Measured four-probe resistivity as a function of gate voltage before (blue) and after (red) current annealing; data from traditional high-mobility device on the substrate (gray dotted line) shown for comparison. The gate voltage is limited to ± 5 V range to avoid mechanical collapse. (B) Mobility as a function of carrier density n for the same devices. (C) AFM image of the setup before the measurements (reproduced with caption from [10,11]).....	13
Figure 2.5 (a) Photograph of a 50- μm aperture partially covered by graphene and its bilayer. The line scan profile shows the intensity of transmitted white light along the yellow line. Inset shows the sample design: a 20- μm thick metal support structure has	

apertures 20, 30, and 50 μm in diameter with graphene flakes deposited over them;	
(b) Optical image of graphene flakes with one, two, three, and four layers on a 285-nm thick SiO_2 -on-Si substrate (reproduced with caption from [17-19]).	15
Figure 2.6 Thermal conductivity measurement of graphene using Raman spectroscopy (reproduced with caption from [22]).	16
Figure 2.7 Mechanical exfoliation of graphene using scotch tape from HOPG (reproduced with caption from [11]).	17
Figure 2.8 (A) Photograph of a centrifuge tube following the first iteration of density gradient ultracentrifugation (DGU). The concentrated graphene was diluted by a factor of 40 to ensure that all graphene bands could be clearly resolved in the photograph. Lines mark the positions of the sorted graphene fractions within the centrifuge tube. (B and C) Representative AFM images of graphene deposited using fractions f4 (B) and f16 (C) onto SiO_2 . (D) Height profile of regions marked in panels B (blue curve) and C (red curve) demonstrating the different thicknesses of graphene flakes obtained from different DGU fractions (reproduced with caption from [11,30]).	18
Figure 2.9 Illustration on the preparation of reduced graphene oxide (reproduced with caption from [35]).	19
Figure 2.10 a) Schematic of the roll-based production of graphene films grown on a copper foil. The process includes adhesion of polymer supports, copper etching (rinsing) and dry transfer-printing on a target substrate. A wet-chemical doping can be carried out using a setup similar to that used for etching. (a) Roll-to-roll transfer of graphene films from a thermal release tape to a PET film at 120°C . (c) A transparent	

ultralarge-area graphene film transferred on a 35-in. PET sheet. (d) An assembled graphene/PET touch panel showing outstanding flexibility (reproduced with caption from [11,43]).....	21
Figure 2.11 Schematic illustrating the three main stages of graphene growth on copper by CVD: (a) copper foil with native oxide; (b) the exposure of the copper foil to CH_4/H_2 atmosphere at 1000 °C leading to the nucleation of graphene islands; (c) enlargement of the graphene flakes with different lattice orientations (reproduced with caption from [38]).....	22
Figure 2.12 Binary phase diagrams of transition metals and carbon. (a) Ni–C; (b) Co–C; (c) Fe–C; (d) Cu–C. The low carbon solubility in Cu, of ~0.008 weight % at ~1084 °C is highlighted in the inset of panel (d) (reproduced with caption from [38]).	23
Figure 2.13 Typical optical microscopy images, SEM images, and Raman spectroscopy of MLG and FLG grown on Ni (a-c), Fe (d-f), Co(g-i), and Cu (j-l) foil substrates using ethylene as the carbon source at 975°C. The growth time was 3 min, and the gas mixing ratio of $\text{C}_2\text{H}_4/\text{H}_2$ was 5/500, and the cooling rate was 60 °C min ⁻¹ . (a, d, g, and j). Optical microscope images of graphene. (b, e, h, and k) SEM images of graphene. (c, f, i, and l) Raman spectroscopy of graphene. Cu substrate background was subtracted. The spectra were normalized with the G-band (reproduced with caption from [44]).....	24
Figure 2.14 Schematic illustration of CVD growth of graphene and its transfer process (reproduced with caption from [47]).....	28
Figure 2.15 Schematic honeycomb structure of a graphene sheet. Carbon atoms are at the vertices. SWNTs can be formed by folding the sheet along lattice vectors. The two	

basis vectors a_1 and a_2 , and several examples of the lattice vectors are shown (reproduced with caption from [55]).....	29
Figure 2.16 Schematic structures of SWNTs (a) A (10,10) arm-chair nanotube (metallic nanotube). (b) A (12, 0) zigzag nanotube. (A small band gap can develop due to the curvature of the nanotube.) (c) The (14, 0) zigzag tube is semiconducting. (d) A (7, 16) tube is semiconducting. This figure illustrates the extreme sensitivity of nanotube electronic structures to the diameter and chirality of nanotube (reproduced with caption from [55]).....	30
Figure 2.17 Methods currently applied for the growth of CNTs: (a) the arc-discharge method; (b) the pulsed laser vaporization method; (c) the chemical vapor deposition method (reproduced with caption from [62]).....	33
Figure 2.18 (a) Schematic of a graphene gas sensor device. (b) Evolution of I_{ds} - V_{gs} curves with the exposure to NH_3 of the graphene for different durations (reproduced with caption from [17]).....	35
Figure 2.19 Transmittance versus sheet resistance for graphene based on production strategies: triangles, CVD; blue rhombuses, micromechanical cleavage (MC); red rhombuses, organic synthesis from polyaromatic hydrocarbons (PAHs); dots, liquid-phase exfoliation (LPE) of pristine graphene; and stars, reduced graphene oxide (RGO). A theoretical line as for equation is also plotted for comparison (reproduced with caption from [32]).....	36
Figure 2.20 Charge/discharge cycle performances of (a) graphite, (b) graphene, (c) graphene + CNT, and (d) graphene + C_{60} at a current density of 0.05 A g^{-1} (reproduced with caption from [78,79]).....	39

Figure 2.21 (a) Illustration depicting a graphene sheet as a chemically inert diffusion barrier. (b) Photograph showing graphene coated (upper) and uncoated (lower) penny after H_2O_2 treatment (30%, 2 min). (c) Photographs of Cu and Cu/ Ni foil with and without graphene coating taken before and after annealing in air (200 °C, 4 h) (reproduced with caption from [86]).....	42
Figure 2.22 Premixed, Normal Diffusion, Inverse Diffusion, and Counter-flow Diffusion Burner Setups.....	43
Figure 2.23 Flame profile of an over-ventilated and under-ventilated flame.	44
Figure 2.24 FESEM images of CNT morphology corresponding to catalytic probe composition (column) and flame sampling height (row). The alloy probes are operated at floating potential mode (FPM) for a 10 min sampling duration (reproduced with caption from [97]).....	47
Figure 2.25 Schematic of the flame synthesis of FLG on a nickel foil (reproduced from [113]).....	52
Figure 3.1 Schematic of the multiple inverse-diffusion flame.	64
Figure 3.2 Top-view of the multiple inverse-diffusion flame.....	64
Figure 3.3 Schematic diagram of the experimental setup involving the use of a multiple-inverse diffusion flame. (MFC stands for mass flow controller).....	65
Figure 3.4. a) Illustration of energy transitions leading to Rayleigh, stokes and anti-stokes spectra. b) Schematic Raman scattering spectrum showing Rayleigh line, Stokes and Anti- Stokes Raman scattering (reproduced with caption from [1,2]).....	68
Figure 3.5 Raman spectra of the different types of sp^2 carbon forms (reproduced with caption from [3]).	70

Figure 3.6 (a) Comparison of Raman spectra at 514 nm for bulk graphite and graphene. (b) Evolution of the spectra at 514 nm with the number of layers. (c) Evolution of the Raman spectra at 633 nm with the number of layers (reproduced with caption from [4]).....	70
Figure 3.7 Basic component of an XPS system (reproduced from [5]).....	72
Figure 3.8 Comparison between the C 1s XPS spectra of graphite and those of the amorphous carbon films (reproduced with caption from [6]).....	72
Figure 3.9 Correlation between the AFM height and number of graphene layers (reproduced with caption from [7]).....	73
Figure 3.10 Schematic diagram of a transmission electron microscope [8].	74
Figure 4.1 Multiple inverse-diffusion flames provide hydrogen and carbon-rich species suitable for growth of graphene and other carbon nanomaterials.	79
Figure 4.2 Few-layer graphene (FLG) film grown by flame synthesis on Cu. (a) Photograph of a 1cm x 1cm film transferred onto quartz. (b) Optical microscope image of the FLG transferred onto a Si substrate with a 300nm oxide layer and the corresponding AFM image and height profile of the FLG transferred on SiO ₂ /Si substrate. (c) Two-dimensional mapping of the Raman I _G /I _{2D} over a 12μm x 12 μm area. (d) Raman spectrum of the FLG on SiO ₂ /Si.	83
Figure 4.3 (a) UV-vis spectrum of the FLG transferred onto a quartz substrate. (b) XPS C 1s spectrum of the FLG shows that the oxygen contamination is minimal and is comparable to CVD grown graphene. The inset shows the XPS spectra of the film.	84

Figure 4.4 Analysis of the influence of temperature on the growth of FLG on Cu, showing variation in Raman I_{2D}/I_G as a function of gas phase temperature. The inset shows atypical Raman spectrum observed at lower temperatures.....	86
Figure 4.5 Few-layer graphene film grown by flame synthesis on Ni. a) Raman spectrum of the FLG on Ni. b) HRTEM image of the FLG. The bottom right inset shows the electron diffraction pattern of the graphene sheet, illustrating the well-defined crystalline structure. The top left inset shows resolution magnified image of the graphitic lattice.....	87
Figure 4.6. XPS C 1s spectrum of the FLG on Ni.	88
Figure 4.7 Investigation of the temperature and methane concentration on the growth of FLG on Ni. a) Temperature = 850°C, CH ₄ :H ₂ = 1:10. b) Temperature = 950°C, CH ₄ :H ₂ = 1:10. c) Raman spectra showing the 2D peak at a constant temperature of 950°C.	89
Figure 4.8 Raman mappings of the 2D peak over a 12 μm x 12 μm region at a constant CH ₄ :H ₂ ratio of 1:10. a) Raman mapping for Cu, illustrating that the growth of graphene is self-limiting to a few layers. b) Raman mapping for Ni, showing regions that correlate to more than 10 layers.....	90
Figure 5.1 Schematic of the experimental setup. Product species of multiple inverse-diffusion flames impinge on a metal substrate (i.e. Cu, Ni, Co, Fe, or Cu/Ni) growing graphene.....	96
Figure 5.2 Growth of few-layer graphene (FLG) film on Cu. (a) Raman spectrum of the film. (b) Photograph of the film transferred on quartz; the inset shows the film transferred onto a SiO ₂ /Si substrate.	99

Figure 5.3 Growth of few-layer graphene (FLG) film on Ni, Co, and Cu-Ni. (a) Raman spectra of the graphene films. (b) TEM image of the graphene film synthesized on Ni, with the inset showing the diffraction pattern.....	100
Figure 5.4 FESEM images comparing the growth of graphene on Cu and Ni. (a) Low magnification image of graphene film on Cu. (b) High magnification image of graphene film on Cu. (c) Low magnification image of graphene film on Ni. (d) High magnification image of graphene film on Ni.	101
Figure 5.5 Growth of a disordered graphitic structure on Fe. (a) Raman spectrum of the material. (b) Low magnification FESEM image of the material growth on Fe; the inset shows a high magnification image.	103
Figure 5.6 Analysis of the influence of temperature on the growth of graphene. (a) Raman spectrum on Cu. (b) Raman spectrum on Ni. (c) Raman spectrum on Co.	104
Figure 5.7 FESEM image showing the low-temperature (500°C) growth condition. (a) High magnification image on Ni. (b,c) Low magnification image on Cu-Ni. (d) High magnification image on Cu-Ni.....	106
Figure 5.8 (a) XPS core-level Cu 2p spectrum of the Cu foil before and after the growth of graphene. (b) Raman spectrum of the film with no H ₂ pretreatment (but H ₂ is used during the growth process) and no external H ₂ as fuel during the growth process (but H ₂ is used during the pretreatment process).	108
Figure 6.1 FESEM images of CNT morphology using a Fe substrate.	115
Figure 6.2 FESEM images of CNT morphology using a Ni/Cr/Fe substrate.	116
Figure 6.3 FESEM images of CNT morphology using a Ni/Ti substrate.....	117

Figure 6.4 Simulated SWNT bends. (a) A 34° bend from a pentagon and heptagon defect on opposite sides. (b) – (d) from three pentagon-heptagon defects on different sides. (e) A 8° bend from two fused defects. (f) A 4° bend from a fused defect. (Reproduced with citation [10])	118
Figure 7.1 Schematic diagram of the experimental setup. The substrate (Ni, Cu-Ni, Inconel, or nitinol) is held at a high temperature (850°C) or a low temperature (500°C).....	122
Figure 7.2 Carbon nanomaterial growth on Ni. (a) Raman spectrum of the few-layer graphene (FLG) synthesized on Ni at a temperature of 850°C. (b) HRTEM image of the FLG, the top right inset is magnified image of the graphene lattice. (c) SEM image of the FLG on Ni, the top right inset is a magnified image of Ni. No CNTs are observed. (d) CNTs grown on Ni at 500°C.	124
Figure 7.3 Raman spectrum showing the influence of temperature on the growth of FLG on Ni.....	125
Figure 7.4 Carbon nanomaterial growth on Cu-Ni. (a) Raman spectrum of the few-layer graphene (FLG) synthesized on Cu-Ni at a temperature of 850°C. (b) SEM image of the FLG on Cu-Ni. No CNTs are observed. (c) CNTs grown on Cu-Ni at 600°C. (d) CNTs grown on Cu-Ni at 500°C.....	127
Figure 7.5 Carbon nanomaterial growth on Inconel and nitinol. (a) Raman spectrum of the few-layer graphene (FLG) synthesized on Inconel at a temperature of 850°C. The top right inset is the SEM image of the FLG on Inconel. (b) Raman spectrum of the growth on nitinol at a temperature of 850°C. The top right inset is the SEM image showing the disorder structure on nitinol. (c) CNTs grown on Inconel at 500°C. (d)	

CNTs grown on nitinol at 500°C. (e) CNTs grown on Inconel without the addition of hydrogen as fuel. (f) CNTs grown on nitinol without the addition of hydrogen as fuel.	129
Figure 8.1 Schematic of the experimental setup (a) Counterflow diffusion flame (CDF) with a probe inserted for CNT growth. (b) Product species of multiple inverse-diffusion flames impinge on a substrate for CNT or graphene growth.	135
Figure 8.2 XRD patterns of as-prepared spinel solid solutions	138
Figure 8.3 CNT growth using NiAl_2O_4 and CoAl_2O_4 . (a) High magnification FESEM image of CNTs covering a single reduced NiAl_2O_4 grain. The top right inset shows a low magnification image of CNTs from NiAl_2O_4 . (b) High magnification FESEM image of CNTs covering a single reduced CoAl_2O_4 grain. The top right inset shows a low magnification image of CNTs from CoAl_2O_4 . (c) TEM image of CNTs from NiAl_2O_4 . (d) HRTEM image of a CNT from NiAl_2O_4 (adapted from [29]).	140
Figure 8.4 CNT growth using ZnFe_2O_4 . (a) High magnification FESEM image of CNTs covering reduced ZnFe_2O_4 grains. The top right inset shows a low magnification image. The bottom right inset shows larger diameter CNTs prepared from poorly crystallized ZnFe_2O_4 . (b) TEM images of CNTs from ZnFe_2O_4 . The right inset is a HRTEM image of a CNT. (c) Raman spectra of as-grown CNTs from ZnFe_2O_4 (adapted from [29]).	142
Figure 8.5 Growth of CNTs using the multiple inverse-diffusion flame. (a) Low magnification FESEM image on CoAl_2O_4 . The top right inset shows a high magnification image. (b) Low magnification FESEM image on NiAl_2O_4 . The top right inset shows a high magnification image. (c) Low magnification FESEM image	

on ZnFe_2O_4 . The top right inset shows a high magnification image. The top left inset shows the growth of no CNTs at a temperature of 500°C on ZnFe_2O_4	144
Figure 8.6 Growth of graphene using the multiple inverse-diffusion flame. (a) Raman spectrum of few-layer graphene (FLG) on Cu and CuFe_2O_4 coated on quartz. (b) FESEM image of the CuFe_2O_4 coated with graphene. The top right inset is a high magnification image.....	147
Figure 8.7 XPS C 1s spectrum of FLG synthesized using Cu foil and CuFe_2O_4	148
Figure 9.1 Schematic diagram of the experimental setup. The stainless steel substrate is held either at a high temperature (850°C) or a low temperature (500°C).....	155
Figure 9.2 Carbon nanomaterial growth on stainless steel at a temperature of 850°C . (a,b) SEM image of the growth of micro- and nano-scale carbon fibers and tubes. (c) The growth after CH_4 is introduced for 5 minutes (dark regions correspond to CNTs). (d) The growth after CH_4 is introduced for 20 minutes.	157
Figure 9.3 (a) Raman spectrum of the high temperature growth condition. (d) XPS spectrum of the of the high temperature growth condition.	158
Figure 9.4 Iron oxide growth on stainless steel at a temperature of 500°C . (a) SEM image shows the growth of a nanocrystalline iron-oxide film at 500°C . The top right inset shows a magnified SEM image of the film. The bottom right inset shows an optical image of the film. (b) Raman spectrum confirms the growth of $\alpha\text{-Fe}_2\text{O}_3$	159
Figure 9.5 (a) TEM image of the iron oxide nanoparticles. (b) SAED confirming the growth of $\alpha\text{-Fe}_2\text{O}_3$	160
Figure 9.6 (a) Fe 2p XPS spectrum of $\alpha\text{-Fe}_2\text{O}_3$. (b) Fe 2p XPS spectrum after argon ion beam etching.	161

Figure 9.7 Growth on stainless steel after a two-step growth process. (a) The growth of nanocrystalline iron oxide. (b) Hybrid growth of CNTs and iron oxide.	162
Figure 9.8 (a) Raman spectrum confirming the growth of γ -Fe ₂ O ₃ and CNTs. (b) TEM analysis of the γ -Fe ₂ O ₃ crystal. The top right inset shows a HRTEM image of γ -Fe ₂ O ₃	162

Chapter 1

1. Introduction

Flame synthesis is widely used to manufacture commercial quantities of nanoparticles. Of the most commonly used nanoparticles, i.e. carbon black, fumed silica, and titania, flame synthesis is the dominant technique in the production of these materials. Production volume of the flame synthesis industry is on the order of 100 metric tons per day [1].

A key advantage of flames is that it readily provides the high temperature necessary for gas phase synthesis. Additionally, flames can naturally provide a carbonizing or oxidizing environment. The scalability of flames has been demonstrated since World War II, when there was a high demand for carbon black due to the growing tire market [2]. Shortly after, flames were widely used in the production of fumed SiO_2 , TiO_2 , and Al_2O_3 , where chloride-based precursors are typically used to inject Si, Ti, or Al into the synthesizing flame. A similar process is currently utilized to synthesize SiO_2 - GeO_2 for the commercial manufacturing of light guides and optical fibers [2].

The importance of flame synthesis is apparent, as the technique continues to develop, being used currently in the production of advanced materials. While the flame synthesis of aerosol represents a major industry, limited progress has been reported in the extension of flames to a chemical vapor deposition (CVD)-type process. Such development could lead to a more scalable and robust method for the growth of nanomaterials on substrates and surfaces, e.g. as coatings.

1.1 Motivation

Carbon-based nanostructures and films define a new class of engineered materials that display remarkable physical, photonic, and electronic properties. Graphene is a monolayer of sp^2 -bonded carbon atoms in a two-dimensional (2-D) structure. This layer of atoms can be wrapped into 0-D fullerenes, rolled into 1-D nanotubes, or stacked as in 3-D graphite. Graphene and carbon nanotubes (CNTs) exhibit unique electronic and photonic properties, high thermal conductivity, and exceptional mechanical strength. Recently, the discovery of graphene by micro-cleaving has generated intensive experimental research into its fabrication. Production methods that currently exist include ultrahigh vacuum (UHV) annealing of SiC, and chemical vapor deposition (CVD). Common techniques for CNT fabrication include plasma-arc discharge, laser ablation, and CVD.

Although these methods have been met with some success, they are not readily or economically scalable for large-area applications or may be subject to batch-to-batch inconsistencies. Combustion synthesis has demonstrated a history of scalability and offers the potential for high-volume continuous production at reduced costs. In utilizing combustion, a portion of the hydrocarbon gas provides the elevated temperatures required, with the remaining fuel serving as the hydrocarbon reagent, thereby constituting an efficient source of both energy and hydrocarbon reactant. This can be especially important as the operating costs for producing advanced materials, especially in the semiconductor industry, far exceed the initial capital equipment costs. Various morphologies of CNTs, carbides, and semiconducting metal-oxide and carbide nanowires

have been produced using air-fuel combustion-based configurations, using both aerosol and supported-substrate methods.

The growth of these nanostructures and films over large areas remains especially challenging. Moreover, current processing methods can be complex, while still characterized by low growth rates and low total yield densities. Accordingly, it is evident that there is a strong need for better methods of synthesizing nanostructured materials, particularly carbon-based nanostructures.

1.2 Research Innovation and Direction

The unique synthesis configuration undertaken in this work is the multiple inverse-diffusion (non-premixed) flame burner, where the post-flame species are directed at a substrate to grow carbon nanomaterials. The burner operates in an inverse mode, where for each distinct flame in the planar array, oxidizer is in the center, and fuel (e.g. H_2 , CH_4) surrounds it. The hydrocarbon species (rich in C_n and CO), which serve as reagents for graphene or CNT growth, are generated in much greater quantities than that achievable in stable, self-sustained premixed flames. By using diffusion flames (burning stoichiometrically in the reaction zone), flame speed, flashback, and cellular instabilities related to premixed flames are avoided.

Operation of a multiple inverse-diffusion burner has no scaling problems by allowing for stability at all burner diameters, where the issuing flow velocity can be independent of the burner diameter. Moreover, since many small diffusion flames are utilized, overall radially-flat profiles of temperature and chemical species are established downstream of the burner, ensuring uniform growth. Advantages of this method are

scalability for large-area surface coverage, increased growth rates, high purity and yield, continuous processing, and reduced costs due to efficient use of fuel as both heat source and reagent.

The research is primarily focused on growing carbon nanomaterials using transitional metals and alloys, such as copper (Cu), nickel (Ni), cobalt (Co), iron (Fe), Inconel, Ni-Cu alloy, and stainless steel. The key factors for carbon nanomaterial growth on metals involve carbon solubility, melting point, and chemical stability. Given the different properties of each transitional metal, we seek to identify the conditions suitable for the growth of graphene and CNTs. Our system requires no prior substrate preparation and permits open-environment processing. Also, using the multiple inverse-diffusion flame setup, we examine the effects of flame structure, flame temperature, fuel to oxidizer ratio, inert addition, hydrogen addition, residence time, and other parameters that impact the formation of graphene and CNTs.

1.3 Research Objective

While a number of different flame configurations are used for the production of CNTs, the number of reports on the flame synthesis of graphene is limited. A key reason for this discrepancy is that graphene was only recently “discovered” as compared to CNTs. Another reason is that the flame synthesis of graphene may be more challenging when compared to that for CNTs. Graphene being a two-dimensional material requires large-scale production across a substrate. Due to the temperature and species gradients that occur in most flames, it is difficult to scale the growth of graphene across an entire substrate. Moreover, a reduced environment with carbon rich species, which is necessary

for graphene growth, is difficult to achieve in most flames. The method of interest of this thesis is based on operating multiple diffusion flames in an inverse mode. This multiple inverse-diffusion flame burner can establish a reduced environment with carbon rich species suitable for the growth of graphene. At the same time, this burner can be used for the growth of CNTs.

Therefore, the objective of this thesis is to investigate the growth of graphene using flame synthesis. The use of flames for graphene synthesis is still in its early stage, hence this work will aim to increase the fundamental understanding of the mechanisms involved for graphene growth. Additionally, this thesis seeks to establish the parameters suitable for the growth of graphene and CNTs using the multiple inverse-diffusion burner.

The research components of this thesis involve:

- 1 Novel Multiple Inverse-diffusion Flame Burner. A new setup, based on multiple inverse diffusion flames, is designed and built for carbon nanomaterial synthesis.
- 2 Graphene Film Synthesis. In order to use graphene or few-layer graphene (FLG) in many applications, large-scale synthesis methods are required. This thesis investigates the direct flame-synthesis of FLG on transitional metals. FLG can be transferred to SiO₂/Si and quartz by spin-coating a thin layer of polymethylmethacrylate (PMMA) and etching away the transitional metal. Once transferred, the optoelectronic properties of the FLG are examined. Raman spectroscopy, analytical electron microscopy techniques, and X-ray photoelectron spectroscopy are used to verify the quality and uniformity of the FLG across the substrate.

Substrate material (i.e. copper, nickel, cobalt, iron, and copper-nickel alloy), along with its temperature and hydrogen pretreatment, strongly impacts the quality and uniformity of the graphene films. Thus these parameters are examined in the growth of FLG.

- 3 CNT Synthesis. In previous studies [3,4], well-aligned multi-walled CNTs with uniform diameters (<15 nm) were grown in 1 and 2-D diffusion flame configurations, which are excellent for fundamental investigation, but are limited in their potential for scale up. Hence, the scalable growth of CNTs on large substrates is explored using the novel burner.
- 4 Transitioning Growth from CNTs to Graphene. This thesis investigates the conditions that enable the transitional growth between CNTs and graphene using the multiple inverse-diffusion burner.
- 5 Graphene and CNT Synthesis using Spinel. Solid oxide solutions containing transition metal ions (spinel) have been used to produce CNTs. Spinel can be readily reduced at high temperatures and provide metal particles, which can enable the scalable growth of CNTs and graphene on composites or arbitrary substrates. CNT and graphene growth occurs through decomposition of flame-generated carbon precursors (e.g. CH₄, CO and C₂H₂) over nanoparticles (i.e. Cu, Ni, Co, and Fe) reduced from the solid oxide. The growth of CNTs is explored on NiAl₂O₄, CoAl₂O₄ and ZnFe₂O₄, using both counterflow diffusion flame and multiple inverse-diffusion flames, while the growth of graphene is investigated on CuFe₂O₄ using only multiple inverse-diffusion flames.

- 6 CNT and Iron-oxide Synthesis on Stainless Steel. This thesis explores the growth of CNTs and iron-oxide on a stainless steel substrate using multiple inverse-diffusion flames.

1.4 Approach

Figure 1.1 depicts the general approach undertaken to understand the growth mechanisms involved in flame synthesis of CNT and graphene films. A number of different parameters are investigated, and the results from the ex-situ characterization help to guide the experiment. Overall a set of optimal parameters are determined for graphene and CNT growth.

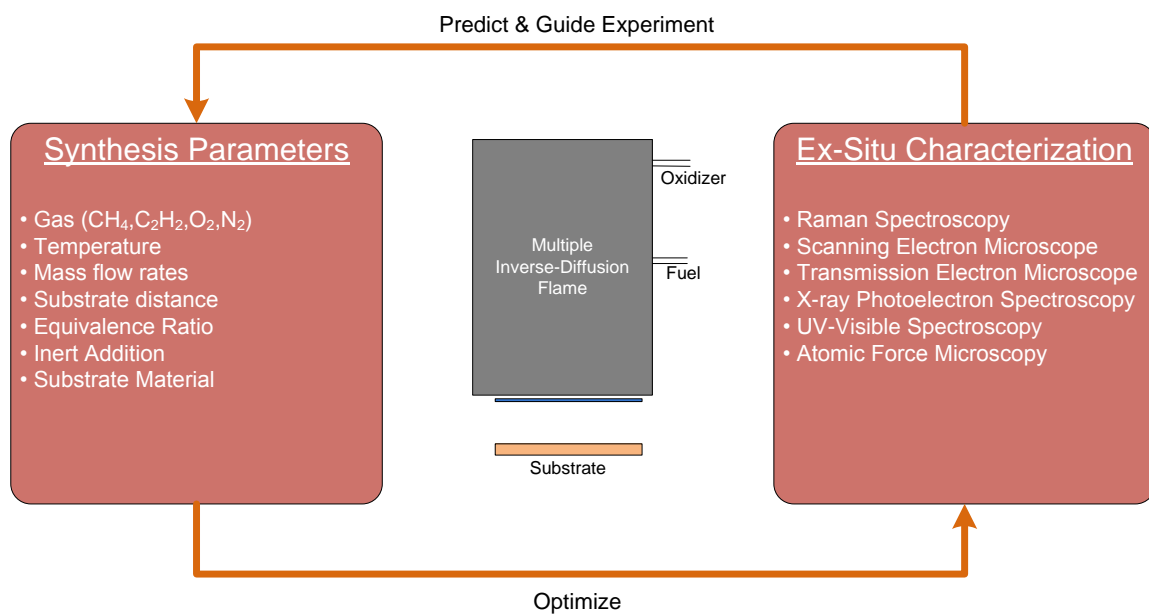


Figure 1.1. General approach used for nanomaterial synthesis.

1.5 Outline of this dissertation

Chapter 2 provides a background review on graphene and CNTs along with different synthesis methods. Chapter 3 describes the experimental setup and the characterization techniques employed. Chapter 4 discusses the structure, property, and thickness of the graphene films prepared on copper and nickel. Chapter 5 further discusses the role of the substrate material, such as copper, nickel, cobalt, copper-nickel, and iron, on the growth of graphene. Additionally the impact of hydrogen and substrate temperature is discussed. Chapter 6 presents the growth of CNTs on various transitional metal alloys. Chapter 7 discusses the transition between CNTs and graphene on nickel alloys as a function of temperature. Chapter 8 investigates the use of metal-oxide spinels for the growth of graphene and CNTs. Chapter 9 examines the growth of iron oxide and CNTs on stainless steel as a function of temperature. Lastly, Chapter 10 highlights some concluding remarks and suggestions for future work.

1.6 References

- [1] Kammler HK, Mädler L, Pratsinis SE. Flame Synthesis of Nanoparticles. *Chem Eng Technol* 2001;24:583-96.
- [2] Teoh WY, Amal R, Madler L. Flame spray pyrolysis: An enabling technology for nanoparticles design and fabrication. *Nanoscale* 2010;2:1324-47.
- [3] Xu F, Liu X, Tse SD. Synthesis of carbon nanotubes on metal alloy substrates with voltage bias in methane inverse diffusion flames. *Carbon* 2006;44:570-7.
- [4] Xu F, Zhao H, Tse SD. Carbon nanotube synthesis on catalytic metal alloys in methane/air counterflow diffusion flames. *Proceedings of the Combustion Institute* 2007;31:1839-47.

Chapter 2

2. Literature Review

2.1 Introduction

Carbon atoms can be arranged in a number of different structural forms (Fig. 2.1), which greatly impacts the properties of the material. The oldest forms of carbon that were discovered include diamond and graphite. Diamond is the strongest and hardest known material, while graphite is one of the best lubricants. Other forms of carbon include fibers and tubes, which can have an extremely high strength, and fullerene molecules that are comprised of 60 carbon atoms in a soccer ball shape [1]. These different structures, with varying properties all have the same building block that is carbon. Hence the fascination and amazement around carbon has been recorded for centuries and new forms are still being discovered (Table 2.1).

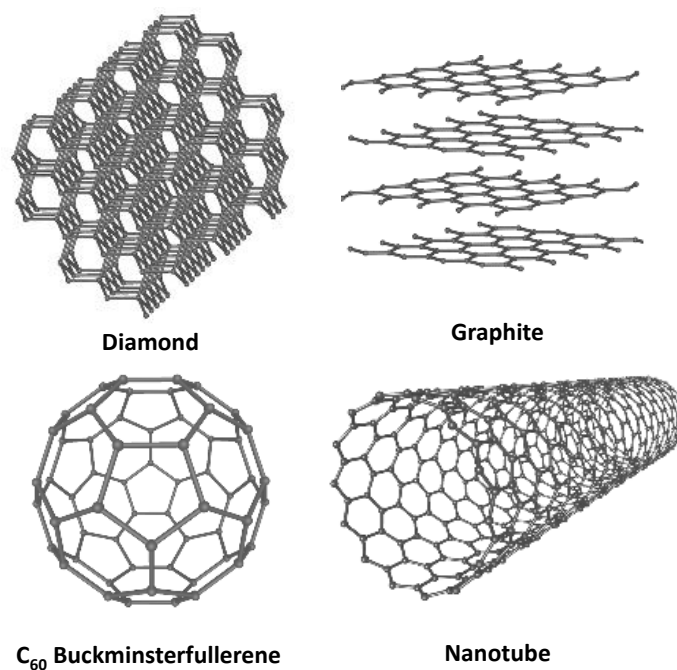


Figure 2.1 Various forms of pure carbon (reproduced from [2]).

First "lead" pencils	1600's
Discovery of the carbon composition of diamond	1797
First carbon electrode for electric arc	1800
Graphite recognized as a carbon polymorph	1855
First carbon filament	1879
Chemical vapor deposition (CVD) of carbon patented	1880
Production of first molded graphite (Acheson process)	1896
Industrial production of pyrolytic graphite	1950s
Industrial production of carbon fibers from rayon	1950s
Discovery of low-pressure diamond synthesis	1970s
Development of diamond-like carbon (DLC)	1980s
Discovery of the fullerene molecules	Late 1980s
Discovery and development of carbon nanotubes (CNTs)	1991
Industrial production of CVD diamond	1992
4 cm long single-wall nanotube (SWNT)	2004
Discovery of Graphene	2004
Sorting of CNTs by size and properties	2006
CVD production of large graphene films	2010

Table 2.1 Chronology and Development of Carbon (reproduced from [3]).

The allotropes of carbon play an important role in the progress of nanoscience. New properties of carbon nanostructures are constantly being realized, resulting in the discovery of numerous applications. A key component for such applications requires an understanding of the synthesis of carbon nanostructures. Hence this chapter will discuss the properties, applications, and synthesis of carbon nanostructures. Specifically the focus will be on sp^2 hybridized carbon, graphene and nanotubes, which has intrigued scientist the most over the past decade.

2.2 Graphene Background

2.2.1 Graphene structure and properties

Graphene comprises of a monoatomic layer of carbon atoms arranged hexagonally. The hexagonal graphene lattice belongs to the plane group $p6m$ with a basis of two carbon atoms. Intrinsic ripples within graphene are confirmed using Monte Carlo simulation [4] and transmission electron studies (TEM) [5]. These ripples tend to have a horizontal dimension of 8 to 10 nm with a vertical displacement of 0.7 to 1 nm (see Fig. 2.2). The stacking of graphene layers along the vertical axis is known as graphite. When the stacking is under 10 layers the material is referred to as few-layer graphene (FLG).

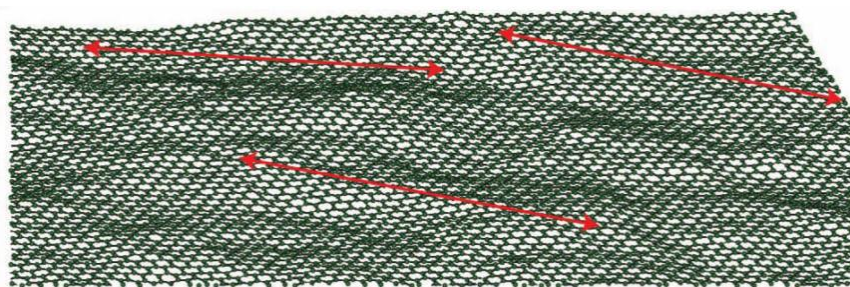


Figure 2.2 Monte Carlo simulation of rippled graphene. The arrows are ~8 nm long (reproduced with caption from [4]).

The bond between carbon atoms within graphene occurs due to sp^2 orbital hybridization, which is comprised of a single 2s carbon orbital along with two 2p carbon orbitals. This results in the carbon atom forming three sigma (σ) bonds with its nearest neighbors. The bond direction is along the hexagonal graphene plane. Additionally, there is a half-filled 2p orbital which results in the formation of pi (π) bonds that is perpendicular to the graphene plane. The σ bonds give rise to the mechanical properties of graphene, while the π bonds enable electrical conduction in graphene or graphite.

2.2.1.1 Electrical properties

Graphene has a unique structure for its charge carriers that resemble massless relativistic particles (Dirac fermions) [7-9]. Also, the primary Brillouin zone contains two different points K and K' (Dirac points), where a band crossing takes place, this results in graphene being a zero band gap semiconductor (see [Fig. 2.3](#)). Graphene exhibits high electronic conductivity due to its well-defined crystal structure. For mechanically exfoliated graphene on Si/SiO₂, the mobility is measured at $\sim 200,000 \text{ cm}^2$ at a carrier density of $2 \times 10^{11} \text{ cm}^{-2}$ [10,11] (see [Fig. 2.4](#)).

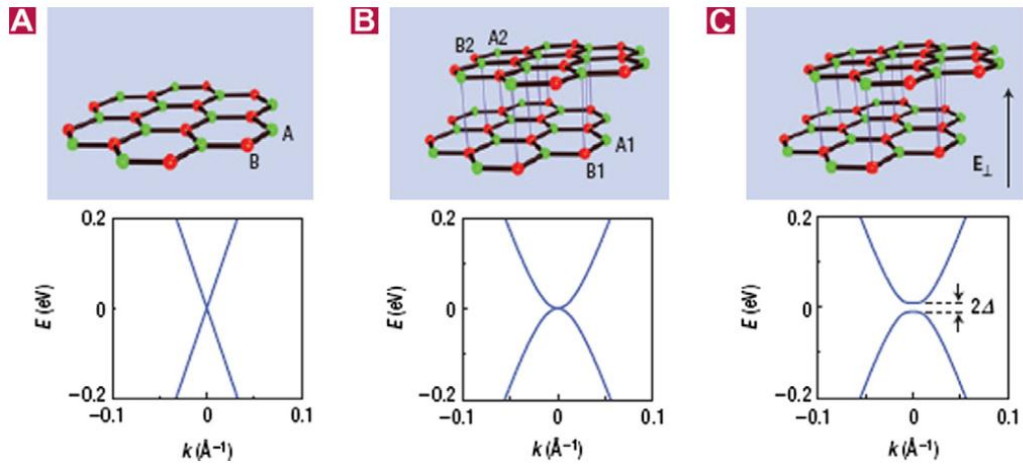


Figure 2.3 Bandgap in graphene devices. Schematic diagrams of the lattice structure of monolayer (a) and bilayer (b) graphene. The green and red colored lattice sites indicate the A (A1/A2) and B (B1/B2) atoms of monolayer (bilayer) graphene, respectively. The diagrams represent the calculated energy dispersion relations in the low-energy regime, and show that monolayer and bilayer graphene are zero-gap semiconductors (for bilayer graphene, a pair of higher-energy bands is also present, not shown in the diagram). (c) When an electric field (E_{\perp}) is applied perpendicular to the bilayer, a bandgap is opened in bilayer graphene, whose size (2Δ) is tunable by the electric field (reproduced with caption from [6]).

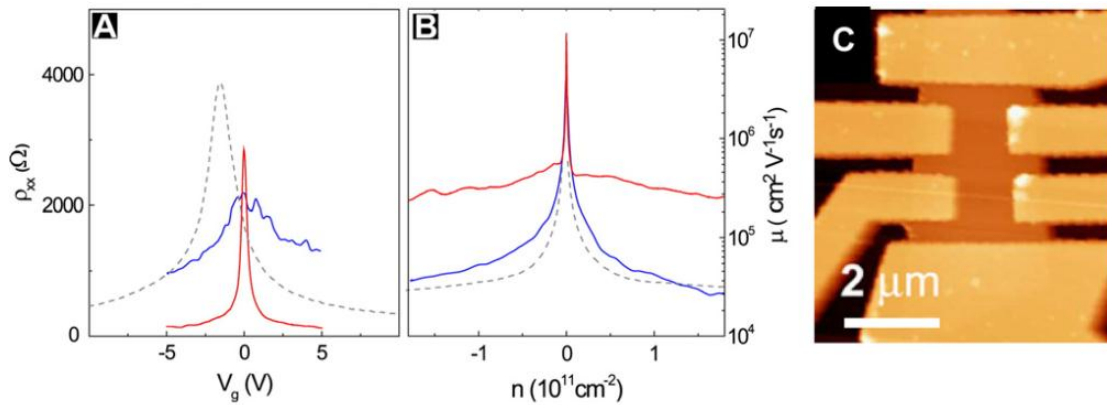


Figure 2.4 (A) Measured four-probe resistivity as a function of gate voltage before (blue) and after (red) current annealing; data from traditional high-mobility device on the substrate (gray dotted line) shown for comparison. The gate voltage is limited to ± 5 V range to avoid mechanical collapse. (B) Mobility as a function of carrier density n for the same devices. (C) AFM image of the setup before the measurements (reproduced with caption from [10,11]).

2.2.1.2 Mechanical properties

The mechanical properties of graphene are measured using numerical simulation, AFM, and Raman. It is reported that the Young's modulus of graphene is 1 TPa and the fracture strength is 130 GPa [12]. Similar results are observed for FLG [13]. Compressive and tensile strain can be measured by monitoring the change in the G and 2D peak of the Raman spectrum, when a stress is applied [14]. Mechanical properties of graphene are summarized in [Table 2.2](#).

Method	Material	Mechanical properties
AFM	Mono layer graphene	$E = 1 \pm 0.1$ TPa $\sigma_{\text{int}} = 130 \pm 10$ GPa at $\varepsilon_{\text{int}} = 0.25$
Raman	Graphene	Strain $\sim 1.3\%$ in tension Strain $\sim 0.7\%$ in compression
AFM	Mono layer Bilayer Tri-layer Graphene	$E = 1.02$ TPa; $\sigma = 130$ GPa $E = 1.04$ TPa; $\sigma = 126$ GPa $E = 0.98$ TPa; $\sigma = 101$ GPa

Table 2.2 Mechanical properties of graphene (reproduced with caption from [11]).

2.2.1.3 Optical properties

Graphene absorbs only 2.3% of incident light over a broad wavelength from 300 to 2,500nm. A peak in the ultraviolet region ($\sim 270\text{nm}$) occurs due to an exciton-shifted singularity in the graphene density of states [15]. In FLG, each layer is perceived as a 2D electron gas, hence little perturbation happens from adjacent layers [15]. Thus, the absorption of light follows a linear relation with the increase of each layer of graphene [16]. Optical image contrast enables the identification of graphene on Si/SiO₂. This technique can also be used to approximate the number of graphene layers (see [Fig. 2.5](#)).

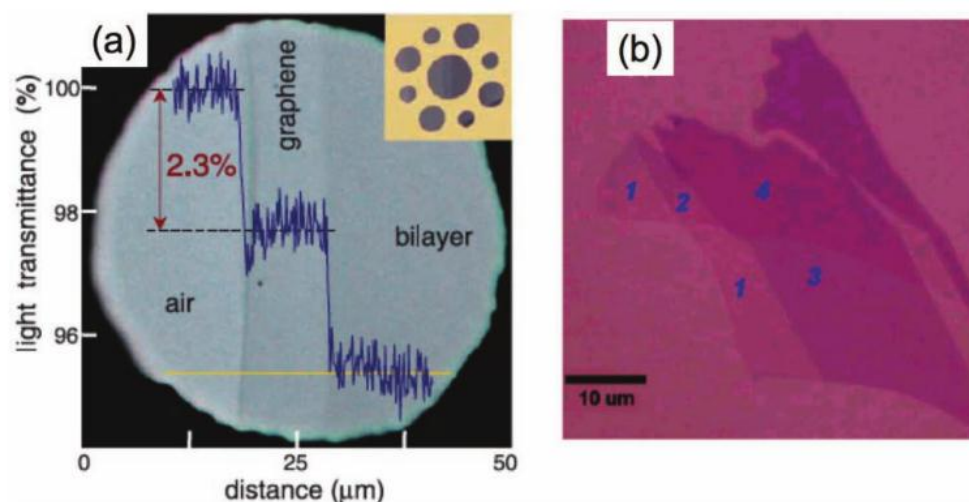


Figure 2.5 (a) Photograph of a 50-μm aperture partially covered by graphene and its bilayer. The line scan profile shows the intensity of transmitted white light along the yellow line. Inset shows the sample design: a 20-μm thick metal support structure has apertures 20, 30, and 50 μm in diameter with graphene flakes deposited over them; (b) Optical image of graphene flakes with one, two, three, and four layers on a 285-nm thick SiO₂-on-Si substrate (reproduced with caption from [17-19]).

2.2.1.4 Thermal properties

Thermal management is a key factor that determines the performance of a material for electronic devices. Large amounts of heat need to effectively be dissipated for higher performance electronic devices. Recently, extremely high thermal conductivity ~5000 W/mK was reported for suspended graphene [20], whereas for supported graphene this value is around 600 W/mK [21]. An effective method to measure the thermal conductivity is using confocal micro-Raman spectroscopy (see Fig. 2.6). The temperature change is determined by measuring the shift in the graphene G peak. For FLG the thermal conductivity is typically lower and in the range between 1000 to 3000 W/mK [22]. A number of factors such as defects, edge scattering, and doping can strongly impact the thermal conductivity of graphene [23,24]. Typically much lower

values are observed for non-pristine graphene such as graphene oxide [25] (see Table 2.3).

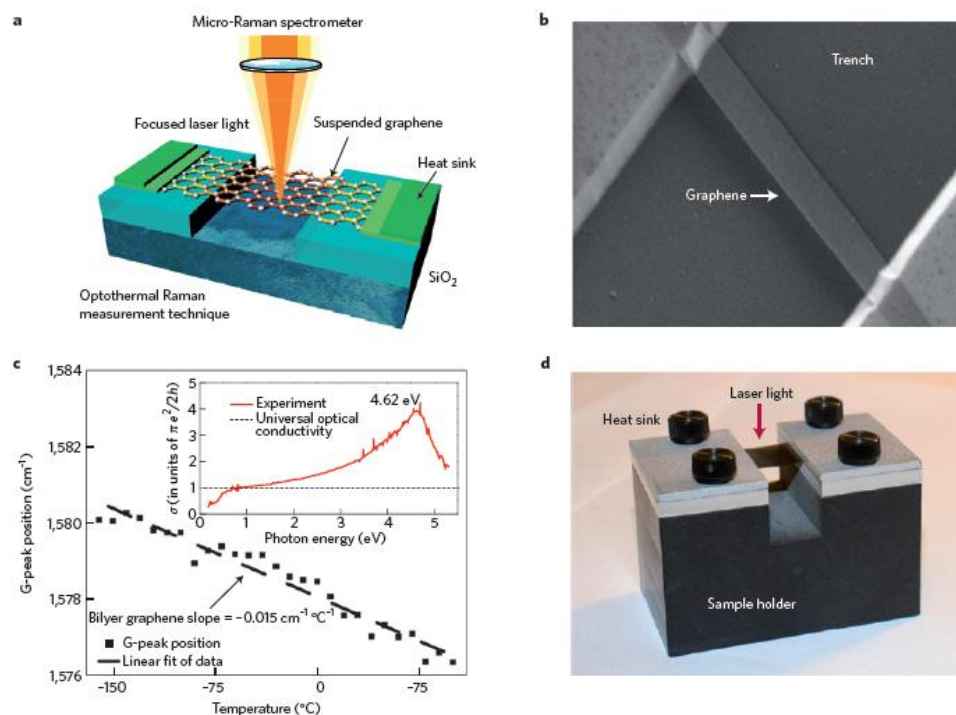


Figure 2.6 Thermal conductivity measurement of graphene using Raman spectroscopy (reproduced with caption from [22]).

Method	Material	Thermal conductivity
Confocal micro-Raman spectroscopy	Single layer graphene	4840–5300 W/mK at RT
Confocal micro-Raman spectroscopy	Suspended graphene flake	4100–4800 W/mK at RT
Thermal measurement method	Single layer (suspended)	3000–5000 W/mK at RT (suspended)
Thermal measurement method	Single layer (on SiO ₂ support)	600 W/mK at RT (on a silicon dioxide support)
Electrical four-point measurement	Reduced graphene oxide flake	0.14–0.87 W/mK

Table 2.3 Thermal conductivity of graphene and graphene oxide based materials (reproduced with caption from [11]).

2.2.2 Graphene synthesis

Initially discovered by micromechanical exfoliation of graphite [26], graphene has generated intense experimental research on its fabrication. Widespread use of graphene will require large-scale synthesis methods. Production methods for graphene that currently exist include mechanical or liquid exfoliation, ultrahigh vacuum (UHV) annealing of SiC, and chemical vapor deposition (CVD). Additionally, the chemical conversion of graphite to graphene oxide can be performed.

2.2.2.1 Micromechanical exfoliation

Micromechanical exfoliation involves peeling highly ordered pyrolytic graphite (HOPG) using adhesive tape [27] (see [Figure 2.7](#)). Since each layer of graphene is connected to the other layer by van der Waals bonding, it is feasible to cleave HOPG. Typically the peeling is performed multiple times. This process can also be used to produce FLG. This is the simplest method for graphene production and is commonly used in laboratory experiments, however it is not scalable for large-scale graphene growth.

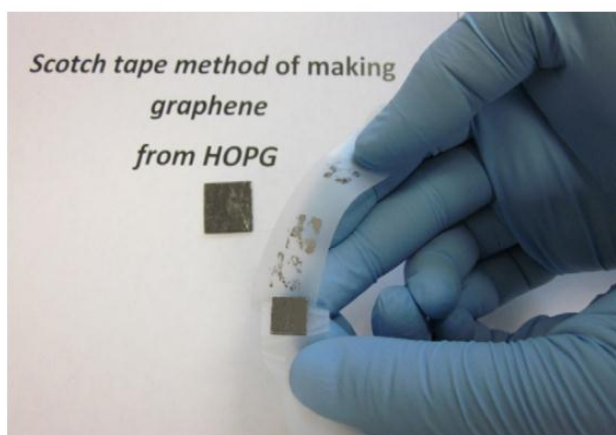


Figure 2.7 Mechanical exfoliation of graphene using scotch tape from HOPG (reproduced with caption from [11]).

2.2.2.2 Liquid-phase exfoliation

Liquid-phase exfoliation (LPE) involves using a solvent to exfoliate graphite by ultrasonication [28,29]. Commonly used solvents include acetic acid, sulfuric acid, and hydrogen peroxide [11]. The ultrasonication time is usually 60 minutes with a power of 250 to 500 W. Green and Hersam reported the use of sodium cholate as a surfactant for the exfoliation of graphene [30] (see Fig. 2.8). Additionally, they were able to separate the sheets by density gradient ultracentrifugation, which enabled the isolation of graphene from FLG. LPE can also be used for the production of graphene nanoribbons [31], where the width of the graphene sheet is less than 10 nm. While LPE represent a scalable method for the production of graphene, large scale film growth remains challenging.

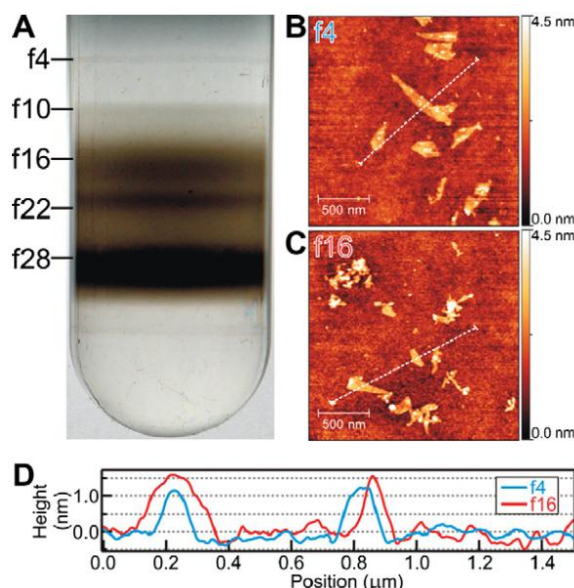


Figure 2.8 (A) Photograph of a centrifuge tube following the first iteration of density gradient ultracentrifugation (DGU). The concentrated graphene was diluted by a factor of 40 to ensure that all graphene bands could be clearly resolved in the photograph. Lines mark the positions of the sorted graphene fractions within the centrifuge tube. (B and C) Representative AFM images of graphene deposited using fractions f4 (B) and f16 (C) onto SiO₂. (D) Height profile of regions marked in panels B (blue curve) and C (red curve) demonstrating the different thicknesses of graphene flakes obtained from different DGU fractions (reproduced with caption from [11,30]).

2.2.2.3 Graphene Oxide

Production of graphite oxide using the Hummers method has been known for over 50 years [32]. Strong acids such as sulfuric acid (H_2SO_4), sodium nitrate (NaNO_3), or potassium permanganate (KMnO_4) are used in the production of graphite oxide. The sonication of graphite oxide results in the synthesis of graphene oxide (GO). Through this process, it is possible to obtain monolayer or few-layer GO. However this method disrupts the sp^2 lattice of graphene, as it can contain epoxide or hydroxyl groups. The reduction of GO (called rGO) [33] can partially remove the hydroxyl or epoxide groups (see Figure 2.9). Despite the reduction, rGO does not exhibit the same properties as graphene. Nevertheless, this method has several advantages such as the ability to produce large sheets at low cost using a facile process [34].

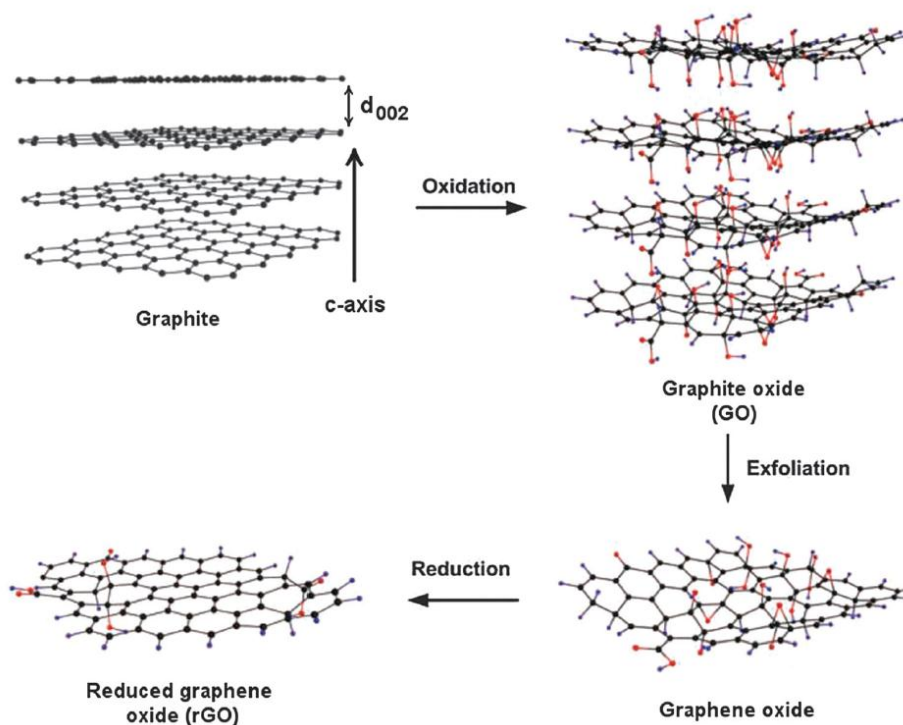


Figure 2.9 Illustration on the preparation of reduced graphene oxide (reproduced with caption from [35]).

2.2.2.4 Annealing of Silicon Carbide (SiC)

When a SiC substrate is heated to a high temperature (around 1200°C), under ultrahigh vacuum (UHV), the silicon atoms sublime from the surface [11]. Subsequently the carbon atoms rearrange to form graphene or FLG. A number of parameters such as time and temperature strongly impact the film thickness and growth quality [36,37]. A key advantage of this process for the semiconductor industry is the direct growth of graphene on an insulating surface. However, the price of a SiC wafer is expensive and the transfer of graphene to other substrates from SiC is challenging. While the growth of graphene on SiC is suitable for certain high performance applications, such as THz frequency electronics [38], it is not viable for a wider range of graphene driven applications.

2.2.2.5 CVD Synthesis

Chemical vapor deposition (CVD) of graphene on transition metals such as nickel (Ni) [39,40] and copper (Cu) [41,42] shows the most potential for large-volume production of graphene. While still in its early stages, CVD-grown graphene has already demonstrated excellent device characteristics [43], including an electron mobility of $7,350 \text{ cm}^2\text{V}^{-1}\text{s}^{-1}$ [38]. In addition, large scale roll-to-roll production of 30-inch graphene films was demonstrated using CVD [43] (Fig. 2.10). The graphene obtained from this process is of high quality, with a sheet resistance of $\sim 125 \text{ }\Omega/\text{square}$ and 97.4% optical transmittance.

Graphene growth using CVD is fairly straightforward (Fig. 2.11), where a copper or nickel substrate is placed in an isothermal reactor at a temperature of around 1000°C. After the substrate is placed in the CVD reactor, hydrogen is added to the reactor. This step is critical to eliminate any oxide layer present on the metal, for the case of Cu this

will reduce any native layers of CuO and Cu_2O . The hydrogen atmosphere also facilitates the growth of grain boundaries [38], which is necessary for the growth of high quality graphene. Afterwards, a hydrocarbon gas (usually methane) is added to the reactor. The hydrocarbon gas provides the necessary carbon species used in the growth of graphene. The hydrocarbon to hydrogen ratio plays an important role in the growth of graphene. If insufficient hydrogen is present, this could result in oxidized metal layers being present, which will lead to a disordered graphene structure. In contrast, excess hydrogen can etch away graphene. On polycrystalline substrates, the graphene flakes tend to have different lattice orientations.

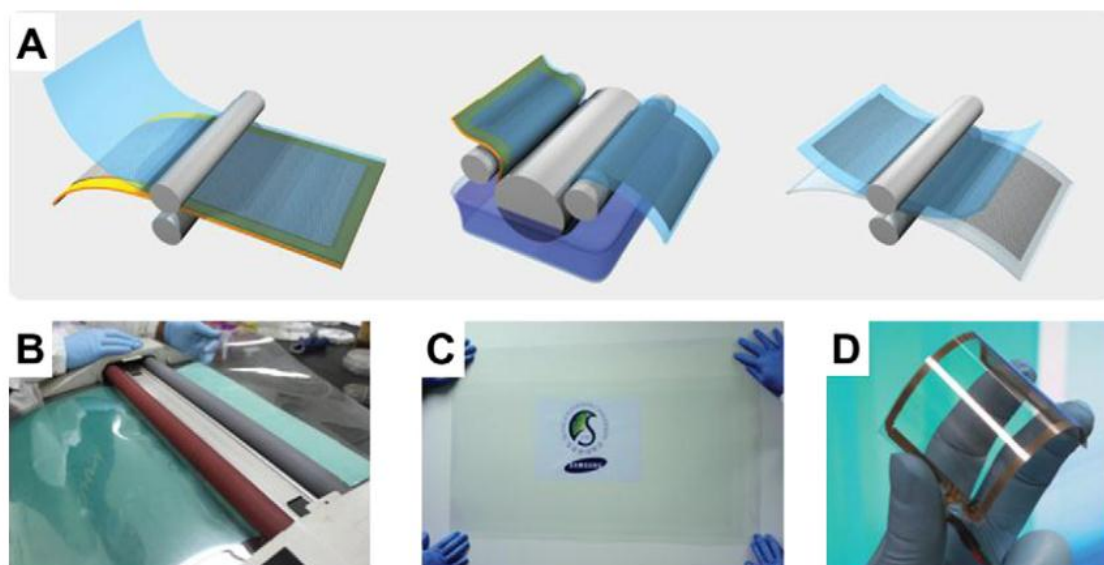


Figure 2.10 a) Schematic of the roll-based production of graphene films grown on a copper foil. The process includes adhesion of polymer supports, copper etching (rinsing) and dry transfer-printing on a target substrate. A wet-chemical doping can be carried out using a setup similar to that used for etching. (a) Roll-to-roll transfer of graphene films from a thermal release tape to a PET film at 120°C . (c) A transparent ultralarge-area graphene film transferred on a 35-in. PET sheet. (d) An assembled graphene/PET touch panel showing outstanding flexibility (reproduced with caption from [11,43]).

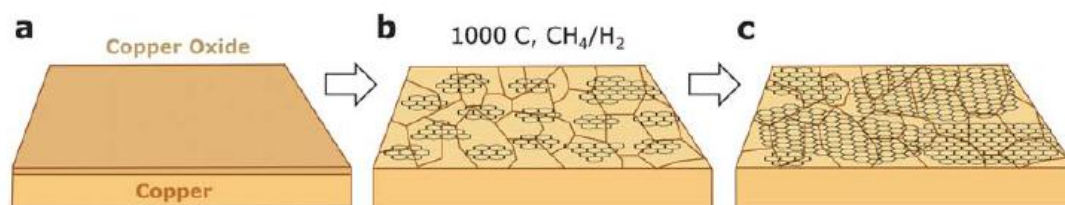


Figure 2.11 Schematic illustrating the three main stages of graphene growth on copper by CVD: (a) copper foil with native oxide; (b) the exposure of the copper foil to CH_4/H_2 atmosphere at $1000\text{ }^{\circ}\text{C}$ leading to the nucleation of graphene islands; (c) enlargement of the graphene flakes with different lattice orientations (reproduced with caption from [38]).

Using CVD, graphene is grown onto transition metals, which provide a low energy pathway by forming intermediate compounds for the growth of graphene. The first row of transition metals (Fe, Co, Ni, and Cu) is of great interest due to their low cost and high availability. The difference in the carbon solubility between these metals (Fig. 2.12) impacts the growth quality. Fe has an asymmetrical distribution of electrons in the d-shell, which gives rise to its high carbon solubility and Cu has a filled 3d shell and has the lowest solubility of carbon. Co and Ni have carbon solubility that falls in between Fe and Cu. Due to its low carbon solubility, Cu is an ideal metal for growing single layer graphene. When using Ni and Co it is common to get up to 10 layers of graphene. Similarly on Fe it is common to have FLG. Figure 2.13 illustrates the growth of graphene or FLG on Ni, Fe, Co, and Cu using CVD.

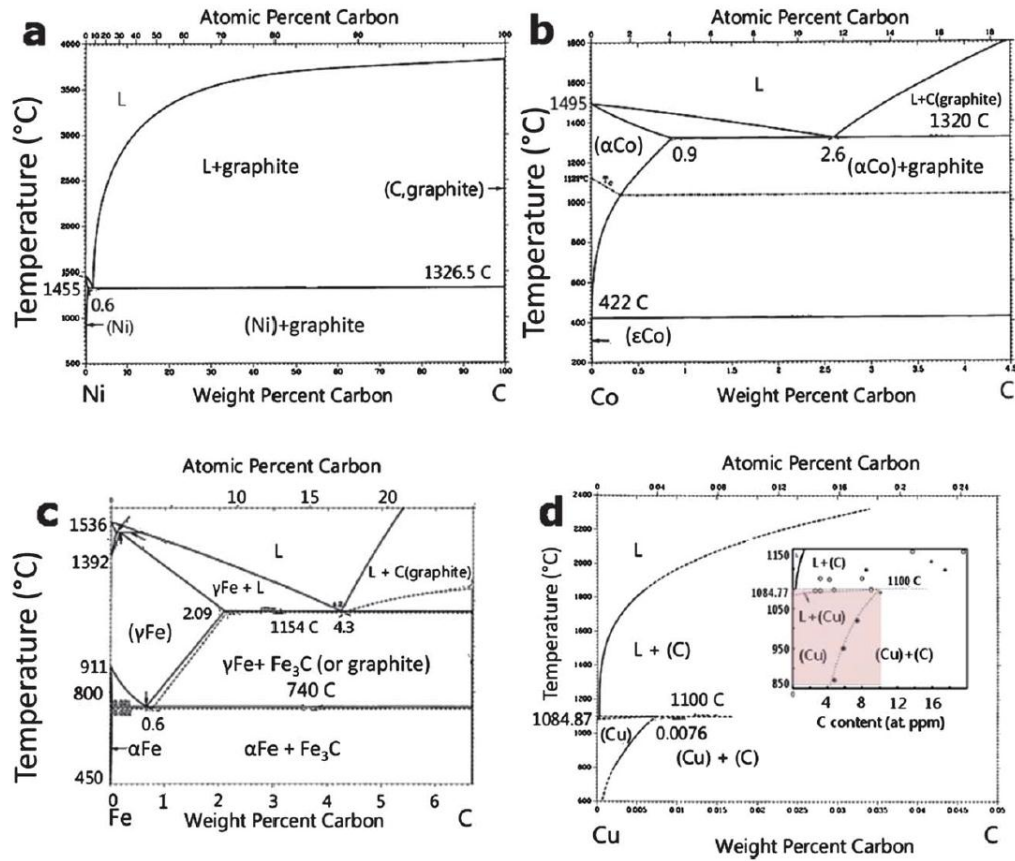


Figure 2.12 Binary phase diagrams of transition metals and carbon. (a) Ni–C; (b) Co–C; (c) Fe–C; (d) Cu–C. The low carbon solubility in Cu, of ~0.008 weight % at ~1084 °C is highlighted in the inset of panel (d) (reproduced with caption from [38]).

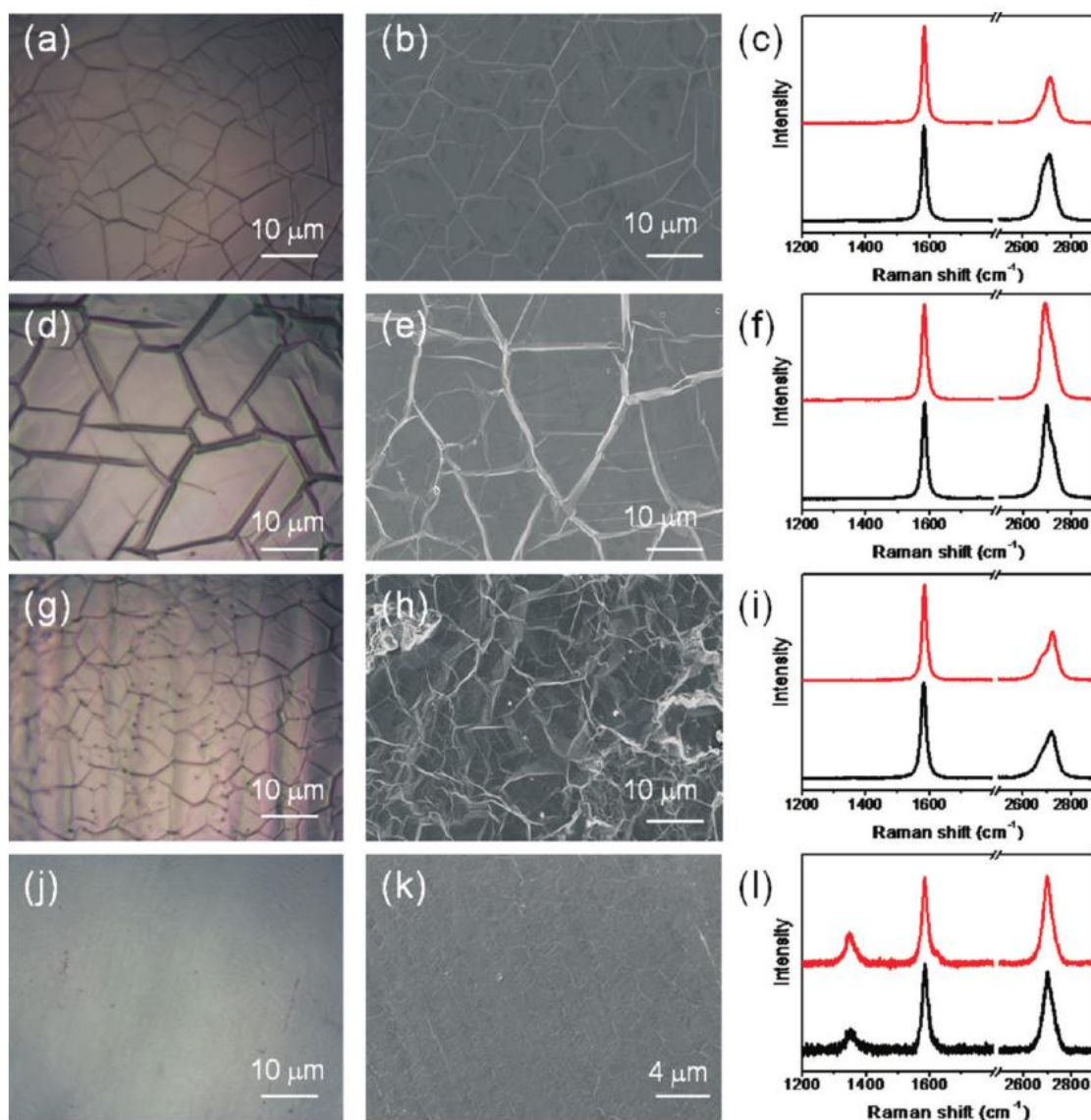


Figure 2.13 Typical optical microscopy images, SEM images, and Raman spectroscopy of MLG and FLG grown on Ni (a-c), Fe (d-f), Co(g-i), and Cu (j-l) foil substrates using ethylene as the carbon source at 975°C. The growth time was 3 min, and the gas mixing ratio of C_2H_4/H_2 was 5/500, and the cooling rate was 60 °C min⁻¹. (a, d, g, and j). Optical microscope images of graphene. (b, e, h, and k) SEM images of graphene. (c, f, i, and l) Raman spectroscopy of graphene. Cu substrate background was subtracted. The spectra were normalized with the G-band (reproduced with caption from [44]).

The growth of graphite on Ni has been known and studied for nearly 50 years. From the phase diagram of nickel and carbon ([Fig. 2.12](#)), we see that at temperatures above 800°C, Ni and C form a metastable solid phase Ni_3C . Upon cooling, the carbon diffuses out of the Ni to form graphene layers. This diffusion occurs at the grain boundaries, where the nucleation of graphene takes place. However, due to the curvature of the grain boundaries, it is common for the nucleation of several layers of graphene to occur. For this reason, it is difficult to grow a single layer of graphene on a large Ni substrate. Additionally the nucleation of graphene results in the formation of graphene flakes, which then join with other flakes and grow in size. When graphene flakes connect, wrinkles tend to form due to stress [40]. With such wrinkles, the subsequent formation of additional graphene layers result in a disordered structure.

Graphene growth on Cu is not caused by the out-diffusion of carbon atoms, as is observed in the case of Ni. Due to the fact that only a trivial amount of carbon is absorbed in copper, the graphene formation occurs due to the breakdown of the hydrocarbon gas on the surface. Once the copper surface is covered by graphene, this deactivates the formation of any additional carbon structure since no metal catalyst is accessible [42]. Hence, Cu has proven to be especially effective in limiting the growth of graphene to a single layer and has been widely studied for the growth of graphene ([Table 2.4](#)) using CVD.

The graphene growth difference on metals was shown in an insightful experiment by the Ruoff group [45]. When using carbon isotope labeling (^{12}C and ^{13}C) the Raman peak of graphene is different. Hence, in their experiment they used a sequence process of $^{12}\text{CH}_4$ followed by $^{13}\text{CH}_4$ to grow graphene. In the case of Ni, the formation of graphene

had a random mix of ^{12}C and ^{13}C . In contrast to Ni, Cu had regions of only ^{12}C graphene and the overall growth pattern followed the precursor time sequence.

Most practical applications of graphene require that the underlying surface be insulating. For this reason, it is important to transfer the graphene sheet from the metal to an insulating surface such as SiO_2 [42]. Additionally, this transfer is required to measure the opto-electronic properties of the synthesized graphene. The commonly used process to transfer graphene is to first deposit and cure poly(methylmethacrylate) (PMMA) on the metal sheet. Afterwards, etch the Cu metal sheet using iron chloride (FeCl_3 in $\text{HCl}/\text{H}_2\text{O}$). This gives a floating sheet of PMMA and graphene, which is rinsed in deionized water. Subsequently, one can transfer this layer to an insulating surface and use acetone to remove the PMMA layer (Fig. 2.14). The transfer of the graphene sheet does result in cracks, particularly when transferring from Ni to an insulating surface. In order to minimize the cracks, it is critical to have good adhesion between the graphene layer and the insulating substrate. For this reason, the use of polyethylene terephthalate (PET) has been researched, which is shown to have good adhesion with graphene [38]. Other methods, such as applying a second coating of PMMA before using acetone have also shown to reduce the number of cracks [46].

Growth Pressure (Torr)	Pre-annealing	H ₂ /CH ₄ flow ratio (scm), growth time and cooling rate	Temperature (°C)	Cu Thickness	#Graphene layers
0.5	1000 °C H ₂ (2 sccm, 0.04 Torr) 30 min (base pressure 0.1 Torr) Acetic acid + heating up to 1000 °C H ₂ (50–200 sccm, 2 Torr 40 °C/min) 900 °C 30 min H ₂ 10 Torr	0.06 (1 min–60 min, cooling rate 40–300 °C/min) 0.23 (10–20 min, cooling rate 20 °C/min + gas flow)	1000 1000	25 µm 500 nm and Cu foil 25 µm	>95% 1 >93% 1
50		10 Torr/40 Torr (10 min, cooling rate 10 °C/s) CH ₄ (99.999%) 15 : 50 : 1000 sccm (H ₂ :CH ₄ :He) (5 min, cooling rate in He 10 °C/s)	850–900 1000	50 µm 700 nm	Few layers 1, 2
0.39	1. Heating up to 1000 °C in ambient pressure. 2. 30 min, 1000 °C He (1000 sccm) + H ₂ (50 sccm) 1. Ar (20 sccm, 0.41 Torr 12 min). 2. H ₂ (20 sccm, 0.3 Torr 1.25 min) up to 766 °C	5 (10 min) cooling in Ar 80 sccm 1 Torr	800	206 nm	1, 2, 3
0.1–0.5	(pre-vacuum) Heating in H ₂ up to 1000 °C (pre-vacuum 0.01) Ar/H ₂ 400 sccm 8–9 Torr up to 950 °C	0.06 (from 15 min up to 420 min) CH ₄ (99.99%) Hexane (4 mL/h) 4 min	1000 950	100–450 nm 25 µm	1 1, 2
0.5	(pre-vacuum) Heating up to 1000 °C H ₂ (13 sccm, 0.1 Torr) 30 min Heating up to 1000 °C H ₂ (8 sccm, 0.18 Torr) 30 min	0.5 (30 s–30 min) cooling rate 9 °C/min 0.33 (30 min) (cooling rate 10 °C/s, H ₂ 0.18 Torr)	1000 1000	25 µm, 125 µm 25 µm	1, 2 1

Table 2.4 Summary of CVD conditions reported in the literature to grow graphene on copper (reproduced with caption from [38]).

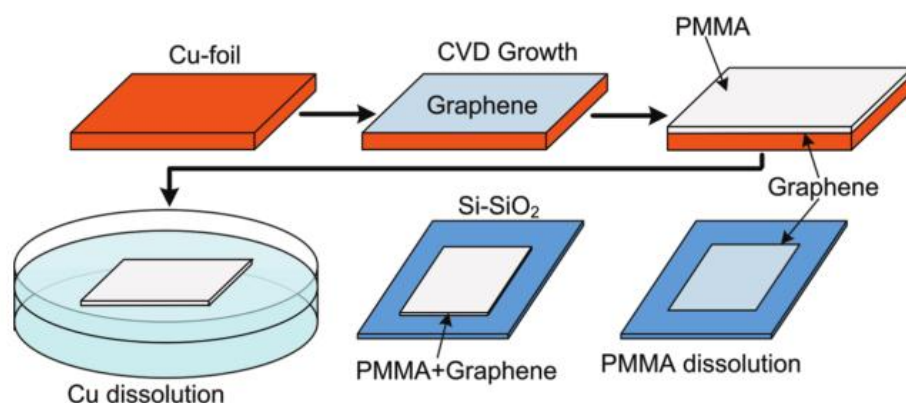


Figure 2.14 Schematic illustration of CVD growth of graphene and its transfer process (reproduced with caption from [47]).

2.2.2.6 Plasma enhanced CVD

Plasma enhanced CVD (PECVD) is another method used for the production of graphene that is comparable to the thermal CVD process [48-50]. Both the growth of graphene and FLG has been reported using PECVD. Typical growth conditions are 5 to 100% CH₄ in H₂ with a substrate temperature of 680°C [11,51]. The power of the plasma is 900W. A key advantage of the process is the ability to grow graphene at lower temperatures and shorter duration (<5min). However, the quality of the graphene film is typically lower when compared to thermal CVD.

Other less common methods used for the production of graphene that are not covered in this chapter are, total organic synthesis, un-zipping CNTs [52], and laser deposition [53].

2.3. Carbon Nanotube Background

2.3.1 Carbon Nanotubes structure and properties

Carbon nanotubes (CNTs) are sheets of graphene that can be rolled to form a tube. A single-wall nanotube (SWNT) comprises of a single graphene sheet, while a multi-wall nanotube (MWNT) is formed from multiple graphene sheets [54]. The diameter of a SWNT is 1.4 nm, while the diameter of a MWNT can range from ten to several hundred of nanometers. For MWNTs, the spacing between the graphene layers is 0.34 nm. The length of a CNT easily extends to the order of a micron, hence the disparity between the length and diameter makes CNTs a very unique structure. CNTs have the highest aspect ratio (length to diameter) among all known materials. Another key category that is used to describe a CNT is chirality [55], which signifies the twist within the graphene wall of the CNT. Depending on the chirality, the CNT can either be semiconductive or metallic. The chirality of a CNT is uniquely identified using two indices (n,m) (Fig. 2.15). Commonly classified CNTs include arm-chair, (m,m) nanotubes, and zig-zag, $(n,0)$ nanotubes (Fig. 2.16).

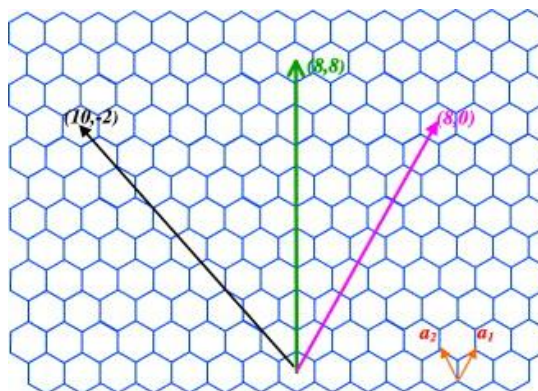


Figure 2.15 Schematic honeycomb structure of a graphene sheet. Carbon atoms are at the vertices. SWNTs can be formed by folding the sheet along lattice vectors. The two basis vectors a_1 and a_2 , and several examples of the lattice vectors are shown (reproduced with caption from [55]).

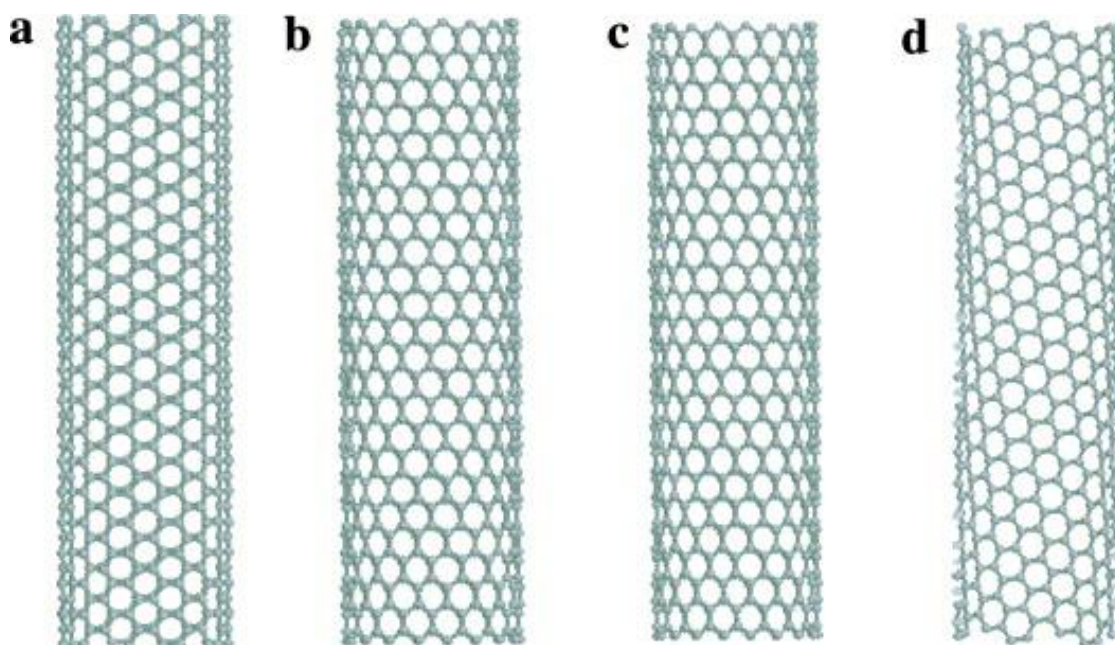


Figure 2.16 Schematic structures of SWNTs (a) A (10,10) arm-chair nanotube (metallic nanotube). (b) A (12, 0) zigzag nanotube. (A small band gap can develop due to the curvature of the nanotube.) (c) The (14, 0) zigzag tube is semiconducting. (d) A (7, 16) tube is semiconducting. This figure illustrates the extreme sensitivity of nanotube electronic structures to the diameter and chirality of nanotube (reproduced with caption from [55]).

The structure of a CNT, such as chirality and diameter, strongly impact its properties. Similar to graphene, CNTs exhibit high strength due to the sp^2 bonded carbon atoms. A Young's modulus of 1 TPa with a tensile strength of 63 GPa has been observed for CNTs [56,57]. Additionally CNTs are extremely flexible [57], however they undergo buckling under compression. Both MWNTs and SWNTs show excellent thermal properties along the tube length. The thermal conductivity for an isolated SWNT is around ~ 6600 W/mK [58], which is similar to the value obtained for graphene.

The electrical properties of a CNT can vary significantly based on the chirality. Depending on the indices (n,m), a SWNT is metallic when $n - m = 3i$, where i is an

integer. All armchair nanotubes are metallic and roughly one-third of zigzag nanotubes are metallic. The current density for a metallic nanotube can be 1000 greater than metals such as copper and silver [59]. Additionally CNTs have unique chemical properties when compared to other graphitic structures. This is due to the curvature induced $\sigma - \pi$ hybridization on the surface and the large number of topological defects [59].

2.3.2 CNT Synthesis

Three basic components are typically required for the synthesis of CNTs: (i) a source of carbon; (ii) a source of heat; and (iii) the presence of certain metals. A number of techniques have been developed for CNT synthesis, which include arc discharge, pulsed laser vaporization, and chemical vapor deposition.

2.3.2.1 Arc discharge

Arc discharge is the first method used for the synthesis of CNTs in 1991 by Iijima [60]. This technique involves the use of two graphite electrodes in a low-pressure chamber filled with argon or helium (Fig. 2.17a) [61]. A direct current is applied that causes the vaporization of the electrode, which results in the production of CNTs, amorphous carbon, fullerenes and other carbonaceous products. SWNTs are formed by inserting a metal catalyst (Ni, Co or Fe) in the graphitic anode, while leaving the cathode as pure graphite [62]. While this process has played a critical role in the discovery of CNTs it is not preferred for scalable industrial production. The overall synthesis process is discontinuous with significant attention needed between batches.

2.3.2.2 Pulsed Laser Deposition

The pulsed laser deposition (PLD) method was initially developed by Smalley's group at Rice University for the synthesis of CNTs (in 1995) and fullerenes [63]. In this technique, a laser is used to vaporize a graphite target or a carbon-containing feedstock (CH_4 or CO) at low pressure (Fig. 2.17b). The target is typically placed in a temperature controlled furnace. SWNTs are observed using a metal catalyst and optimal inert gas and catalyst mixture are similar for arc discharge and PLD [64]. While PLD is more scalable when compared to arc discharge, lasers are a costly energy source and thus not suitable for large scale production.

2.3.2.3 Chemical Vapor Deposition

Chemical vapor deposition (CVD) is a well-established and scalable method for the growth of CNTs (Fig. 2.17c). A number of different CVD configurations have been utilized, including horizontal furnace, fluidized bed reactor, vertical furnace, and plasma enhanced CVD [62]. A key advantage of the horizontal furnace is that it is isothermally heated; hence there is no temperature gradient across the substrate. A wide range of temperatures from 500°C to 1100°C have been reported for CNT growth. A lower temperature growth typically involves using a plasma enhanced (PECVD) [65]. A number of different hydrocarbons in the form of gas, liquid, and solid can be used.

The metal catalyst/substrate strongly impacts the growth of CNTs in a CVD reactor. There are two methods for the introduction of the catalyst, the first being it is placed on the substrate prior to the synthesis, known as surface deposition, or the second being it is introduced as a precursor during the growth process, known as floating

catalyst. The growth of MWNTs is usually observed during the surface deposition method, while the growth of SWNTs is observed using the floating catalyst method. Large quantities of CNTs have been produced using CVD, where Smalley and co-workers reported that a high pressure reactor can yield ~10g/day of SWNTs [62,66]. A drawback of the CVD method is the time required for the synthesis process.

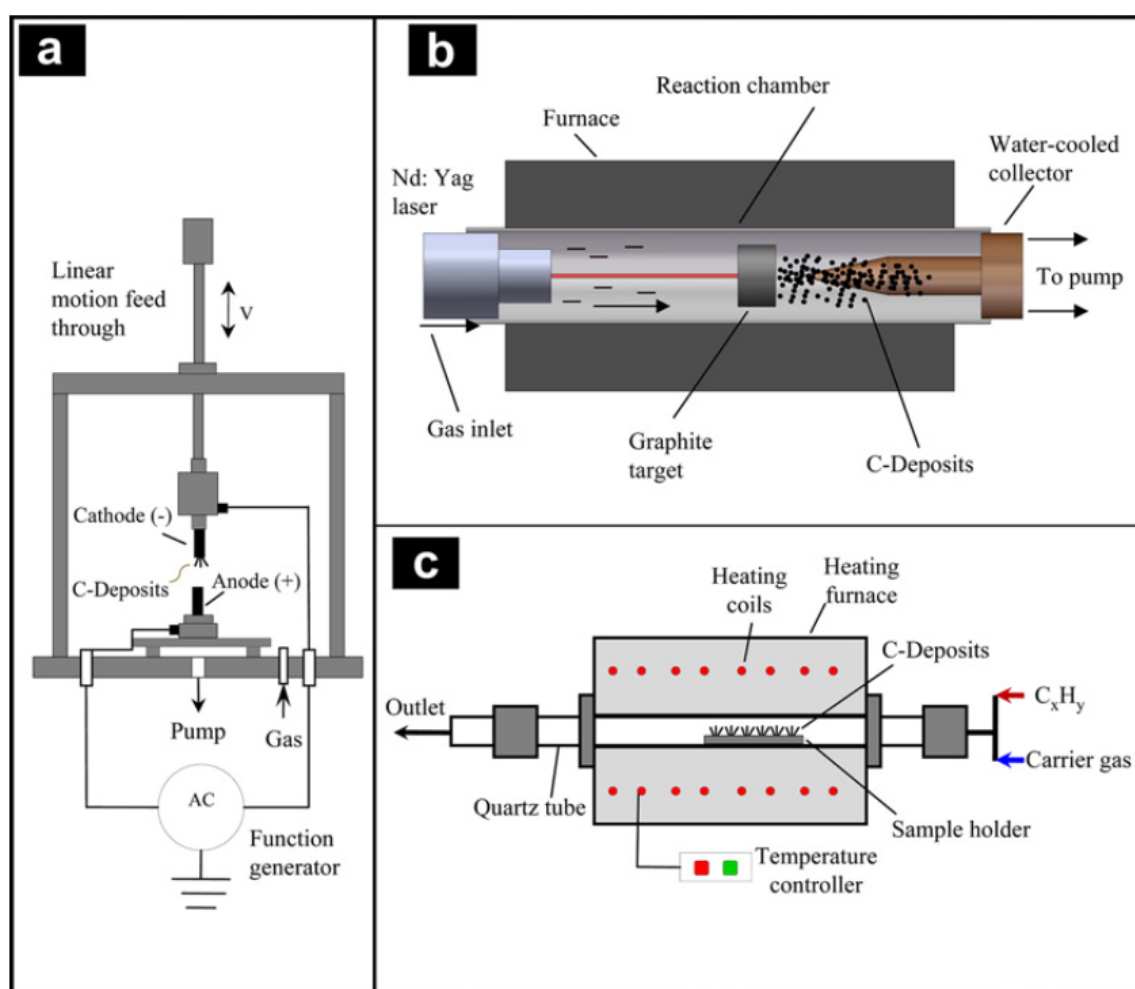


Figure 2.17 Methods currently applied for the growth of CNTs: (a) the arc-discharge method; (b) the pulsed laser vaporization method; (c) the chemical vapor deposition method (reproduced with caption from [62]).

2.4 Applications of Graphene and Carbon Nanotubes

The electrical, mechanical, and chemical properties of graphene and CNTs afford a wide range of applications. Specific applications that are discussed in this section include sensors, transparent conductive films, clean energy devices, field effect transistors, composites, oxidation resistance, and catalysis.

2.4.1 Sensors

Due to the change in conductance as a function of surface adsorption, coupled with large specific surface area, both graphene and CNTs are promising materials for sensors [67,68]. A number of experiments have demonstrated the use of CNTs and graphene for sensors. Adu et al. [69] showed the change in voltage by flowing He, N₂, and H₂ on a tangled mat of SWNTs. Varghese et al. [70] constructed a device based on MWNTs to detect humidity, ammonia, carbon monoxide, and carbon dioxide. There are a few drawbacks of using pristine CNTs as sensors, such as they lack specificity to distinguish between gases and limited sensitivity for certain gases. Recently new sensors are being developed based on the functionalization of CNTs with conducting polymers and metal nanoparticles [71]. These new sensors should help overcome the limitations associated with sensors based on pristine CNTs.

Graphene is also a promising candidate for the detection of gases. [Figure 2.18](#) illustrates a typical setup where graphene is used to detect NH₃. These results illustrate that NH₃ molecules adsorb and dope the graphene surface. Studies suggest that NH₃ and CO molecules are donors, while H₂O and NO₂ are acceptors, on the graphene surface [72]. Graphene oxide is also used for various sensing applications, where it can detect at

the parts-per-billion level [17]. Additionally, hybrid films based on CNTs and graphene exhibit enhanced sensitivity [73].

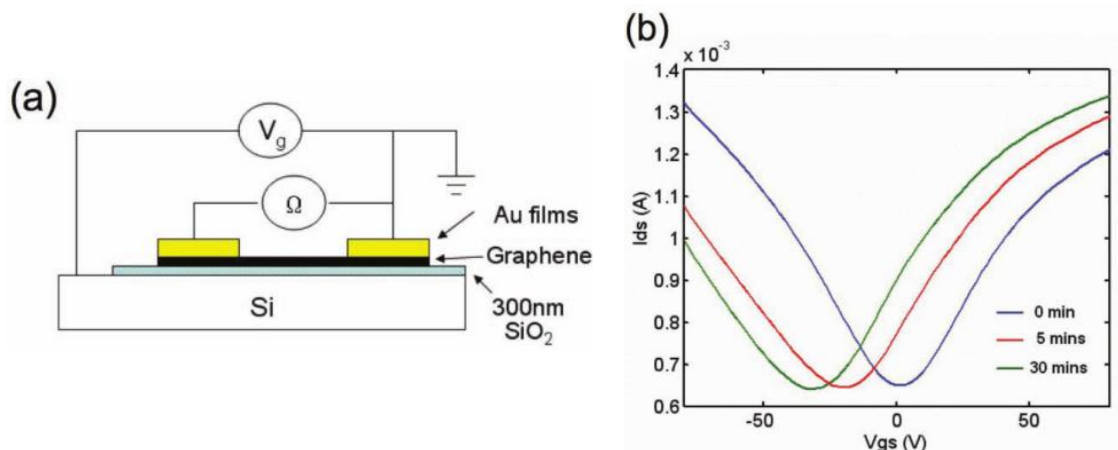


Figure 2.18 (a) Schematic of a graphene gas sensor device. (b) Evolution of I_{ds} - V_{gs} curves with the exposure to NH_3 of the graphene for different durations (reproduced with caption from [17]).

2.4.2 Transparent Conductive Films

Indium tin oxide (ITO) is widely used in the production of transparent electrodes and is often the bench mark when comparing other transparent conductive films. Commercially available ITO has a transmittance of around ~80% and a sheet resistance of 10 Ω/sq [32]. Due to the scarcity and rising cost of ITO, the scientific community is focused on developing alternatives to ITO. Graphene and CNTs have the potential to replace ITO in devices. While most methods that are used for graphene production result in a higher sheet resistance when compared to ITO (Fig. 2.19), the properties of CVD prepared graphene on Cu are similar to that of ITO (Table 2.5). As for CNTs, a major drawback is the resistance from tube to tube, resulting in a higher sheet resistance (Table 2.6). Networks containing CNTs and graphene flakes could possibly lower the sheet resistance

for CNT based transparent electrodes [74]. Nevertheless, graphene and CNTs are of significant importance as a viable alternative to ITO.

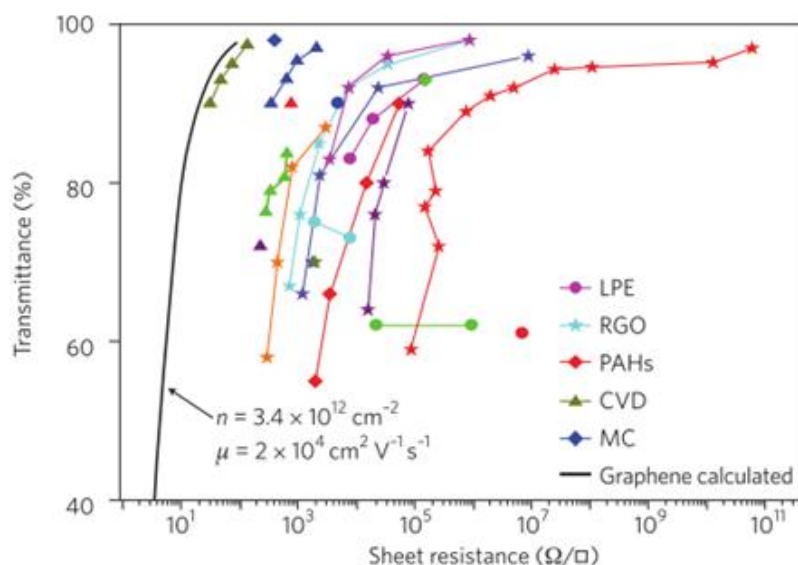


Figure 2.19 Transmittance versus sheet resistance for graphene based on production strategies: triangles, CVD; blue rhombuses, micromechanical cleavage (MC); red rhombuses, organic synthesis from polyaromatic hydrocarbons (PAHs); dots, liquid-phase exfoliation (LPE) of pristine graphene; and stars, reduced graphene oxide (RGO). A theoretical line as for equation is also plotted for comparison (reproduced with caption from [32]).

Year	Author	Preparation of graphene	Method of transparent conductive film	Sheet resistance	Transmittance at 500–550 nm
2007	Wang ²⁹	Graphene oxide/reduction	Dip coating	1.8 kΩ/sq	> 70%
2008	Wu ³⁰	Graphene oxide/reduction	Spin coating	5 kΩ/sq ~ 1 MΩ/sq	> 80%
2008	Li ¹⁹	Exfoliated graphene by molecule/annealing	Langmuir–Blodgett (LB)	8 kΩ/sq	80%
2008	Blake ³¹	Exfoliation in DMF with sonication	Spray deposition	5 kΩ/sq	90%
2008	Blake ³¹	Microcleavage/chemical doping	Transfer	400 Ω/sq	98%
2010	Lee ³²	Exfoliation in liquid/nitric acid treatment	Filtration/transfer	3 kΩ/sq	80%
2010	Yamaguchi ³³	Graphene oxide/reduction	Spin coating/transfer	1 kΩ/sq	70%
2009	Reina ⁵⁴	CVD/Ni	Etching/transfer	770 Ω/sq ~ 1000 Ω/sq	90%
2009	Park ¹⁵	CVD/Ni	Etching/transfer	600 Ω/sq	85%
2009	Kim ³⁵	CVD/Ni	Etching/transfer	280 Ω/sq	90%
2009	Li ²⁸	CVD/Cu	Etching/transfer	350 Ω/sq	90%
2010	Bae ¹⁶	CVD/Cu	Etching/transfer	40 Ω/sq	90%

Table 2.5 Comparison of sheet resistances of graphene based transparent conductive films (reproduced with caption from [74]).

Year	Author	Preparation of SWNT	Method of transparent conductive film	Sheet resistance	Transmittance at 500–550 nm
2004	Wu ⁴⁶	Dual pulsed laser vaporization	Filtration/transfer	30 Ω /sq	> 70%
2006	Zhang ⁴⁷	HiPCO or arc discharge (P3)	Filtration/transfer	HiPCO (7200 Ω /sq)	87%
			SOCl ₂ doping	P3(380 Ω /sq)	
2007	Geng ¹⁸	Arc discharge	Spray coating/HNO ₃ doping	40 Ω /sq	70%
				70 Ω /sq	80%
2007	Andrade ⁴⁸	HiPCO	Dipping coating	186 Ω /sq	86%
2008	Green ⁴⁹	HiPCO	Filtration/transfer	140 Ω /sq	> 70%
		Laser-ablation			
		Arc discharge			
		Sorting metallic SWNTs			
2008	Jackson ⁵⁰	Arc discharge	Filtration/transfer	170 Ω /sq	80%
			Doping (SOCl ₂ or HNO ₃)	140 Ω /sq	
2010	Kim ⁵¹	CVD	Spray coating/densification (D)	259 Ω /sq (before D)	80%
				150 Ω /sq (after D)	

Table 2.6 Comparison of sheet resistances from SWNT based transparent conductive films (reproduced with caption from [74]).

2.4.3 Clean energy devices

Carbon nanomaterials such as CNT, graphene, fullerene and carbon black are widely used in clean energy related devices. Two specific applications that has been the focus of the scientific community, is the use of CNT or graphene based electrodes for electrochemical double layer capacitors (ELDC) and rechargeable lithium ion batteries (RLBs). While the use of CNTs in clean energy applications has been predicted since the 1990s [75], more recently graphene is expected to be a promising electrode material due to its high theoretical surface area of $2630 \text{ m}^2 \text{ g}^{-1}$ [67].

ELDCs are ultracapacitors that store charge at the interface between a high surface area electrode and electrolyte [67]. Activated carbon (supplemented with carbon black), due to its high specific surface area, is often used as an electrode in an EDLC. While the specific surface area (SSA) is the most important parameter that determines the performance of an ELDC, other parameters such as long cycling life and thermal stability are of equal importance. Ni et al [76] used MWNTs as an electrode material for an EDLC with an SSA of $430 \text{ m}^2 \text{ g}^{-1}$ and capacitance of 113 F g^{-1} . While a range of SSA and

capacitance values have been reported for graphene based EDLCs, Vivekchand et al. [77] demonstrated the use of reduced graphene oxide as an electrode with a SSA of $925\text{ m}^2\text{ g}^{-1}$ and capacitance of 117 F g^{-1} . In general graphene has a higher SSA and capacitance when compared with CNTs (Table 2.7).

Carbon based EDLC materials	SSA ($\text{m}^2\text{ g}^{-1}$)	C_m (F g^{-1})
Activated carbon	1000~3500	< 200
Activated carbon fiber	1000~3000	120~370
Templated carbon	500~3000	100~350
Carbon aerogel	400~1000	100~125
Carbon nanotube	120~500	15~135
GBMs	<1500	14~264

Table 2.7 Comparison of the EDLCs based on different carbon materials (reproduced with caption from [78]).

RLB is the most used battery for portable electronics due to its high energy density, high voltage, and long cycling life. The development of future devices, such as electric vehicles, depends on the continued advancement of RLBs. Graphite is the commercialized anode used in LIB due to its good life-cycle performance and high columbic efficiency [78]. A limitation of graphite is that the specific capacitance is restricted to 372 mA h g^{-1} , due to the formation of LiC_6 . Kudo et al. [79] demonstrated that the specific capacitance of graphene oxide is 540 mA h g^{-1} , which can further increase to 730 or 784 mA h g^{-1} , with the addition of CNTs or C_{60} . However a drawback is the rapid decrease in performance with increasing cycle numbers (Fig. 2.20).

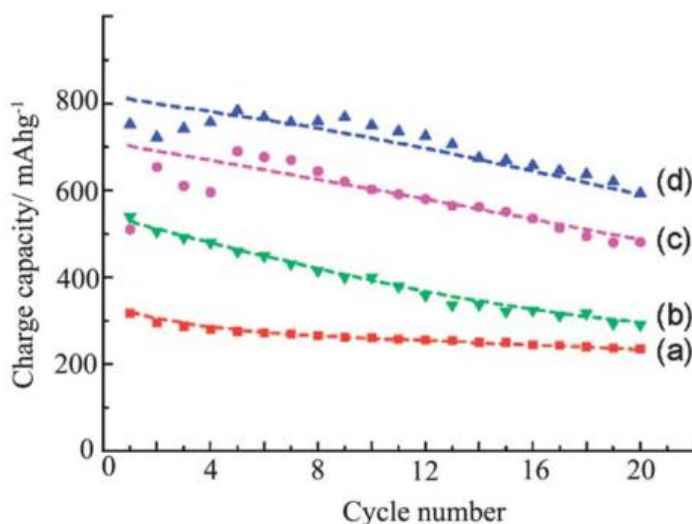


Figure 2.20 Charge/discharge cycle performances of (a) graphite, (b) graphene, (c) graphene + CNT, and (d) graphene + C₆₀ at a current density of 0.05 A g⁻¹ (reproduced with caption from [78,79]).

While significant progress has been made in the use of graphene for clean energy devices, numerous challenges still remain. Specific challenges include: (i) structural defects and restacking of graphene limit the exposed surface area, such that the high theoretical SSA of graphene is unachievable, (ii) chemical and physical instability limits the life-time of graphene based devices, and (iii) a better understanding of the mechanism involved with the use of graphene. Nevertheless, researchers believe graphene can still overcome many of the bottlenecks of current clean energy devices [78].

2.4.4 Field effect transistor

Due to the unique band structure and bipolar carriers of graphene, a gate electrical field can control the electrons and holes for usage in field effect transistors (FET) [67]. Various high frequency FETs have been built using graphene. A cutoff frequency of 100 GHz was reported using graphene synthesis on SiC [80]. Similarly, CVD graphene from

copper was transferred to a wafer of diamond-like carbon and a cutoff frequency of 155 GHz was reported [81]. Such performance can enable the next generation of transistors for radio-frequency applications. Since graphene is a zero bandgap material, such devices cannot be used to replace silicon-based microprocessors. Therefore the introduction of a bandgap within graphene is the subject of scientific research [82].

2.4.4 Composites

Graphene and CNTs based polymer composites have shown enhanced properties related to tensile strength, elastic modulus, electrical conductivity, and thermal conductivity. A challenge associated with CNT based composites is that the CNTs tend to stay in bundles, rather than being distributed evenly throughout the composite [83,84]. Due to the high specific surface area, graphene can further increase the performance of various composites. Graphene based polymer composites that have been studied include polystyrene (PS), PMMA, polyvinyl alcohol (PVA), polypropylene (PP), epoxy, polyester, silicone foam, polyurethane, poly(vinylidene fluoride), and polycarbonate [67]. The addition of graphene-oxide to PVA (at 0.7% loading) resulted in a 76% increase in the tensile strength and 62% increase in the Young's modulus [85].

There is a need for improved thermal interface materials (TIMs), specifically in use in electronics. Current polymer or grease based TIMs use silver particles, which require a high volume fraction (up to 70%) [22]. CNT or graphene based TIMs can significantly enhance the thermal conductivity of a base material at a much lower volume fraction ([Table 2.8](#)).

Filler	Enhancement	Volume fraction	Base material
MWCNT	160%	1.0 vol. %	Oil
SWCNT	125%	1.0 wt %	Epoxy
SWCNT	200%	5.0 wt %	Epoxy
Graphite nanoplatelets	3,000%	25.0 vol. %	Epoxy
Graphene oxide nanoparticles	30–80%	5.0 vol. %	Glycol; paraffin
Graphene oxide	400%	5.0 wt %	Epoxy resin
Graphene	500%	5.0 vol. %	Silver epoxy
Graphene	1,000%	5.0 vol. %	Epoxy

Table 2.8 Thermal conductivity enhancement in nanocarbon composites (reproduced with caption from [22]).

2.4.5 Oxidation Resistance

Many applications of refined metals require a protective coating that prevents against oxidation. The production of such coatings is a major industry [86], which uses many different methods, such as coating with organic layers, paints, polymers, and amorphous carbon. In many cases the physical properties of the reactive metals are modified. Graphene and FLG offer the advantage of providing a coating that is one to a few atoms thick, while preserving the metal properties. Recently CVD grown graphene on Cu and Ni/Cu served as an excellent passivation layer for the metal [86]. While slight oxidation does occur at the graphene grain boundaries, the graphene layer provides perfect protection within the grains. [Figure 2.21](#) illustrates the role of CVD grown graphene as a protective layer on Cu and Cu/Ni.

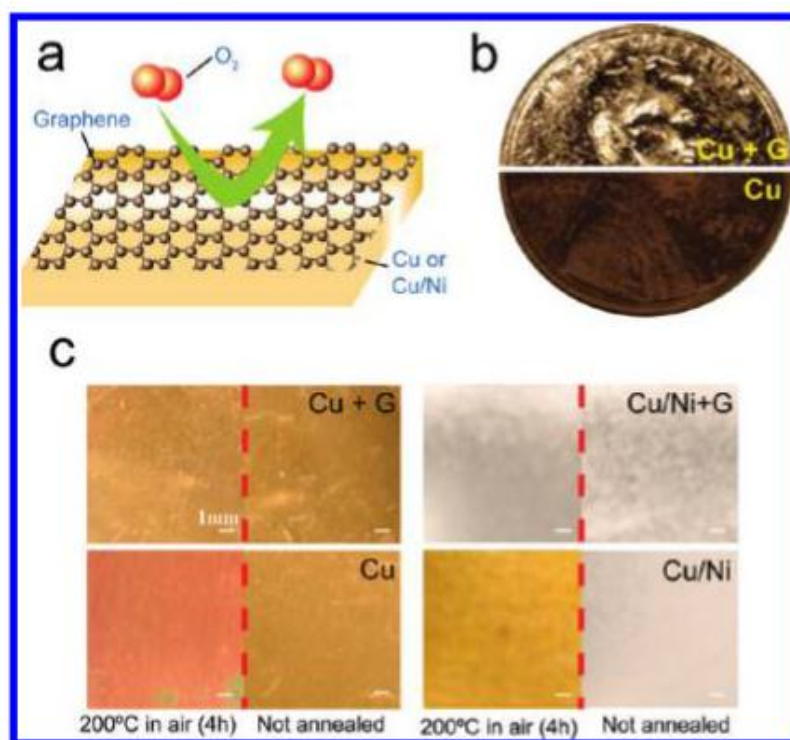


Figure 2.21 (a) Illustration depicting a graphene sheet as a chemically inert diffusion barrier. (b) Photograph showing graphene coated (upper) and uncoated (lower) penny after H_2O_2 treatment (30%, 2 min). (c) Photographs of Cu and Cu/ Ni foil with and without graphene coating taken before and after annealing in air (200 °C, 4 h) (reproduced with caption from [86]).

2.4.6 Catalysis

Another important application of graphene and CNT is in the area of catalysis. Hybrid materials of CNTs (or graphene) with metal nanoparticles can enable enhanced diffusion and fast transfer electron kinetics [87]. These hybrid catalysts have been used for various reactions, such as methane decomposition, methanol oxidation, ethylene hydroformylation, butene hydrogenation, and NO decomposition [88]. In addition, a number of promising results based on FLG as a catalytic support have been obtained [89].

2.5 Flame Synthesis

Flame synthesis is not as widely studied for material synthesis when compared to CVD, but it offers several key advantages such as scalability and cost effectiveness. The most commonly used flame types include premixed, normal diffusion, inverse diffusion, and co-flow (Fig. 2.22). Since the early 2000s a number of researchers have focused on the use of flames for CNT synthesis. However, the development of flame synthesis for graphene is still in its early stage. In addition to flame type, a number of parameters such as temperature, species concentration, and velocity impact the growth of CNTs or graphene.

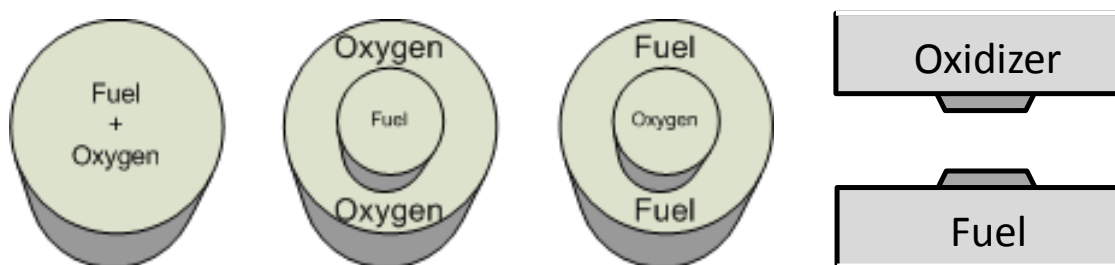


Figure 2.22 Premixed, Normal Diffusion, Inverse Diffusion, and Counter-flow Diffusion Burner Setups

2.5.1 Flame Synthesis of CNTs

A number of works have demonstrated the use of flames for CNT synthesis, utilizing normal diffusion, inverse diffusion, counter-flow, and premixed flames. A diffusion flame occurs when the oxidizer and fuel are initially separated, and mix through diffusion during the combustion process. Normal diffusion flame (over-ventilated flame) typically

comprises of two concentric tubes, where the fuel is inserted in the inner tube and oxidizer flows in the outer tube. An inverse diffusion flame (under-ventilated flame) has the opposite flow configuration (fuel in the outer tube and oxidizer in the inner tube) when compared to a normal diffusion flame. For over-ventilated flames, fuel rich species (such as CO and H₂) are only located inside the flame, while for under-ventilated flames, fuel rich species are present outside the flame (Fig. 2.23). This fundamental difference enables a wider growth region for CNTs when using an inverse diffusion flame as compared to using a normal diffusion flame. A counter-flow flame setup involves the use of two converging nozzles facing each other, where the oxidizer flows from one nozzle and the fuel flows from the other nozzle. A premixed flame (e.g. Bunsen flame) is established when the oxidizer and fuel are completely mixed before combusting.

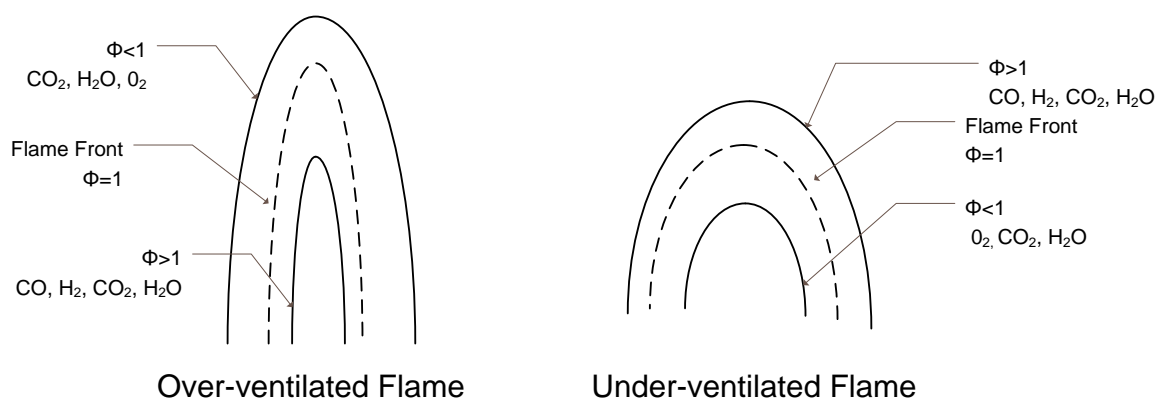


Figure 2.23 Flame profile of an over-ventilated and under-ventilated flame.

2.5.1.1 Normal Diffusion Flames

Yuan et al. [90] in 2001 reported the synthesis of MWNTs using a normal diffusion flame. The fuel, methane, was issued from a 1.1 cm diameters stainless-steel tube, which was surrounded by air flowing through a 5 cm diameter tube. The flame height (H) was

65mm. A Ni/Cr wire was inserted into the flame and held for 15-30 minutes. The optimal height for CNT growth was around $H/5$ to $H/3$. The wire contained MWNTs with a diameter between 20 to 60nm. Yuan et al. [91] also used the same burner with ethylene as the fuel and they found that the addition of nitrogen led to the alignment of MWNTs. This could also be due to the decrease in temperature when adding nitrogen.

Hu et al. [92] demonstrated the synthesis of well-aligned MWNTs using an ethylene diffusion flame. The CNTs were grown directly on a silicon substrate using thin-film anodic aluminum oxide (AAO) as the template. Catalytic cobalt particles were electrodeposited on the template. It was found that the diameter and length of the CNTs can be controlled using the template. The sample was placed 4 mm above the burner, where the flame diameter was around 10 mm. Hence the growth of CNTs was restricted to a small region within the flame, which is a limitation for scaled growth across large substrates. Vander Wal [93] also reported the growth of CNTs using a normal diffusion flame. Metal nanoparticles supported on TiO_2 were used as the catalyst. The shape of the nanoparticles determined the nanotube morphology, which were all MWNTs. It was shown that reactive radicals such as hydrogen can etch amorphous carbon and prevent pyrolytic carbon buildup.

2.5.1.2 Inverse Diffusion Flames

Lee et al. [94,95] in 2004 reported the growth of MWNTs using an inverse ethylene diffusion flame. The inner tube had a diameter of 11 mm, which used for air. The outer tube had a diameter 94 mm, which was used for nitrogen and ethylene. Air was supplied at a flow rate of 0.8 l/min, while the flow of ethylene and nitrogen was 5 and 30 l/min,

respectively. Stainless steel plates coated with $\text{Ni}(\text{NO}_3)_2$ were used as the substrate. Unlike a normal diffusion flame, no oxidizer was present outside the flame front, hence the growth of CNTs was observed 5 to 7 mm from the flame center in the radial direction. The growth of MWNTs was mostly observed in the temperature range of 1000 to 1300K, while the growth of nanofibers was commonly observed in the temperature range of 800K to 1000K. Unrau et al. [96] using an oxy-ethylene inverse diffusion flame reported the growth of SWNTs. Ferrocene was introduced through a bubbler as a floating catalyst, which enabled the growth of SWNTs.

Xu et al. [97] demonstrated the growth of well-aligned MWNTs using a methane inverse diffusion flame. A number of parameters including alloy composition (Fe, Ni/Cu, and Ni/Cr/Fe), sampling position, and applied voltage bias were investigated. Spontaneous Raman spectroscopy enabled local gas-phase temperature and carbon-based species (e.g. CO, C_2H_2) measurements. It was shown that the substrate composition, sampling position, temperature, and species concentration all impact the growth of CNTs. [Figure 2.24](#) depicts the influence of alloy composition and sampling position on the growth of CNTs. It is evident that such fluctuation in CNT quality based on sampling position would limit the scalable and uniform growth of CNTs across a large substrate.

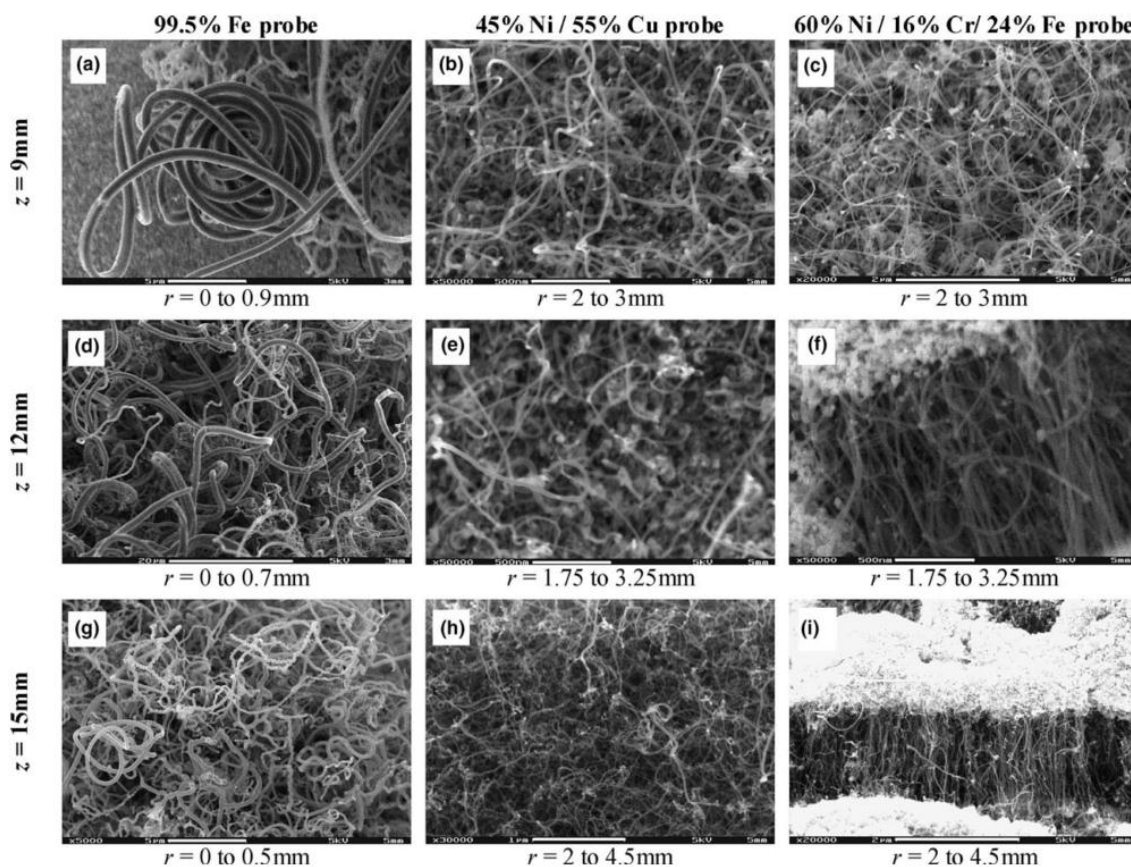


Figure 2.24 FESEM images of CNT morphology corresponding to catalytic probe composition (column) and flame sampling height (row). The alloy probes are operated at floating potential mode (FPM) for a 10 min sampling duration (reproduced with caption from [97]).

2.5.1.3 Counter flow diffusion Flames

The counter flow diffusion flame (CDF) was first used for the production of various oxide nanomaterials such as Al_2O_3 , SiO_2 , and GeO_2 [98,99], and more recently, the CDF burner has commonly been used for the growth of CNTs [100]. Xu et al. [101] demonstrated the growth of CNTs using a CDF burner on various metal alloys (i.e., Fe, Fe/Cr, Ni/Cu, Ni/Ti, Ni/Cr, and Ni/Cr/Fe). It was shown that the alloy composition

strongly impacts the growth of CNTs, along with gas-phase temperature, and local C_2H_2 concentration. Additionally, using spontaneous Raman spectroscopy a universal growth condition for CNTs was established that can be translated between different burner configurations. Merchan-Merchan and co-workers [102,103] also demonstrated the growth of CNTs using the CDF burner on a Ni alloy probe. Their study investigated different flame parameters and the application of an external electric field on the growth of CNTs. A catalytic probe was inserted using a protecting shield in the yellow soot region of the flame. Based on the flame height different morphologies of MWNTs were observed. The application of an external electrical field enabled the vertical alignment of MWNTs. Li et al. [104] investigated the growth of CNTs using the CDF burner on a Ni alloy probe and a Si substrate coated with porous anodic aluminum oxide. The flame profile of a CDF burner is well understood by the combustion community and is well-suited for the fundamental investigation of nanomaterial synthesis. A limitation of the CDF flame is the inability to grow CNTs across large regions due to the temperature and concentration gradients. Additionally, the growth typically occurs on a wire probe, as any large substrate would impact the flow structure of the CDF flame.

2.5.1.4 Premixed Flames

The use of a premixed flame for CNT synthesis was first reported by Duan and McKinnon in 1994 [105]. MWNTs were observed in a fuel rich benzene-air premixed flame at low pressure. Significant amount of amorphous soot was also present. Chowdhury et al. in 1995 [106] observed the presence of fullerenes and MWNTs using benzene, acetylene, and ethylene premixed flames at low pressures.

Vander Wal et al. [107] investigated the effects of fuel on the growth of CNTs using a premixed flame. Cobalt was used as the catalyst for CNT growth and the gas temperature was 800°C. The growth of MWNTs was observed using an ethane, ethylene, acetylene, and propane fuel rich flame. However the growth of CNTs was not observed using a methane flame, at a fuel rich equivalence ratio from 1.5 to 2. This is contrary to the results reported using a diffusion flame, where the growth of CNTs is observed using a methane flame.

A study comparing the use of a premixed and diffusion flame for CNT and fullerene growth was performed by Goel et al [108]. Benzene was used as the fuel and it was found that a diffusion flame results in a higher yield of CNTs. Additionally, the growth of CNTs using a premixed flame is strongly dependent on the residence time.

Woo et al. [109] used a double-faced wall stagnation flow burner for the production of CNTs. Each burner operated in a premixed mode with ethylene as the fuel. A Ni-coated plate was used as the catalyst and MWNTs were observed on the substrate. The use of a stagnation flame represents a scalable method for the growth of CNTs on a substrate.

Height et al. [110] using an acetylene premixed flame reported the growth of SWNTs. Iron pentacarbonyl was introduced through a bubbler as a floating catalyst, which enabled the growth of SWNTs. Thermophoretic sampling was used to collect the CNTs at different temperatures, 1500 to 1800 K, and different equivalence ratios, 1.5 to 1.9. The diameters of the individual CNTs were between 0.9 and 1.5nm.

The use of premixed flames has emerged as an alternative to CVD for CNT production [62]. However, there are still a number of challenges associated with using premixed flames for CNT production, such as catalyst poisoning due to soot precursors.

Therefore, it is important to develop flames free of soot such as an inverse diffusion flame [96]. Additionally, by using diffusion flames (burning stoichiometrically in the reaction zone), flame speed, flashback, and cellular instabilities related to premixed flames are avoided.

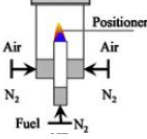




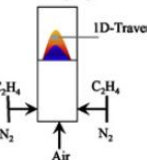

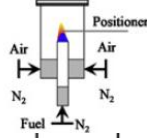

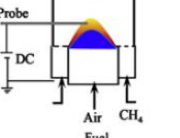

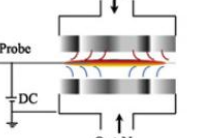

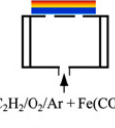

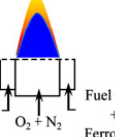

Author	Burner Configuration	Flame Type	Fuel/Oxidizer	Catalytic Material	Catalyst Delivery	CNT Type
Yuan et al. [60,61]		Co-flow diffusion	CH ₄ [54] & C ₂ H ₄ [61]/Air	Stainless steel and Ni-Cr-Fe	Solid support (stainless steel grid held by a Ni-Cr-Fe wire-(i)- [60,61] and electroplated with cobalt-(ii)- [61])	Entangle [60,61], straight & bamboo-like (i), and aligned MWCNT (ii) [61]  
Howard et al. [58]		Premixed	C ₆ H ₆ , C ₂ H ₂ , C ₂ H ₄ / O ₂ +diluent	None	None	Fullerenes & multi-shell nanotubes 
Lee et al. [62]		Inverse diffusion	C ₂ H ₄ /Air	Stainless steel and Ni(NO ₃) ₂	Solid support (Stainless steel plate coated with Ni(NO ₃) ₂)	MWCNT & CNF 
Hu et al. [86]		Co-flow diffusion	C ₂ H ₄ /Air	Cobalt	Solid support (AAO electroplated with cobalt)	Aligned-MWCNT 
Xu et al. [66]		Co-flow diffusion	CH ₄ /Air	Transition metal alloy probes with various compositions (e.g. Fe, Ni/Cu, and Ni/Cr/Fe)	Solid support (transition metal alloy wires with various compositions, e.g. Fe, Ni/Cu, and Ni/Cr/Fe)	MWCNTs & WACNTs 
Merchan-Merchan et al. [69]		Counter-flow diffusion	CH ₄ +C ₂ H ₂ /N ₂ +O ₂	Ni based alloy (73% Ni+17%Cu+10%Fe)	Solid support (Ni based alloy wire)	Coiled, helically, branching & VACNTs CNTs 
Height et al. [121,122]		Premixed	C ₂ H ₂ /O ₂ -Ar	Iron pentacarbonyl - Fe(CO) ₅	Argon gas	SWCNT 
Unrau et al. [134]		Inverse diffusion	C ₂ H ₄ /O ₂	Ferrocene	Fuel + Nitrogen gases mixture	SWCNT 

Table 2.9 Summary of different flame configurations used for CNT synthesis (reproduced from [62]).

2.5.2 Flame Synthesis of Graphene

Whereas a number of different flame configurations have been used for the production of CNTs, the number of reports on the flame synthesis of graphene has been limited. While a key reason for this discrepancy is that graphene was only recently discovered (2004) when compared to CNTs (1991). Another important reason is that the flame synthesis of graphene is more challenging when compared to CNTs. Graphene being a two-dimensional material requires large-scale production across a substrate. Due to the temperature and species gradients that occur in most flames, it is difficult to scale the growth of graphene across an entire substrate. Moreover, a reduced environment with carbon rich species, which is necessary for graphene growth, is difficult to achieve in most flames.

Similar to earlier CNT flame synthesis research results, where the growth of CNTs was observed near the soot region of a premixed flame, carbon particles containing graphene were observed in a Bunsen (propane) flame [111]. These particles were collected by placing a transmission electron microscopy (TEM) grid 2 cm above the tip of the burner. The grid was held within the flame for 10 to 50ms. The graphene films were several hundreds of nanometers in size.

In an attempt to grow graphene on copper, Li et al. [112] investigated the growth of graphene using an ethanol burner. The substrate was placed within the flame at a temperature of 550 to 700°C and the flame was extinguished using a cap to prevent the oxidation of the copper foil. The growth of an amorphous carbon film was observed on the substrate and XPS confirmed the formation of sp^2 , sp^3 and C-O bonded atoms. Graphene was not observed due to the low-temperature and the presence of oxygen

within the flame. In a different experiment, Li et al. [113] were able to successfully synthesize graphene on nickel. The process utilized two different burners (burner 1 and burner 2); with the substrate situated within the interior region of the flame structure itself (Fig. 2.25). Burner 1 (alcohol burner) surrounded the substrate for the entire time, thus it prevented air oxidation and served as the carbon source. Burner 2 (butane-fueled Bunsen burner) provided the additional heating of the substrate and served as the carbon source for graphene growth as well (also referred as the carburization flame in Fig. 2.25). The flame was extinguished using a cap. Although the viability of flame synthesis for graphene growth was demonstrated, the process resulted in the formation of amorphous carbon impurities along with the graphene. Moreover, the configuration may not readily be scalable for large-area graphene production.

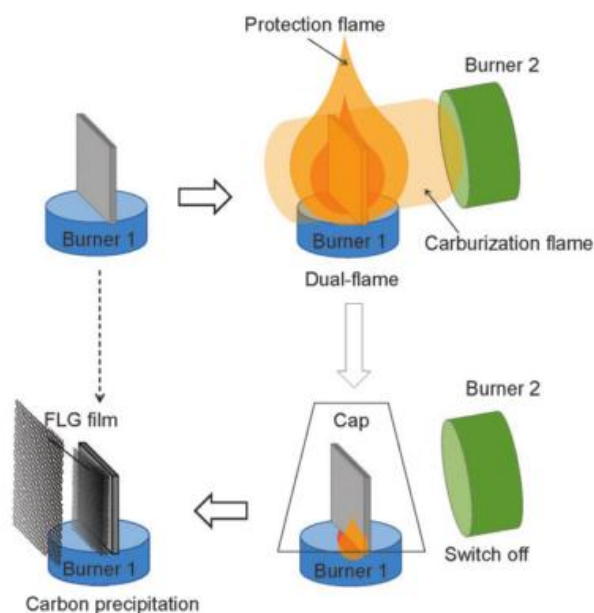


Figure 2.25 Schematic of the flame synthesis of FLG on a nickel foil (reproduced from [113]).

2.5.3 Scalable Flame Synthesis of Metal Oxides

Similar to CNTs, a number of burner configurations have been used for the production of metal-oxides. A particularly exciting burner configuration is the use of multiple diffusion flames, where uniform temperatures can be established downstream from the burner. Similar to a single diffusion flame, the multiple diffusion flame can either operate in a normal or inverse mode. Prior to the work reported in this thesis, the multiple diffusion flame was only operated in a normal configuration mode, where it was used for the scalable synthesis of SiO_2 [114], Fe_2O_3 [115], CuO [115], WO_3 [116], and MoO_3 [117].

2.6 Summary

Graphene and CNTs with their remarkable photonic, electrical, and mechanical properties have attracted significant research interest. These properties afford a wide range of applications, such as flexible touch panels, thin-film transistors, solar panels, and corrosion resistant coatings. Three components are typically necessary for graphene and CNT synthesis: carbon, heat, and the presence of certain metals. CVD is the most prevalent technology that is currently used for the synthesis of CNTs and graphene. Flame synthesis, which readily provides high temperatures and precursor carbon species, serves as a scalable method for the production of carbon nanomaterials.

2.7 References

- [1] Kratschmer W, Lamb LD, Fostiropoulos K, Huffman DR. Solid C₆₀: a new form of carbon. *Nature* 1990;347:354-8.
- [2] http://en.wikipedia.org/wiki/Allotropes_of_carbon ;2012.
- [3] Pierson HO. *Handbook of Carbon, Graphite, Diamonds and Fullerenes: Processing, Properties and Applications*. 1st ed. : William Andrew, 1995.
- [4] Fasolino A, Los JH, Katsnelson MI. Intrinsic ripples in graphene. *Nat Mater* 2007;6:858-61.
- [5] Meyer JC, Kisielowski C, Erni R, Rossell MD, Crommie MF, Zettl A. Direct Imaging of Lattice Atoms and Topological Defects in Graphene Membranes. *Nano Lett* 2008;8:3582-6.
- [6] Oostinga JB, Heersche HB, Liu X, Morpurgo AF, Vandersypen LMK. Gate-induced insulating state in bilayer graphene devices. *Nat Mater* 2008;7:151-7.
- [7] Zhang Y, Tan Y, Stormer HL, Kim P. Experimental observation of the quantum Hall effect and Berry's phase in graphene. *Nature* 2005;438:201-4.
- [8] Novoselov KS, Jiang D, Schedin F, Booth TJ, Khotkevich VV, Morozov SV et al. Two-dimensional atomic crystals. *Proc Natl Acad Sci U S A* 2005;102:10451-3.
- [9] Geim AK, Novoselov KS. The rise of graphene. *Nat Mater* 2007;6:183-91.
- [10] Bolotin KI, Sikes KJ, Jiang Z, Klima M, Fudenberg G, Hone J et al. Ultrahigh electron mobility in suspended graphene. *Solid State Commun* 2008;146:351-5.
- [11] Singh V, Joung D, Zhai L, Das S, Khondaker SI, Seal S. Graphene based materials: Past, present and future. *Progress in Materials Science* 2011;56:1178-271.
- [12] Lee C, Wei X, Kysar JW, Hone J. Measurement of the Elastic Properties and Intrinsic Strength of Monolayer Graphene. *Science* 2008;321:385-8.
- [13] Lee C, Wei X, Li Q, Carpick R, Kysar JW, Hone J. Elastic and frictional properties of graphene. *physica status solidi (b)* 2009;246:2562-7.
- [14] Tsoukleri G, Parthenios J, Papagelis K, Jalil R, Ferrari AC, Geim AK et al. Subjecting a Graphene Monolayer to Tension and Compression. *Small* 2009;5:2397-402.

- [15] Bonaccorso F, Sun Z, Hasan T, Ferrari AC. Graphene photonics and optoelectronics. *Nat Photon* 2010;4:611-22.
- [16] de Heer WA, Berger C, Wu X, First PN, Conrad EH, Li X et al. Epitaxial graphene. *Solid State Commun* 2007;143:92-100.
- [17] Zhu Y, Murali S, Cai W, Li X, Suk JW, Potts JR et al. Graphene and Graphene Oxide: Synthesis, Properties, and Applications. *Adv Mater* 2010;22:3906-24.
- [18] Ni ZH, Wang HM, Kasim J, Fan HM, Yu T, Wu YH et al. Graphene Thickness Determination Using Reflection and Contrast Spectroscopy. *Nano Lett* 2007;7:2758-63.
- [19] Nair RR, Blake P, Grigorenko AN, Novoselov KS, Booth TJ, Stauber T et al. Fine Structure Constant Defines Visual Transparency of Graphene. *Science* 2008;320:1308-.
- [20] Balandin AA, Ghosh S, Bao W, Calizo I, Teweldebrhan D, Miao F et al. Superior Thermal Conductivity of Single-Layer Graphene. *Nano Lett* 2008;8:902-7.
- [21] Seol JH, Jo I, Moore AL, Lindsay L, Aitken ZH, Pettes MT et al. Two-Dimensional Phonon Transport in Supported Graphene. *Science* 2010;328:213-6.
- [22] Balandin AA. Thermal properties of graphene and nanostructured carbon materials. *Nat Mater* 2011;10:569-81.
- [23] Nika DL, Pokatilov EP, Askerov AS, Balandin AA. Phonon thermal conduction in graphene: Role of Umklapp and edge roughness scattering. *Phys Rev B* 2009;79:155413.
- [24] Jiang J, Lan J, Wang J, Li B. Isotopic effects on the thermal conductivity of graphene nanoribbons: Localization mechanism. *J Appl Phys* 2010;107:054314-5.
- [25] Timo Schwamb and Brian R Burg and Niklas C Schirmer and Dimos Poulikakos. An electrical method for the measurement of the thermal and electrical conductivity of reduced graphene oxide nanostructures. *Nanotechnology* 2009;20:405704.
- [26] Geim AK, Novoselov KS. The rise of graphene. *Nat Mater* 2007;6:183-91.
- [27] Novoselov KS, Geim AK, Morozov SV, Jiang D, Katsnelson MI, Grigorieva IV et al. Two-dimensional gas of massless Dirac fermions in graphene. *Nature* 2005;438:197-200.
- [28] Hernandez Y, Nicolosi V, Lotya M, Blighe FM, Sun Z, De S et al. High-yield production of graphene by liquid-phase exfoliation of graphite. *Nat Nano* 2008;3:563-8.

- [29] Lotya M, Hernandez Y, King PJ, Smith RJ, Nicolosi V, Karlsson LS et al. Liquid Phase Production of Graphene by Exfoliation of Graphite in Surfactant/Water Solutions. *J Am Chem Soc* 2009;131:3611-20.
- [30] Green AA, Hersam MC. Solution Phase Production of Graphene with Controlled Thickness via Density Differentiation. *Nano Lett* 2009;9:4031-6.
- [31] Li X, Wang X, Zhang L, Lee S, Dai H. Chemically Derived, Ultrasooth Graphene Nanoribbon Semiconductors. *Science* 2008;319:1229-32.
- [32] Bonaccorso F, Sun Z, Hasan T, Ferrari AC. Graphene photonics and optoelectronics. *Nat Photon* 2010;4:611-22.
- [33] Eda G, Fanchini G, Chhowalla M. Large-area ultrathin films of reduced graphene oxide as a transparent and flexible electronic material. *Nat Nano* 2008;3:270-4.
- [34] Yamaguchi H, Eda G, Mattevi C, Kim H, Chhowalla M. Highly Uniform 300 mm Wafer-Scale Deposition of Single and Multilayered Chemically Derived Graphene Thin Films. *ACS Nano* 2010;4:524-8.
- [35] Machado BF, Serp P. Graphene-based materials for catalysis. *Catal Sci Technol* 2012;2.
- [36] Aristov VY, Urbanik G, Kummer K, Vyalikh DV, Molodtsova OV, Preobrajenski AB et al. Graphene Synthesis on Cubic SiC/Si Wafers. Perspectives for Mass Production of Graphene-Based Electronic Devices. *Nano Letters* 2010; 2010;10:992-5.
- [37] Emtsev KV, Bostwick A, Horn K, Jobst J, Kellogg GL, Ley L et al. Towards wafer-size graphene layers by atmospheric pressure graphitization of silicon carbide. *Nat Mater* 2009;8:203-7.
- [38] Mattevi C, Kim H, Chhowalla M. A review of chemical vapour deposition of graphene on copper. *J Mater Chem* 2011;21:3324-34.
- [39] Obraztsov AN, Obraztsova EA, Tyurnina AV, Zolotukhin AA. Chemical vapor deposition of thin graphite films of nanometer thickness. *Carbon* 2007;45:2017-21.
- [40] Chae SJ, GÃ¼neÅŸ F, Kim KK, Kim ES, Han GH, Kim SM et al. Synthesis of Large-Area Graphene Layers on Poly-Nickel Substrate by Chemical Vapor Deposition: Wrinkle Formation. *Adv Mater* 2009;21:2328-33.
- [41] Li X, Cai W, An J, Kim S, Nah J, Yang D et al. Large-Area Synthesis of High-Quality and Uniform Graphene Films on Copper Foils. *Science* 2009;324:1312-4.

- [42] Bhaviripudi S, Jia X, Dresselhaus MS, Kong J. Role of Kinetic Factors in Chemical Vapor Deposition Synthesis of Uniform Large Area Graphene Using Copper Catalyst. *Nano Letters* 2010; 2010;10:4128-33.
- [43] Bae S, Kim H, Lee Y, Xu X, Park J, Zheng Y et al. Roll-to-roll production of 30-inch graphene films for transparent electrodes. *Nat Nano* 2010;5:574-8.
- [44] Yao Y, Li Z, Lin Z, Moon K, Agar J, Wong C. Controlled Growth of Multilayer, Few-Layer, and Single-Layer Graphene on Metal Substrates. *J Phys Chem C* 2011;115:5232-8.
- [45] Li X, Cai W, Colombo L, Ruoff RS. Evolution of Graphene Growth on Ni and Cu by Carbon Isotope Labeling. *Nano Letters* 2009; 2009;9:4268-72.
- [46] Li X, Zhu Y, Cai W, Borysiak M, Han B, Chen D et al. Transfer of Large-Area Graphene Films for High-Performance Transparent Conductive Electrodes. *Nano Letters* 2009; 2009;9:4359-63.
- [47] Srivastava A, Galande C, Ci L, Song L, Rai C, Jariwala D et al. Novel Liquid Precursor-Based Facile Synthesis of Large-Area Continuous, Single, and Few-Layer Graphene Films. *Chem Mater* 2010;22:3457-61.
- [48] Zhu M, Wang J, Holloway BC, Outlaw RA, Zhao X, Hou K et al. A mechanism for carbon nanosheet formation. *Carbon* 2007;45:2229-34.
- [49] Kim J, Ishihara M, Koga Y, Tsugawa K, Hasegawa M, Iijima S. Low-temperature synthesis of large-area graphene-based transparent conductive films using surface wave plasma chemical vapor deposition. *Appl Phys Lett* 2011;98:091502-3.
- [50] Yuan GD, Zhang WJ, Yang Y, Tang YB, Li YQ, Wang JX et al. Graphene sheets via microwave chemical vapor deposition. *Chemical Physics Letters* 2009;467:361-4.
- [51] Wang J, Zhu M, Outlaw RA, Zhao X, Manos DM, Holloway BC. Synthesis of carbon nanosheets by inductively coupled radio-frequency plasma enhanced chemical vapor deposition. *Carbon* 2004;42:2867-72.
- [52] Barone V, Hod O, Scuseria GE. Electronic Structure and Stability of Semiconducting Graphene Nanoribbons. *Nano Lett* 2006;6:2748-54.
- [53] Cappelli E, Scilletta C, Orlando S, Flammini R, Iacobucci S, Ascarelli P. Surface characterisation of nano-structured carbon films deposited by Nd:YAG pulsed laser deposition. *Thin Solid Films* 2005;482:305-10.
- [54] Thostenson ET, Ren Z, Chou T. Advances in the science and technology of carbon nanotubes and their composites: a review. *Composites Sci Technol* 2001;61:1899-912.

- [55] Hongjie D. Carbon nanotubes: opportunities and challenges. *Surf Sci* 2002;500:218-41.
- [56] Yu M, Lourie O, Dyer MJ, Moloni K, Kelly TF, Ruoff RS. Strength and Breaking Mechanism of Multiwalled Carbon Nanotubes Under Tensile Load. *Science* 2000;287:637-40.
- [57] Ruoff RS, Lorents DC. Mechanical and thermal properties of carbon nanotubes. *Carbon* 1995;33:925-30.
- [58] Berber S, Kwon Y, Tománek D. Unusually High Thermal Conductivity of Carbon Nanotubes. *Phys Rev Lett* 2000;84:4613-6.
- [59] Ajayan PM. Nanotubes from Carbon. *Chem Rev* 1999;99:1787-800.
- [60] Iijima S. Helical Microtubules of Graphitic Carbon. *Nature* 1991;354:56-.
- [61] Ebbesen TW, Ajayan PM. Large-scale synthesis of carbon nanotubes. *Nature* 1992;358:220-2.
- [62] Merchan-Merchan W, Saveliev AV, Kennedy L, Jimenez WC. Combustion synthesis of carbon nanotubes and related nanostructures. *Progress in Energy and Combustion Science* 2010;36:696-727.
- [63] Ando Y, Zhao X, Sugai T, Kumar M. Growing carbon nanotubes. *Materials Today* 2004;7:22-9.
- [64] Xu F. Investigating flame-based synthesis of carbon nanotubes and metal-oxide nanowires. Rutgers University 2007.
- [65] Tanemura M, Iwata K, Takahashi K, Fujimoto Y, Okuyama F, Sugie H et al. Growth of aligned carbon nanotubes by plasma-enhanced chemical vapor deposition: Optimization of growth parameters. *J Appl Phys* 2001;90:1529.
- [66] Bronikowski MJ, Willis PA, Colbert DT, Smith KA, Smalley RE. Gas-phase production of carbon single-walled nanotubes from carbon monoxide via the HiPco process: A parametric study. *J Vac Sci Technol A* 2001;19:1800-5.
- [67] Zhu Y, Murali S, Cai W, Li X, Suk JW, Potts JR et al. Graphene and Graphene Oxide: Synthesis, Properties, and Applications. *Adv Mater* 2010;22:3906-24.
- [68] Kong J, Franklin NR, Zhou C, Chapline MG, Peng S, Cho K et al. Nanotube Molecular Wires as Chemical Sensors. *Science* 2000;287:622-5.

- [69] Adu CKW, Sumanasekera GU, Pradhan BK, Romero HE, Eklund PC. Carbon nanotubes: A thermoelectric nano-nose. *Chemical Physics Letters* 2001;337:31-5.
- [70] Varghese OK, Kichambre PD, Gong D, Ong KG, Dickey EC, Grimes CA. Gas sensing characteristics of multi-wall carbon nanotubes. *Sensors Actuators B: Chem* 2001;81:32-41.
- [71] Ting Zhang and Syed Mubeen and Nosang V Myung and Marc,A.Deshusses. Recent progress in carbon nanotube-based gas sensors. *Nanotechnology* 2008;19:332001.
- [72] Leenaerts O, Partoens B, Peeters FM. Adsorption of H₂O, NH₃, CO, NO₂, and NO on graphene: A first-principles study. *Phys Rev B* 2008;77:125416.
- [73] Jeong HY, Lee D, Choi HK, Lee DH, Kim J, Lee JY et al. Flexible room-temperature NO₂ gas sensors based on carbon nanotubes/reduced graphene hybrid films. *Appl Phys Lett* 2010;96:213105-3.
- [74] Roth S, Park HJ. Nanocarbonic transparent conductive films. *Chem Soc Rev* 2010;39:2477-83.
- [75] Chang Liu aH. Carbon nanotubes for clean energy applications. *J Phys D* 2005;38:R231.
- [76] Niu C, Sichel EK, Hoch R, Moy D, Tennent H. High power electrochemical capacitors based on carbon nanotube electrodes. *Appl Phys Lett* 1997;70:1480-2.
- [77] Vivekchand S, Rout C, Subrahmanyam K, Govindaraj A, Rao C. Graphene-based electrochemical supercapacitors. *Journal of Chemical Sciences* 2008;120:9-13.
- [78] Sun Y, Wu Q, Shi G. Graphene based new energy materials. *Energy Environ Sci* 2011;4:1113-32.
- [79] Yoo E, Kim J, Hosono E, Zhou H, Kudo T, Honma I. Large Reversible Li Storage of Graphene Nanosheet Families for Use in Rechargeable Lithium Ion Batteries. *Nano Lett* 2008;8:2277-82.
- [80] Lin Y-, Dimitrakopoulos C, Jenkins KA, Farmer DB, Chiu H-, Grill A et al. 100-GHz Transistors from Wafer-Scale Epitaxial Graphene. *Science* 2010;327:662-.
- [81] Wu Y, Lin Y, Bol AA, Jenkins KA, Xia F, Farmer DB et al. High-frequency, scaled graphene transistors on diamond-like carbon. *Nature* 2011;472:74-8.
- [82] Zhang Y, Tang T, Girit C, Hao Z, Martin MC, Zettl A et al. Direct observation of a widely tunable bandgap in bilayer graphene. *Nature* 2009;459:820-3.

- [83] Breuer O, Sundararaj U. Big returns from small fibers: A review of polymer/carbon nanotube composites. *Polymer Composites* 2004;25:630-45.
- [84] Gibson RF, Ayorinde EO, Wen Y. Vibrations of carbon nanotubes and their composites: A review. *Composites Sci Technol* 2007;67:1-28.
- [85] Liang J, Huang Y, Zhang L, Wang Y, Ma Y, Guo T et al. Molecular-Level Dispersion of Graphene into Poly(vinyl alcohol) and Effective Reinforcement of their Nanocomposites. *Advanced Functional Materials* 2009;19:2297-302.
- [86] Chen S, Brown L, Levendoff M, Cai W, Ju S, Edgeworth J et al. Oxidation Resistance of Graphene-Coated Cu and Cu/Ni Alloy. *ACS Nano* 2011;5:1321-7.
- [87] Vairavapandian D, Vichchulada P, Lay MD. Preparation and modification of carbon nanotubes: Review of recent advances and applications in catalysis and sensing. *Anal Chim Acta* 2008;626:119-29.
- [88] Serp P, Corrias M, Kalck P. Carbon nanotubes and nanofibers in catalysis. *Applied Catalysis A: General* 2003;253:337-58.
- [89] Machado BF, Serp P. Graphene-based materials for catalysis. *Catal Sci Technol* 2012;2:54-75.
- [90] Yuan L, Saito K, Pan C, Williams FA, Gordon AS. Nanotubes from methane flames. *Chemical Physics Letters* 2001;340:237-41.
- [91] Yuan L, Saito K, Hu W, Chen Z. Ethylene flame synthesis of well-aligned multi-walled carbon nanotubes. *Chemical Physics Letters* 2001;346:23-8.
- [92] Hu W, Yuan L, Chen Z, Gong D, Saito K. Fabrication and Characterization of Vertically Aligned Carbon Nanotubes on Silicon Substrates Using Porous Alumina Nanotemplates. *Journal of Nanoscience and Nanotechnology* 2002;2:203-7.
- [93] Randall L. VW. Flame synthesis of substrate-supported metal-catalyzed carbon nanotubes. *Chemical Physics Letters* 2000;324:217-23.
- [94] Lee GW, Jurng J, Hwang J. Formation of Ni-catalyzed multiwalled carbon nanotubes and nanofibers on a substrate using an ethylene inverse diffusion flame. *Combust Flame* 2004;139:167-75.
- [95] Woo Lee G, Jurng J, Hwang J. Synthesis of carbon nanotubes on a catalytic metal substrate by using an ethylene inverse diffusion flame. *Carbon* 2004;42:682-5.

- [96] Unrau CJ, Axelbaum RL, Biswas P, Fraundorf P. Synthesis of single-walled carbon nanotubes in oxy-fuel inverse diffusion flames with online diagnostics. *Proceedings of the Combustion Institute* 2007;31:1865-72.
- [97] Xu F, Liu X, Tse SD. Synthesis of carbon nanotubes on metal alloy substrates with voltage bias in methane inverse diffusion flames. *Carbon* 2006;44:570-7.
- [98] Chung S, Katz JL. The counterflow diffusion flame burner: A new tool for the study of the nucleation of refractory compounds. *Combust Flame* 1985;61:271-84.
- [99] Rosner DE. Flame Synthesis of Valuable Nanoparticles: Recent Progress/Current Needs in Areas of Rate Laws, Population Dynamics, and Characterization. *Ind Eng Chem Res* 2005;44:6045-55.
- [100] Merchan-Merchan W, Saveliev AV, Kennedy L, Jimenez WC. Combustion synthesis of carbon nanotubes and related nanostructures. *Progress in Energy and Combustion Science* 2010;36:696-727.
- [101] Xu F, Zhao H, Tse SD. Carbon nanotube synthesis on catalytic metal alloys in methane/air counterflow diffusion flames. *Proceedings of the Combustion Institute* 2007;31:1839-47.
- [102] Merchan-Merchan W, Saveliev AV, Kennedy LA. High-rate flame synthesis of vertically aligned carbon nanotubes using electric field control. *Carbon* 2004;42:599-608.
- [103] Saveliev AV, Merchan-Merchan W, Kennedy LA. Metal catalyzed synthesis of carbon nanostructures in an opposed flow methane oxygen flame. *Combust Flame* 2003;135:27-33.
- [104] Li TX, Zhang HG, Wang FJ, Chen Z, Saito K. Synthesis of carbon nanotubes on Ni-alloy and Si-substrates using counterflow methane-air diffusion flames. *Proceedings of the Combustion Institute* 2007;31:1849-56.
- [105] Duan HM, McKinnon JT. Nanoclusters Produced in Flames. *J Phys Chem* 1994;98:12815-8.
- [106] Das Chowdhury K, Howard JB, VanderSande JB. Fullerene nanostructures in flames *J Mater Res* 2011; 1996;11:341 <last_page> 347.
- [107] Vander Wal RL, Hall LJ, Berger GM. Optimization of Flame Synthesis for Carbon Nanotubes Using Supported Catalyst. *J Phys Chem B* 2002;106:13122-32.
- [108] Goel A, Hebggen P, Vander Sande JB, Howard JB. Combustion synthesis of fullerenes and fullerene nanostructures. *Carbon* 2002;40:177-82.

- [109] Woo SK, Hong YT, Kwon OC. Flame-synthesis limits and self-catalytic behavior of carbon nanotubes using a double-faced wall stagnation flow burner. *Combust Flame* 2009;156:1983-92.
- [110] Height MJ, Howard JB, Tester JW, Vander Sande JB. Flame synthesis of single-walled carbon nanotubes. *Carbon* 2004;42:2295-307.
- [111] Ossler F, Wagner JB, Canton SE, Wallenberg LR. Sheet-like carbon particles with graphene structures obtained from a Bunsen flame. *Carbon* 2010;48:4203-6.
- [112] Li Z, Zhu H, Wang K, Wei J, Gui X, Li X et al. Ethanol flame synthesis of highly transparent carbon thin films. *Carbon* 2011;49:237-41.
- [113] Li Z, Zhu H, Xie D, Wang K, Cao A, Wei J et al. Flame synthesis of few-layered graphene/graphite films. *Chem Commun* 2011;47:3520-2.
- [114] Wooldridge MS, Torek PV, Donovan MT, Hall DL, Miller TA, Palmer TR et al. An experimental investigation of gas-phase combustion synthesis of SiO₂ nanoparticles using a multi-element diffusion flame burner. *Combust Flame* 2002;131:98-109.
- [115] Rao PM, Zheng X. Rapid Catalyst-Free Flame Synthesis of Dense, Aligned $\hat{\Gamma}$ -Fe₂O₃ Nanoflake and CuO Nanoneedle Arrays. *Nano Lett* 2009;9:3001-6.
- [116] Rao PM, Zheng X. Flame synthesis of tungsten oxide nanostructures on diverse substrates. *Proceedings of the Combustion Institute* 2011;33:1891-8.
- [117] Cai L, Rao PM, Zheng X. Morphology-Controlled Flame Synthesis of Single, Branched, and Flower-like $\hat{\Gamma}$ -MoO₃ Nanobelt Arrays. *Nano Lett* 2011;11:872-7.

Chapter 3

3. Experimental Setup

The experimental setup and characterization of graphene and CNTs from flame synthesis are discussed in this chapter. A multiple inverse-diffusion burner is used in the synthesis of graphene and CNTs. The characterization techniques utilized include Raman spectroscopy, field-emission scanning electron microscopy (FESEM), transmission electron microscopy (TEM), x-ray photoelectron spectroscopy (XPS), and atomic force microscopy (AFM) .

3.1 Multiple Inverse-Diffusion Burner Setup

The multiple inverse-diffusion setup ([Fig. 3.1](#)) is where each individual diffusion flame runs in an inverse mode (“under-ventilated”). Water is used to cool the burner and a quartz cylinder encompasses the region of the multiple flames. This prevents oxidizer permeation from the ambient and directs optimal gas-phase conditions (i.e. species and temperature) to the substrate. Oxidizer (e.g. air or O_2) enters only through the small individual stainless steel tubes, while the fuel (e.g. methane, ethylene, acetylene, hydrogen, etc.) flows around the tubes. The top-view of the burner is illustrated in [Fig. 3.2](#), where a honeycomb fixture is used to mount the tubes. The fuel flows in all empty cells, while the oxidizer flows in the cells with an inserted tube. Note that the setup is open to atmospheric conditions. For dimensional information of the burner setup please refer to the appendix.

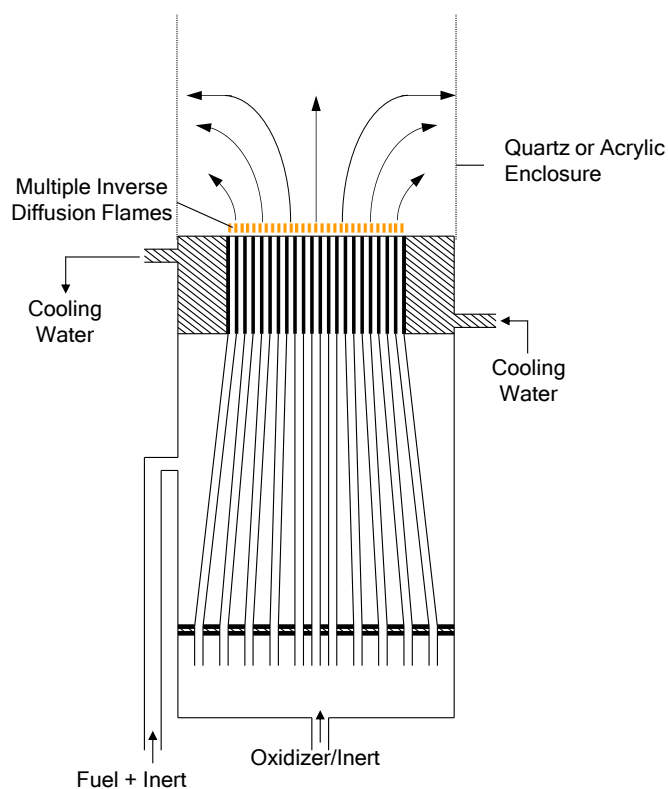


Figure 3.1 Schematic of the multiple inverse-diffusion flame.

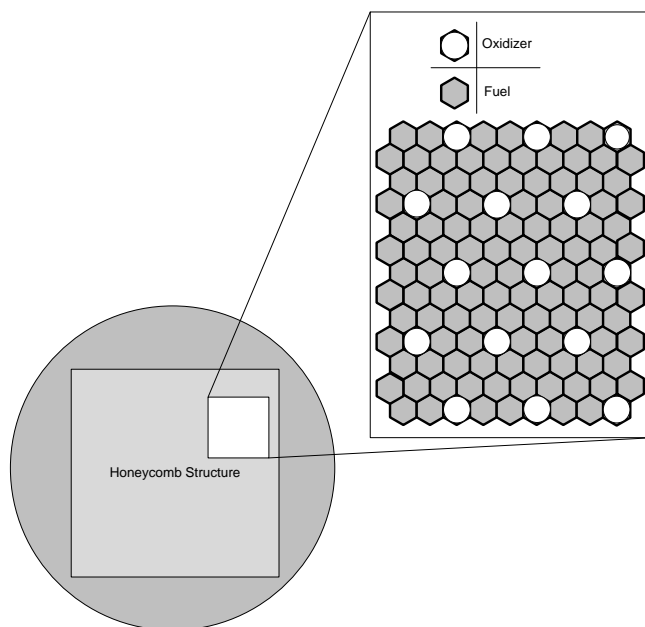


Figure 3.2 Top-view of the multiple inverse-diffusion flame.

A detailed schematic of the experimental setup is shown in Fig. 3.3. Mass flow controllers (MFCs) from Emcore are used to precisely regulate the gas flow rates. A computer program using Labview is used to control the MFCs, which ensures the reproducibility of the experiment and reduces any experimental error. An after-burner is mounted outside the quartz tube to consume any excess fuel. A sidewall slot is machined within the quartz tube to allow access for an igniter and thermocouple. A rod is inserted from the top to hold the substrate. The setup is mounted onto an optical table, where it can easily be moved in any direction. Please refer to the appendix for information on the fuel and oxidizer flow rates.

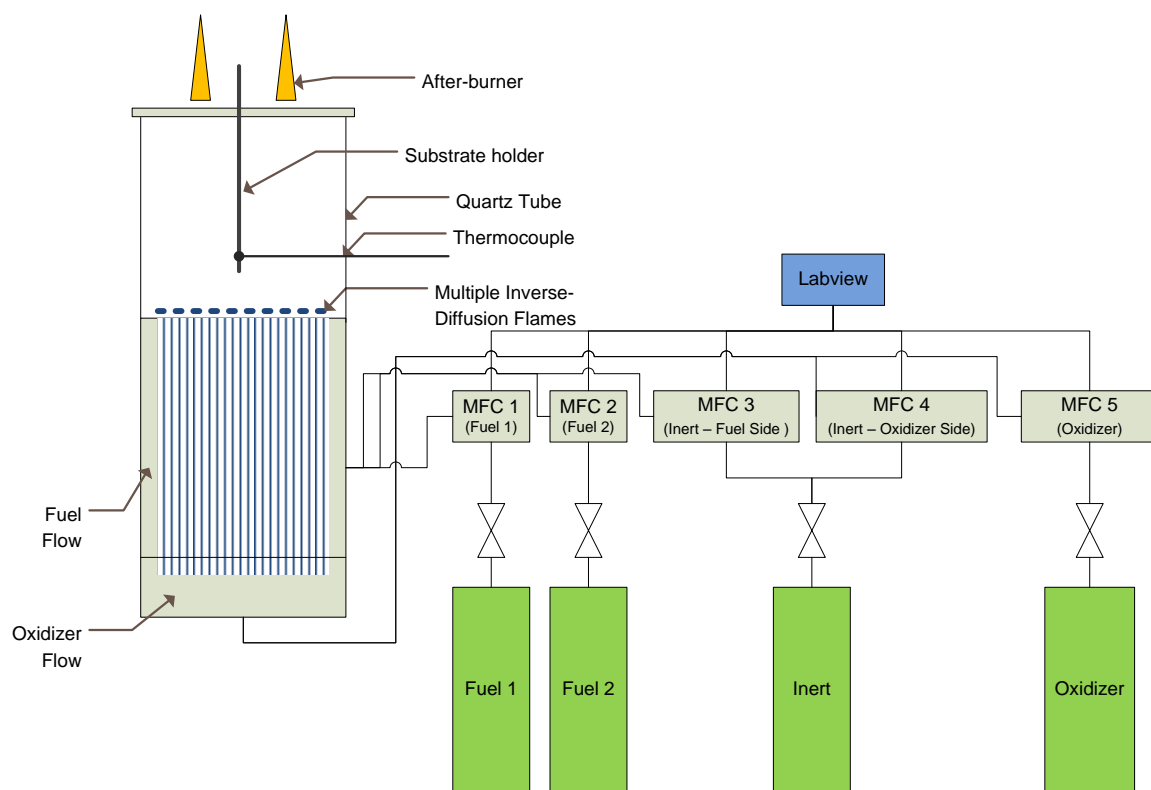


Figure 3.3 Schematic diagram of the experimental setup involving the use of a multiple-inverse diffusion flame. (MFC stands for mass flow controller).

3.2 Thermocouple (TC) and its coating

The gas phase temperature is measured using a 125 μm Pt/Pt-10%Rh thermocouple (S-type) (OMEGA, Model: P10R-005). To prevent catalytic oxidation on the platinum-based thermocouple, a silica coating is applied. This coating is performed using a small burner, where silicon oil is injected using a syringe pump. The thermocouple is held for 2 seconds within the flame and the procedure is repeated three times. A microscope is used to confirm that a uniform coating of $3 \pm 0.5 \mu\text{m}$ is applied.

3.3 Experimental procedures

For detailed experimental procedures please refer to the appendix.

3.4 Numerical Techniques

The flame simulation is performed using FLUENT and the results are included in the appendix.

3.5 Sample Preparation

All foils investigated are cut into 1cm x 2cm pieces and placed above the burner. The foil can be placed parallel to the burner, where the flow impinges on the substrate, or perpendicular to the burner, where the flow runs parallel to the substrate. For CNT growth cases in Chapter 6, the substrate is cleaned in ethanol using ultra-sonication. In all other cases no prior substrate preparation is performed. [Table 3.1](#) provides a list of foils investigated.

Name	Thickness	Company	Part #
Copper Foil	0.025mm	Alfa Aesar	13382
Nickel Foil	0.025mm	Alfa Aesar	12722
Stainless Steel 304 Foil	0.025mm	Alfa Aesar	41580
Iron Foil	0.025mm	Alfa Aesar	44687
Cobalt Foil	0.025mm	Alfa Aesar	40183
Nickel Copper Foil	0.51mm	Alfa Aesar	45148
Nickel Copper Foil	0.025mm	Goodfellow	430-916-69
Nickel Foil 201	0.050mm	Arnold Magnetics	
Inconel Foil 600	0.050mm	Arnold Magnetics	

Table 3.1 List of substrates investigated.

3.6 Characterization techniques

Table 3.2 summarizes the list of equipment used to characterize the growth of graphene and CNTs.

Technique	Equipment
Raman spectroscopy	Renishaw 1000, laser excitation 514.5 nm
Atomic force microscopy	Digital Instruments Nanoscope II
X-ray photoelectron spectroscopy	Thermo Scientific K-Alpha
Transmission electron microscopy	JEOL 2010F & TOPCON 002B
Scanning electron microscopy	Zeiss Sigma 8100

Table 3.2 List of characterization techniques.

3.6.1 Raman spectroscopy

Raman spectroscopy is used to investigate the vibrational and rotational modes within a crystal or molecule. The technique involves the use of an incident electromagnetic (em) radiation, which alters the electronic cloud of the chemically bonded structure by storing energy. If the stored energy is re-radiated at the same frequency as the incident (em), then it is referred to as Rayleigh scattering. When the stored energy is partially absorbed within the molecule, a resulting photon of lower energy is generated, which is referred to as Stokes scattering. To the contrary, when the molecule loses energy, a photon of higher energy is generated that is referred to as Anti-Stokes scattering. The Stokes and Anti-Stokes occurrence are called Raman lines and is based on the vibrational or rotational frequency of the structure (see Fig. 3.4).

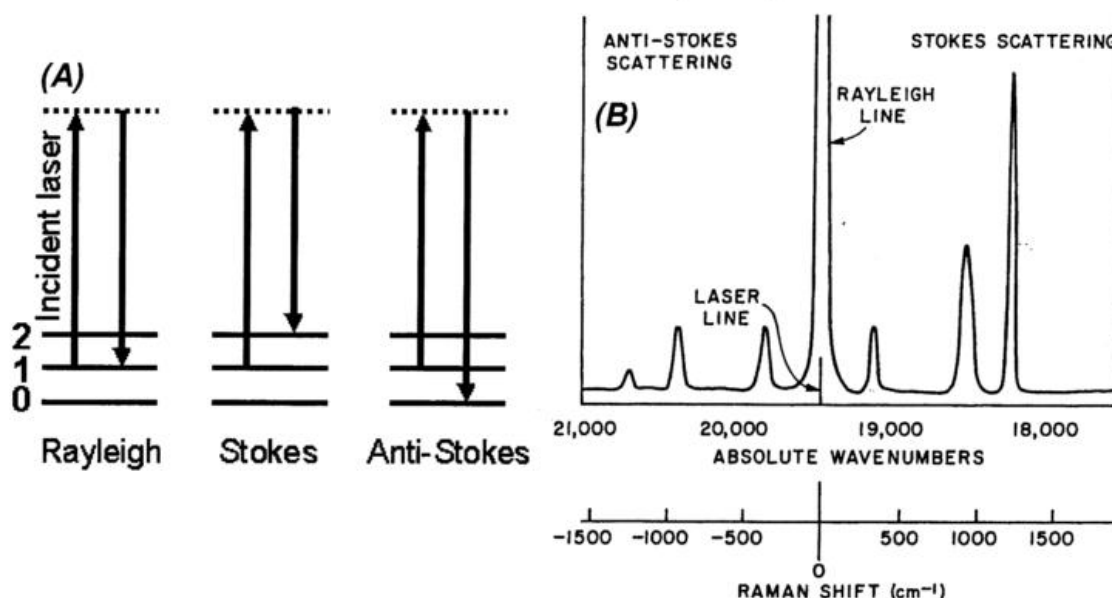


Figure 3.4. a) Illustration of energy transitions leading to Rayleigh, stokes and anti-stokes spectra. b) Schematic Raman scattering spectrum showing Rayleigh line, Stokes and Anti- Stokes Raman scattering (reproduced with caption from [1,2]).

Raman spectroscopy is a very powerful and important technique for the characterization of graphitic materials. It has been extensively used to characterize amorphous carbon, graphite, carbon fibers, glassy carbon, fullerenes, carbon nanotubes, and graphene [3]. [Figure 3.8](#) illustrates the Raman spectrum for common sp^2 bonded carbon materials. Four features of the Raman spectra are used to distinguish between different sp^2 carbon forms, which include the D, G, G' (or 2D), and Raman breathing mode (RBM).

The G band is related to the bond stretching of sp^2 bonded carbon atoms. Any modification to the flat structure of graphene, such as an external forcer or the interaction by placing another graphene layer, can cause a shift in the G peak. CNTs due to their curved structure result in the occurrence of multiple peaks within the G band, while a single strong peak is typically observed for graphene. Additionally, for CNTs the curvature dependence is related to the diameter, which can be probed using the G peak [3].

Similarly all sp^2 carbon materials have a strong peak in the range of 2500 – 2800 cm^{-1} called the G' (or 2D) peak. This peak is caused by the second-order zone boundary phonons and is used to determine the number of layers of graphene. For graphite, this peak (using a 514nm laser) is at $\sim 2727cm^{-1}$, and for a single layer of graphene, it shifts to $2660cm^{-1}$ [4]. A 2D peak between these numbers can be used to determine the number of graphene layers ([Fig. 3.6](#)). The location of the G' peak is dependent on the excitation laser and the results comparing the peaks using a 514 and 633nm laser is shown in [Fig. 3.6](#). The G' peak is also used for probing the electronic structure of SWNTs [3].

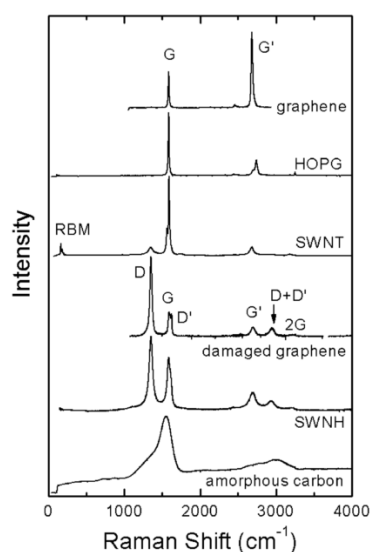


Figure 3.5 Raman spectra of the different types of sp^2 carbon forms (reproduced with caption from [3]).

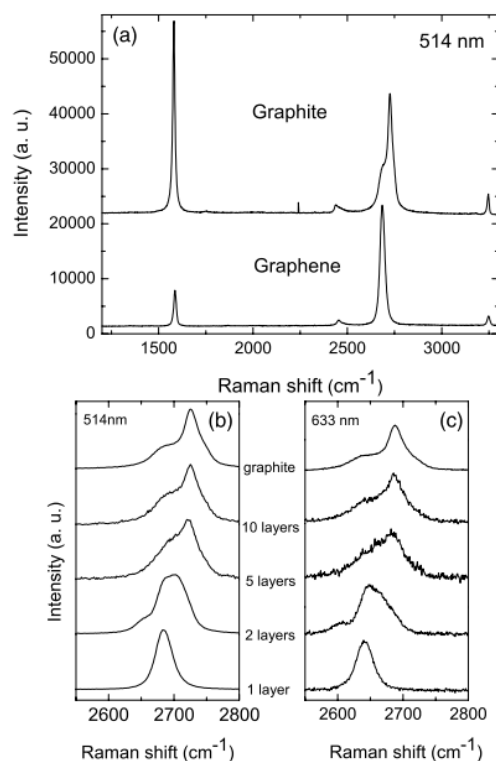


Figure 3.6 (a) Comparison of Raman spectra at 514 nm for bulk graphite and graphene. (b) Evolution of the spectra at 514 nm with the number of layers. (c) Evolution of the Raman spectra at 633 nm with the number of layers (reproduced with caption from [4]).

The D peak is due to the first-order zone boundary phonons and is used to determine the disorder present in the graphene. For pristine single-layer graphene, there should be no D peak present. However, as the number of graphene layers increases, a D peak is normally encountered. The ratio between the D and G peak is used as a metric to measure the disorder present in the graphene, which develops from domain boundaries, wrinkles, edges, impurities, and other phenomena.

The radial breathing mode (RBM) is important when characterizing SWNTs, where it can determine the diameter and optical transition energy for a given tube. It can also be used to understand the tube to tube interaction within MWNTs [3]. Overall Raman spectroscopy is a very powerful and important tool when characterizing graphene and CNTs.

3.6.2 X-ray photoelectron spectroscopy (XPS)

XPS is a technique that determines the elemental composition, empirical formula, chemical state and electronic state of the elements that occur within a material. An X-ray beam is used to irradiate the material and the number of electrons along with the kinetic energy is measured. XPS is performed under ultra-high vacuum conditions and is a surface technique with a penetration depth of 1 to 10nm. [Figure 3.7](#) summarizes the basic components of an XPS system.

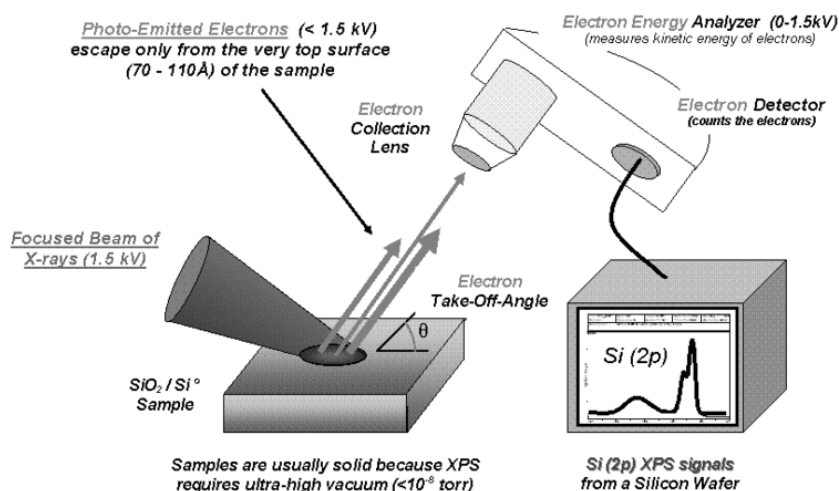


Figure 3.7 Basic component of an XPS system (reproduced from [5]).

XPS can be used to determine sp^2 bonded carbon materials from other carbon structures (Fig. 3.8). For graphite, CNTs, and graphene a single peak at ~ 284.5 eV is typically observed. Additionally the C1s peak is used to determine the presence of oxygen incorporation (C-O) within the graphene structure.

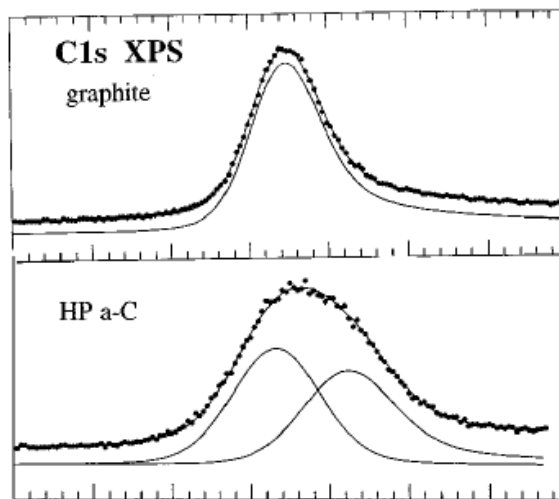


Figure 3.8 Comparison between the C 1s XPS spectra of graphite and those of the amorphous carbon films (reproduced with caption from [6]).

3.6.3 Atomic Force Microscopy (AFM)

AFM consists of a cantilever with a sharp tip that is used to scan the surface of a substrate. It can be used to determine the surface morphology and the thickness of a film structure. For few-layer graphene it can be used to estimate the number of layers (Fig 3.9), where a single layer of graphene has a thickness of 0.7nm.

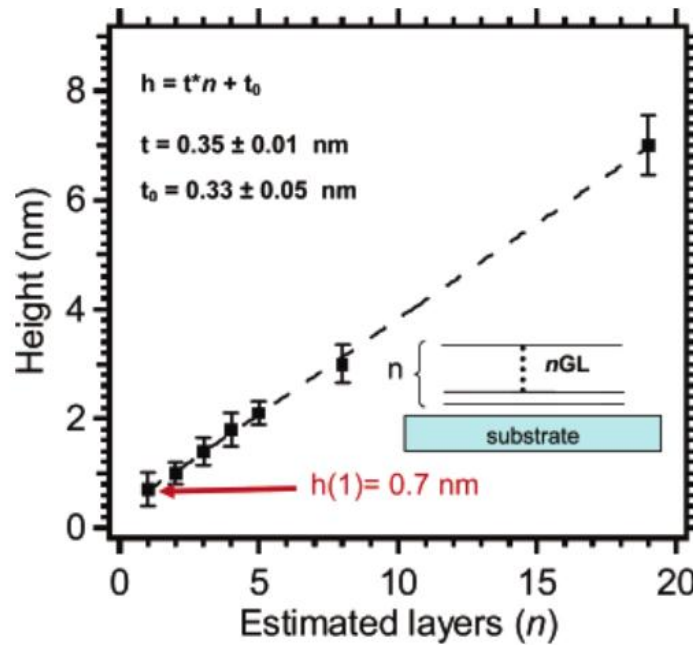


Figure 3.9 Correlation between the AFM height and number of graphene layers (reproduced with caption from [7]).

3.6.4 Field-Emission Scanning Electron Microscopy (FESEM)

FESEM is used for imaging a sample by scanning it with a beam of electrons. The interaction between the electrons and the material reveal the surface topography. It is commonly used to determine the morphology of the CNTs and graphene films. Variation in the thickness of a graphene film can be observed using FESEM.

3.6.5 Transmission electron microscopy (TEM)

TEM is where a beam of electrons is transmitted through an ultra-thin sample (see [Fig. 3.10](#)). This technique can be used for imaging or obtaining a diffraction pattern. For graphene, high resolution transmission electron microscopy (HRTEM) can be used to depict the hexagonal atomic structure. Selected area electron diffraction (SAED) can be used to determine the crystallinity of the carbon nanomaterial.

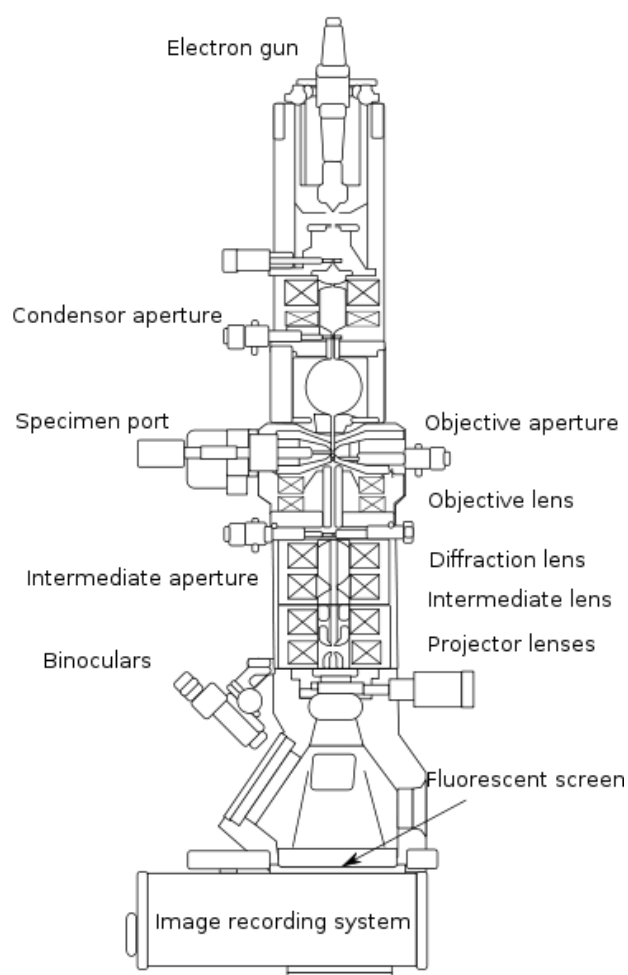


Figure 3.10 Schematic diagram of a transmission electron microscope [8].

3.7 References

- [1] Height MJ. MIT Flame Synthesis of Carbon Nanotubes and Metallic Nanomaterials Thesis. 2002.
- [2] Brundle CR, Evans C, Wilson S. Encyclopedia of materials characterization: surfaces, interfaces, thin films : Boston : Butterworth-Heinemann ; 1992.
- [3] Dresselhaus MS, Jorio A, Hofmann M, Dresselhaus G, Saito R. Perspectives on Carbon Nanotubes and Graphene Raman Spectroscopy. Nano Lett 2010;10:751-8.
- [4] Ferrari AC, Meyer JC, Scardaci V, Casiraghi C, Lazzeri M, Mauri F et al. Raman Spectrum of Graphene and Graphene Layers. Phys Rev Lett 2006;97:187401.
- [5] http://en.wikipedia.org/wiki/X-ray_photoelectron_spectroscopy.
- [6] D  az J, Paolicelli G, Ferrer S, Comin F. Separation of the sp^3 and sp^2 components in the C1s photoemission spectra of amorphous carbon films. Phys Rev B 1996;54:8064-9.
- [7] Gupta A, Chen G, Joshi P, Tadigadapa S, Eklund. Raman Scattering from High-Frequency Phonons in Supported n-Graphene Layer Films. Nano Lett 2006;6:2667-73.
- [8] http://en.wikipedia.org/wiki/Transmission_electron_microscopy.

Chapter 4

4. Structure, Property, and Thickness of Graphene Films Prepared Using Open Atmosphere Flame Synthesis

4.1 Introduction

Both single-layer and few-layer graphene possess unique properties that afford a wide range of applications, including high frequency transistors [1] and transparent electrodes [2]. Ultimately, the future of graphene-based devices lies in developing production methods that are highly scalable, reliable, efficient, and economical. Mechanical exfoliation enabled the isolation of graphene and the discovery of its extraordinary electronic properties; however, this method is limited to producing graphene flakes due to its lack of scalability. Sublimation of Si from single-crystal silicon carbide (SiC) offers the advantage of direct synthesis of graphene on insulating surfaces [3,4]. Nevertheless, this method requires very-high temperatures, which has associated difficulties, and is presently constrained by high SiC wafer cost. Chemical vapor deposition (CVD) of graphene on transition metals such as nickel (Ni) [5,6] and copper (Cu) [7,8] shows the most potential for large-volume production of graphene. While still in its early stages, CVD-grown graphene has already demonstrated excellent device characteristics [9], including electron mobility of $7,350 \text{ cm}^2\text{V}^{-1}\text{s}^{-1}$ [10]. Nevertheless, growth of graphene over large areas remains challenging, due to the confinement necessary to operate at reduced pressures or suitable environments.

Flame synthesis has a demonstrated history of scalability and offers the potential for high-volume continuous production at reduced costs [11]. In utilizing globally-rich

combustion, a portion of the hydrocarbon gas provides the requisite elevated temperatures, with the remaining fuel serving as the hydrocarbon reagent for carbon-based nanostructure growth, thereby constituting an efficient source of energy and hydrocarbon reactant. This aspect can be especially advantageous as the operating costs for producing advanced materials, particularly in the semiconductor industry, end up far exceeding the initial capital equipment costs. Flame synthesis has been used successfully to grow various oxide nanostructures [12,13], single-wall [14] and multi-wall [15] carbon nanotubes (CNTs), sheet-like carbon particles [16], and amorphous carbon thin-films [17]. Recently, few-layer graphene has been synthesized with flames using alcohol as fuel on Ni substrates [18]. The process utilized two different burners, with the substrate situated within the interior region of the flame structure itself. Although the viability of flame synthesis to grow graphene was demonstrated, the process resulted in the formation of amorphous carbon impurities along with the graphene. Moreover, the configuration may not readily scalable for large-area graphene production. Flame synthesis of graphene on Cu has yet to be reported.

The synthesis configuration employed in this work is based on a multiple inverse-diffusion (non-premixed) flame burner, where the post-flame species are directed at a substrate to grow graphene; see [Fig. 4.1](#). Each of the tiny diffusion flames is run in the inverse mode (“under-ventilated”), where for each flame, the oxidizer is in the center and fuel (e.g. methane) surrounds it. The net effect is that post-flame gases are largely comprised of pyrolysis species that have not passed through the oxidation zone. In fact, the reaction zone serves as a “getterer,” such that the oxygen mole fraction can be reduced to $\sim 10^{-8}$ in the post-flame gases. Carbon formation processes are effectively

separated from oxidation processes in inverse diffusion flames, which also tend to soot less than normal diffusion flames [19]. No soot is observed in our multiple-inverse diffusion flame setup, for the conditions examined. Moreover, the hydrocarbon species (rich in C_n and CO), which serve as reagents for graphene growth, are generated in much greater quantities than that achievable in stable, self-sustained premixed flames. By using diffusion flames (burning stoichiometrically in the reaction zone), flame speed, flashback, and cellular instabilities related to premixed flames are avoided. Operation of a multi-element non-premixed flame burner has no scaling problems by allowing for stability at all burner diameters, where the issuing flow velocity can be independent of the burner diameter. Moreover, since many small diffusion flames are utilized, overall radially-flat profiles of temperature and chemical species are established downstream of the burner, ensuring uniform growth. Confinement in an inert environment or shielding with an inert co-flow or tube prevents an encompassing diffusion flame from developing. Finally, this flame synthesis configuration is well suited for carbon-based nanomaterial synthesis in open-atmosphere environments, affording large-area growth (e.g. by translating the burner and rasterizing) at high rates.

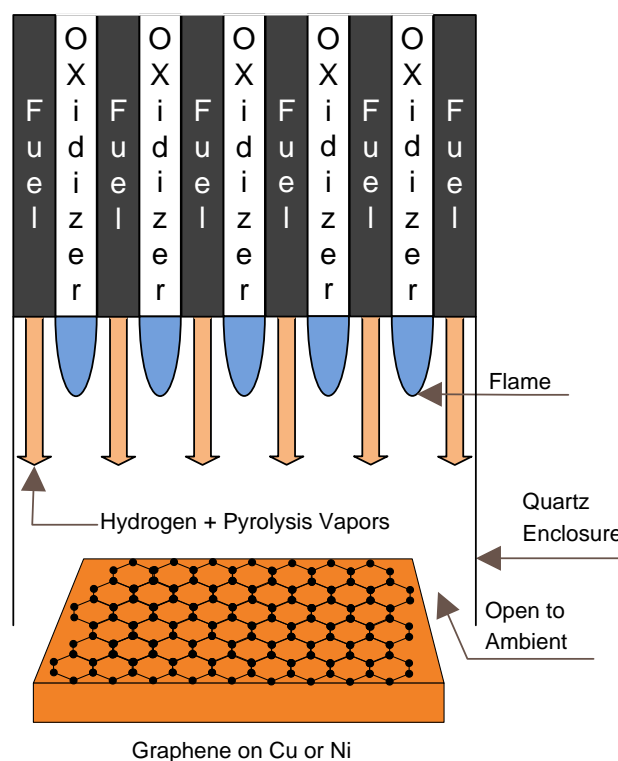


Figure 4.1 Multiple inverse-diffusion flames provide hydrogen and carbon-rich species suitable for growth of graphene and other carbon nanomaterials.

4.2 Experiment

Few-layer graphene (FLG) films are grown on 25 μm thick Cu and Ni foils (Alfa Aesar), placed downstream of our novel burner. A quartz cylinder encompasses the region of the multiple flames and substrate, preventing oxidizer permeation from the ambient and directing optimal gas-phase conditions (i.e. species and temperature) to the substrate. Note that the setup is open to atmospheric conditions. Prior to FLG film synthesis, the metal substrates are reduced in a hydrogen environment to remove any oxide layers. This treatment is accomplished using the same multiple inverse-diffusion flame burner running only hydrogen as fuel at a globally-rich equivalence ratio for 10 minutes. For

FLG synthesis, CH_4 is introduced into the fuel (with a global equivalence ratio of ~ 3) for 5 and 10 min, for Ni and Cu substrates, respectively. A silica-coated 125 μm Pt/Pt-10%Rh thermocouple (S-type) measures the substrate temperature to be $\sim 950^\circ\text{C}$. The experiment is finalized by turning off the oxygen, which extinguishes the flame, while fuel and inert gases continue to flow, cooling the substrate to room temperature.

The films grown on Cu are transferred onto SiO_2/Si substrates for electrical and Raman analysis. The transfer is done by first spin-coating poly-methyl methacrylate (PMMA) on the graphene covering the Cu substrate. Since the thermofluid mechanics give rise to FLG being grown on both sides of the substrate, oxygen plasma is used to remove the graphene film from one side. The PMMA-coated graphene on Cu substrate is then immersed in a ferric chloride (FeCl_3) solution (23%wt) to etch away the copper. The free-floating PMMA coated graphene is then carefully placed on the SiO_2/Si substrate, and the PMMA is removed in hot acetone. The final sample is rinsed with isopropanol, and dried with N_2 .

The FLG is characterized using Raman spectroscopy (Renishaw 1000, laser excitation 514.5 nm), atomic force microscopy (AFM, Digital Instruments Nanoscope II), X-ray photoelectron spectroscopy (XPS, Thermo Scientific K-Alpha), and transmission electron microscopy (TEM, JEOL 2010F). For TEM sample preparation, the metal substrate is etched away, and the graphene film is placed in ethanol. The obtained solution is ultrasonicated for 5min to form a homogenous suspension, and a drop is placed on a lacey TEM grid.

4.3 Results and Discussion

Synthesis of FLG has been demonstrated on a number of transition metals. Due to their low cost and acceptability in the semiconductor industry, copper and nickel are promising substrates for the growth of graphene. While a number of parameters such as pressure, temperature, and crystal structure influence the growth of graphene, the difference in carbon solubility of metals such as Cu and Ni results in distinctive growth mechanisms [20]. From the binary phase diagram of Ni and C [21], at temperatures above 800°C, Ni and C form a metastable solid phase; upon cooling, the carbon diffuses out of the Ni to form graphene/graphite. Due to this growth mechanism on Ni, the number of graphene layers across the substrate remains difficult to control. In contrast, graphene formation on Cu occurs only on the surface due to the extremely-low solubility of carbon in Cu. Consequently, once the substrate is covered by graphene, the Cu surface is no longer accessible; and deposition of additional layers does not occur [7,20]. Hence, Cu has proven to be an excellent substrate for the growth of monolayered graphene; however, growing multiple layers has been found to be challenging.

4.3.1 Flame Synthesis of FLG on Cu

A photograph of a flame-synthesized FLG film that has been subsequently transferred onto a 1cm × 1cm quartz substrate is shown in [Fig. 4.2a](#). In [Fig. 4.2b](#), an optical image shows a graphene flake along with the corresponding atomic force microscopy (AFM) image. The thickness of the graphene films on Cu is found typically to be on the order of 4nm from AFM height profiles, suggesting that the film consists of 8 to 10 monolayers of graphene.

Raman spectroscopy enables the identification of single to few-layer graphene [22], along with its quality. Typical Raman spectrum of FLG after transfer onto SiO₂/Si is shown in Fig. 4.2(c). Three peaks are noticeably present in the spectrum: (i) the D peak at 1351 cm⁻¹, which is due to the first-order zone boundary phonons and is used to determine the disorder present in the graphene; (ii) the G peak at 1580 cm⁻¹, which is related to the bond stretching of sp² bonded carbon atoms; and (iii) the 2D peak at ~2700 cm⁻¹, which is caused by the second-order zone boundary phonons. The ratio between the intensities of the G peak (I_G) and the 2D peak (I_{2D}) provides an estimate of the number of layers [6,23], where, from Fig. 4.2(d), the values are found to range from 1.3 to 1.7. For mono and bi-layer graphene, this ratio is less than 1. If more than 2 layers are present, ratios ranging from 1.3 to 2.4 have been reported for FLG. Reina et al. [23] reported I_G/I_{2d} ratio of 1.3 for 3 layers of graphene on Ni; and Robertson et al. [24] reported values of 1.8 to 2.4 for 5 to 10 layers of graphene on Cu. The full-width and half-maximum (FWHM) of our 2D peak is ~75 cm⁻¹, which is consistent with FLG grown at atmospheric pressure [8]. The Raman data should be used in conjunction with other characterization and verification techniques to corroborate the properties of FLG. Transmittance can be used to assess the number of graphene layers, where the opacity of monolayer graphene is estimated to be 2.3% [25]. From Fig. 4.3a, the transmittance of our FLG films at 550nm is 86%, which correlates to ~6 layers. Combining our results from Raman, AFM, and transmittance, we estimate that 5 to 8 layers of graphene are grown uniformly across the Cu substrate using our flame-synthesis technique.

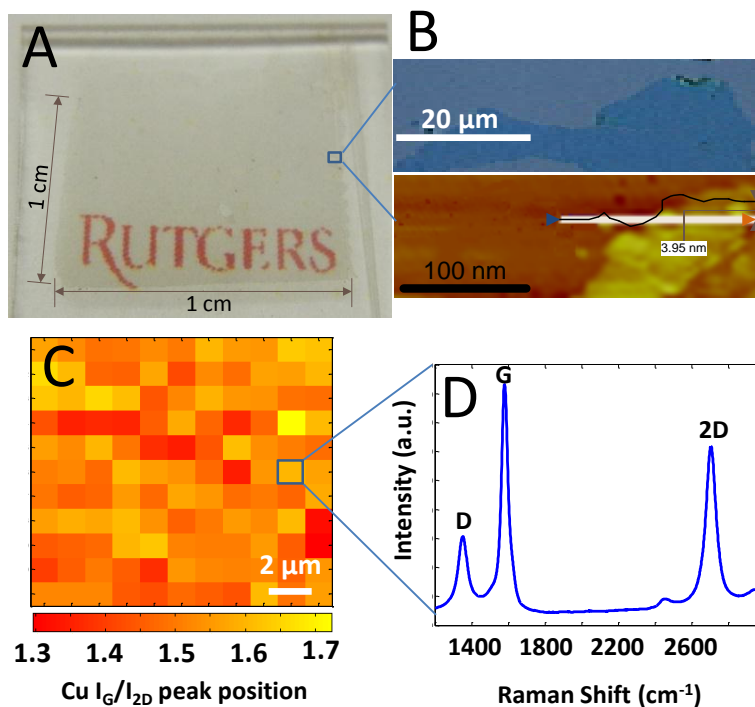


Figure 4.2 Few-layer graphene (FLG) film grown by flame synthesis on Cu. (a) Photograph of a 1 cm x 1 cm film transferred onto quartz. (b) Optical microscope image of the FLG transferred onto a Si substrate with a 300 nm oxide layer and the corresponding AFM image and height profile of the FLG transferred on SiO₂/Si substrate. (c) Two-dimensional mapping of the Raman I_G/I_{2D} over a 12 μm x 12 μm area. (d) Raman spectrum of the FLG on SiO₂/Si.

The I_D/I_G ratio observed in our sample is around ~ 0.35 , which is comparable to measurements of FLG grown using other methods [8]. The measured disorder in our FLG likely arises from the sheets being composed of sub-micron domains. Using the four probe method, the sheet resistance of the FLG is calculated to be 40 kΩ/sq at 86% transmittance value, which is considerably higher than CVD-grown graphene. Similarly, the high sheet resistance may be attributed to the small domain size of the graphene. In CVD growth, the characteristic domain size of graphene has been increased by lowering the global flux of methane [26]. However, the fundamental mechanism for this trend is

not clear, as there are many effects intertwined; and additional parameter dependencies need to be explored to isolate the controlling mechanism dictating domain size. We are currently investigating the effect of methane flux, as well as other parameters, on enlarging domain size for flame-synthesized graphene on Cu.

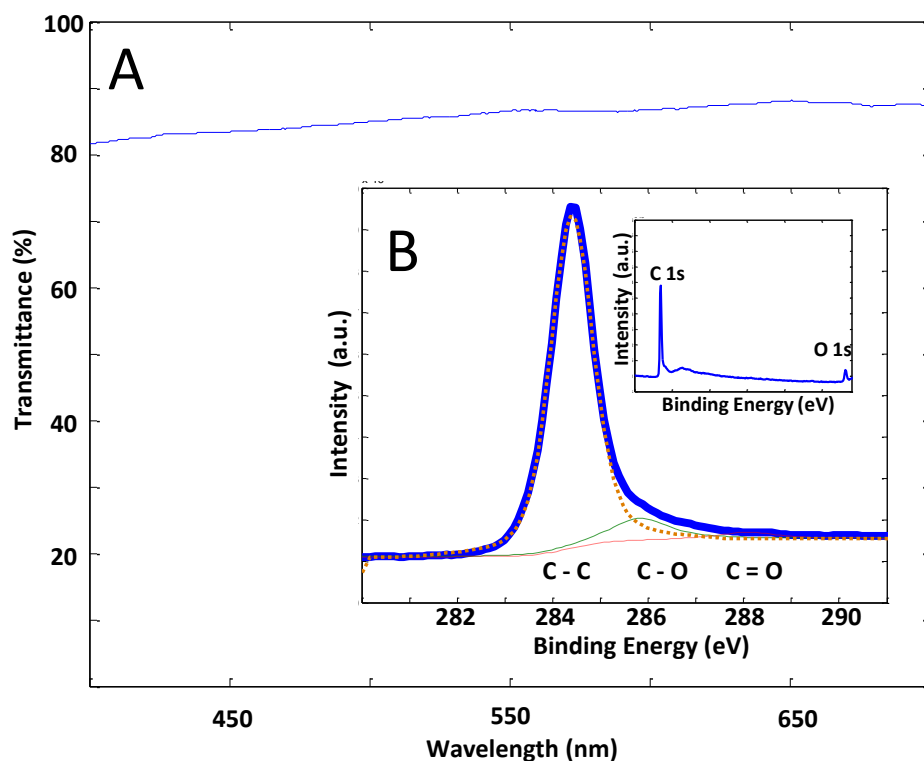


Figure 4.3 (a) UV-vis spectrum of the FLG transferred onto a quartz substrate. (b) XPS C 1s spectrum of the FLG shows that the oxygen contamination is minimal and is comparable to CVD grown graphene. The inset shows the XPS spectra of the film.

A product of hydrogen and hydrocarbon combustion with oxygen is H_2O , which at high temperatures can result in oxygen doping of graphene. However, with abundant H_2 present in the post-flame species, and at relatively “low” growth temperatures ($\sim 950^\circ C$), such oxidation reactions are minimized. The X-ray photoelectron spectroscopy (XPS) spectrum of the C 1s peak, where the main peak at 284.4 eV indicates

that most of the atoms are in the sp^2 C state, is shown in Fig. 4.3b. Less than 10% of oxygen incorporation (e.g. CO) is visible from the XPS figure. Surprisingly, the amount of oxygen-bonded species in our open-ambient flame synthesis process is actually lower than that for CVD-grown graphene under near vacuum conditions [9]. Consequently, the conditions for our flame synthesis, where H_2O oxidation is minimized, O_2 is “getterred” in the reaction zone, and open-atmosphere processing is afforded, are advantageous for scaled growth of graphene over large areas (e.g. over existing structures). Note that the O 1s peak, as seen in the inset of Fig. 4.3b, is due to oxygen or water absorbed on the surface and is even present in pristine graphene [27]. The oxygen content between graphene layers needs to be further investigated.

The effects of $CH_4:H_2$ ratio and temperature are examined in the growth of FLG on Cu. For the standard case, the $CH_4:H_2$ ratio is kept at 1:10, and similar results are observed when this ratio is varied from 1:5 to 1:20. However, when the ratio is below 1:40, no growth of FLG is observed on the substrate. This result is contrary to that reported using atmospheric-pressure CVD [8], where at lower $CH_4:H_2$ ratios, monolayer graphene is synthesized. In flame synthesis, temperature is a critical factor in the growth of uniform FLG. At lower gas-phase temperatures, the typical Raman spectrum features resemble those of nanocrystalline graphite [28], where a much higher D-peak exists and the intensity ratio between the G peak and 2D peak increases, as shown in Fig. 4.4. Upon further reducing the gas-phase temperature, the 2D peak disappears. However, a G peak is still observed, indicating the presence of activated carbon-based materials on the copper [29]. The reason for different carbon-based growth on Cu is perhaps due to the presence of other gaseous carbonaceous species, such as CO and C_n , in the post-flame

environment. These species can readily decompose at lower temperatures to form carbon materials that are stable at lower temperatures. In another work [17] that attempts to grow graphene on copper using flames, a thin carbon film is synthesized with large amounts of sp^3 bonding. This characteristic of the thin film was attributed to the low deposition temperatures of 550°C to 700°C .

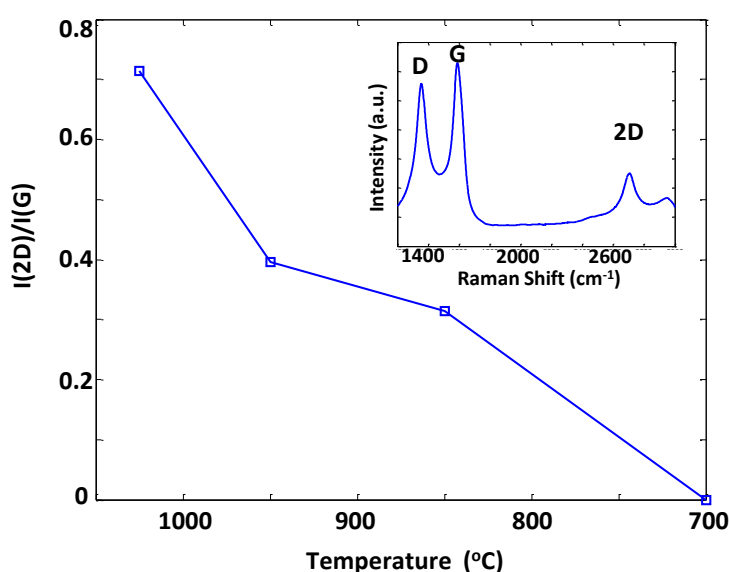


Figure 4.4 Analysis of the influence of temperature on the growth of FLG on Cu, showing variation in Raman I_{2D}/I_G as a function of gas phase temperature. The inset shows atypical Raman spectrum observed at lower temperatures.

4.3.2 Flame Synthesis of FLG on Ni

A typical Raman spectrum of FLG grown on $25\mu\text{m}$ thick Ni foil is shown in Fig. 4.5a.

The number of layers of graphene on nickel is estimated based on the location of the 2D peak [6]. With the 2D peak at 2720 cm^{-1} , this shift corresponds with 5 to 10 layers of graphene. The G peak is at 1583 cm^{-1} , and a typical I_D/I_G ratio is 0.1, which is lower than that for the FLG grown on Cu. This result can be attributed to the different growth

mechanism of graphene on Ni compared with that on Cu. Ni has higher carbon solubility, so the growth of graphene occurs due to carbon segregation or precipitation. This growth mechanism on Ni should be unaffected by the high carbon flux encountered in the flame. However, in the case of Cu, high carbon flux may lead to smaller graphene domain size, and hence more measured disorder. A HRTEM image and the corresponding diffraction pattern are shown in Fig. 4.5b. The hexagonal symmetry of multiple graphene layers can be inferred from the diffraction pattern, although specific stacking order of the layers requires additional analysis. A magnified image of the well-ordered graphitic lattice is shown in the inset of Fig. 4.5b.

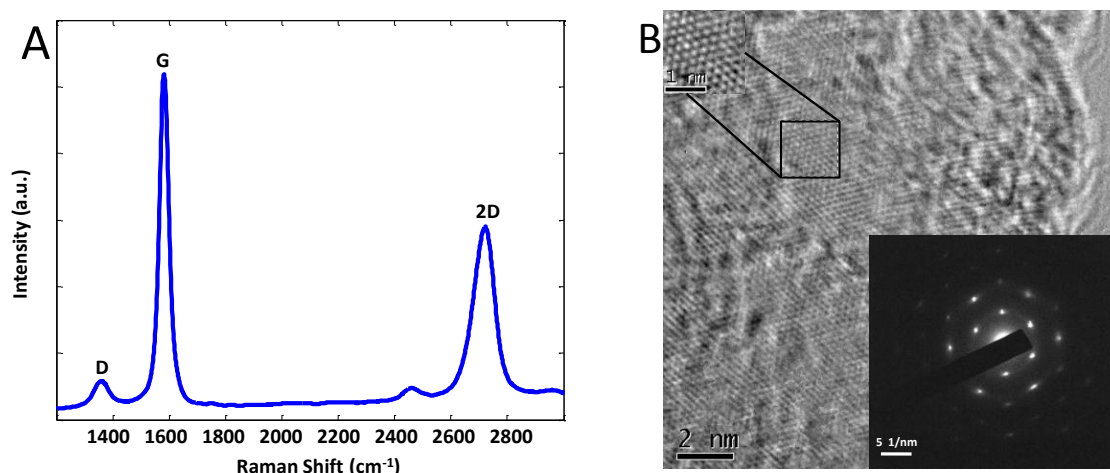


Figure 4.5 Few-layer graphene film grown by flame synthesis on Ni. a) Raman spectrum of the FLG on Ni. b) HRTEM image of the FLG. The bottom right inset shows the electron diffraction pattern of the graphene sheet, illustrating the well-defined crystalline structure. The top left inset shows resolution magnified image of the graphitic lattice.

The XPS of the graphene on Ni is shown in Fig. 4.6 and the main C 1s peak is at 284.5 eV, which indicates most of the atoms are in the sp² C state [30]. Similar to Cu, a

low oxygen concentration is observed for the growth of graphene on Ni. Hence it is proposed here that the abundance of H_2 in the post-flame species of the multiple inverse-diffusion flame, limits the oxidation of the graphene film.

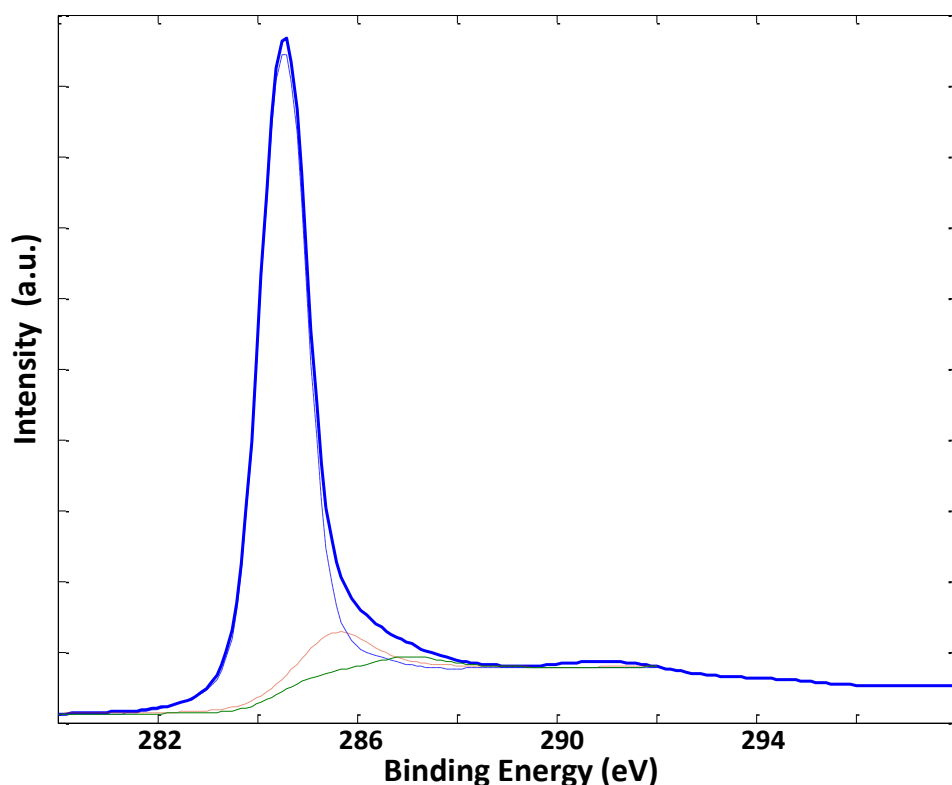


Figure 4.6. XPS C 1s spectrum of the FLG on Ni.

Graphene growth on nickel depends on a number of parameters, such as metal substrate thickness, hydrocarbon to hydrogen ratio, growth time, and temperature. The dependence of graphene growth on gas-phase temperature and methane concentration is illustrated in Fig. 4.7. The gas-phase temperature directly affects the gas-phase chemistry as well as the rate of hydrocarbon decomposition on the Ni surface, which further affects the diffusion rate of carbon atoms into Ni [31]. Hence, at lower gas-phase temperatures,

fewer carbon atoms diffuse into Ni, leading to the growth of fewer layers of graphene upon cooling. This effect is evident from optical microscopy of the as-synthesized graphene on Ni. At lower temperatures (i.e. 850°C), Fig. 4.7a shows lighter regions corresponding to FLG; and the color contrast demonstrates that the growth of FLG on Ni is not uniform. With increased temperature (i.e. 950°C), Fig. 4.7b shows that the Ni foil becomes uniformly dark, indicating the presence of more than 10 layers of graphene. The dependence of graphene growth on the ratio of methane to hydrogen is shown in Fig. 4.7c. When this ratio is lowered to 1:20, the Raman position of the 2D peak ($\sim 2700\text{ cm}^{-1}$) indicates that fewer than 5 layers of graphene are grown. Interestingly, such growth is similar to the 850°C temperature growth illustrated in Fig. 4.7a, where the growth is non-uniform across the substrate.

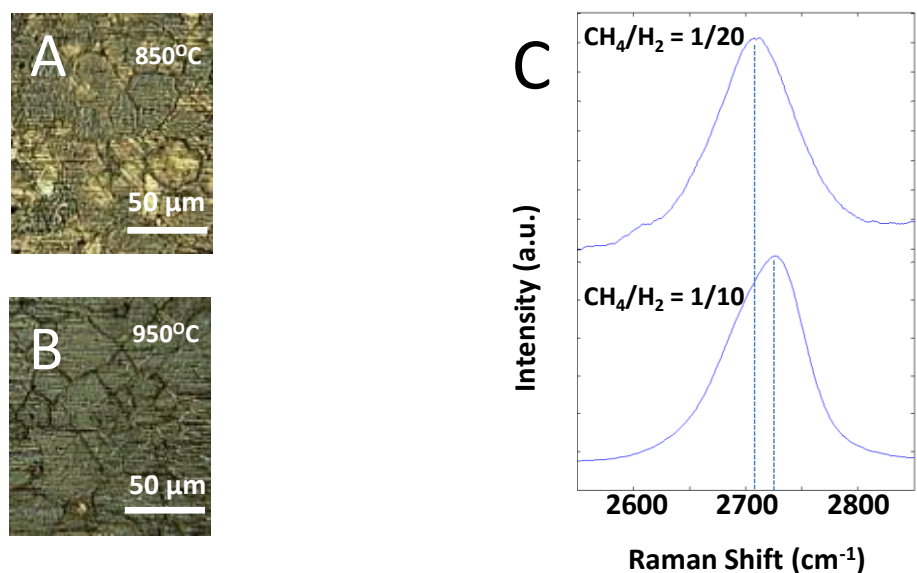


Figure 4.7 Investigation of the temperature and methane concentration on the growth of FLG on Ni. a) Temperature = 850°C, CH₄:H₂ = 1:10. b) Temperature = 950°C, CH₄:H₂ = 1:10. c) Raman spectra showing the 2D peak at a constant temperature of 950°C.

For the gas-phase synthesis conditions examined, the growth of FLG on Ni results in lower disorder, as assessed by Raman, when compared to the growth on Cu. However, the growth is less uniform and comprises more layers (>10), due to the different growth mechanism of graphene on Ni, compared to growth on Cu. The Raman mappings of FLG grown on Cu and Ni, respectively, at a $\text{CH}_4:\text{H}_2$ ratio of 1:10, are compared in Fig. 4.8. For Cu, methane is introduced for 10 minutes at a temperature of 950°C ; while for Ni, methane is introduced for 5 minutes at a temperature of 850°C . In Fig. 4.8a, for Cu, the 2D peak is always at or below 2700 cm^{-1} , which is consistent with FLG. On the other hand, in Fig. 4.8b, for Ni, the 2D peak reaches a value of 2727 cm^{-1} , indicating the presence of more than 10 layers. As such, the growth of graphene on Cu is self-limiting to few-layers for our flame synthesis system at atmospheric conditions.

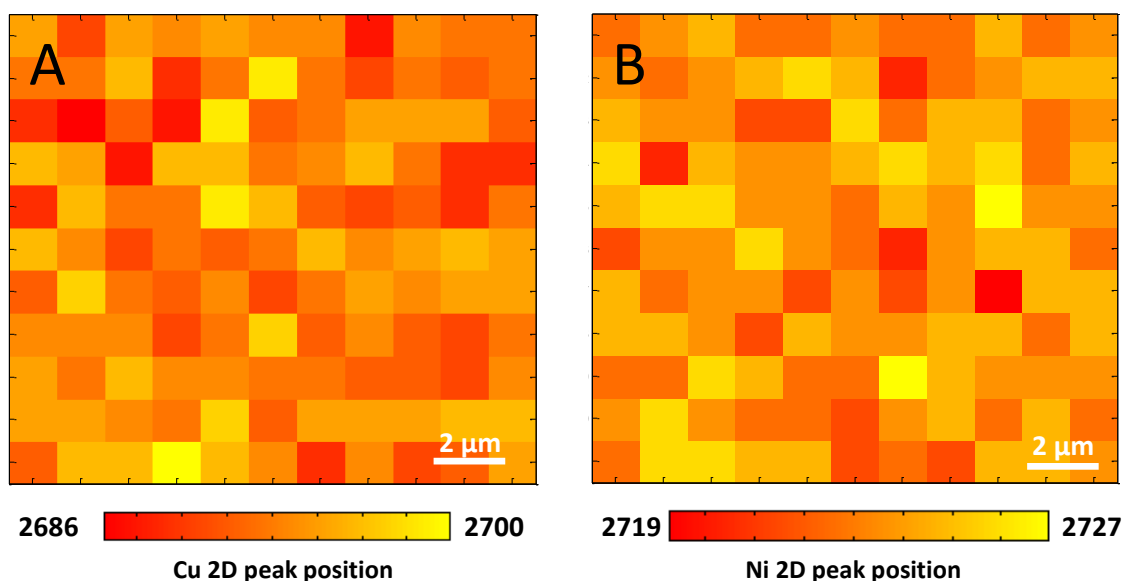


Figure 4.8 Raman mappings of the 2D peak over a $12\text{ }\mu\text{m} \times 12\text{ }\mu\text{m}$ region at a constant $\text{CH}_4:\text{H}_2$ ratio of 1:10. a) Raman mapping for Cu, illustrating that the growth of graphene is self-limiting to a few layers. b) Raman mapping for Ni, showing regions that correlate to more than 10 layers.

4.4 Concluding Remarks

Flame synthesis utilizing a multiple-inverse diffusion flame burner is demonstrated in this work to be well-suited for processing carbon-based nanostructures. Under very rich fuel conditions, the configuration generates specific hydrocarbon species that can form graphene on a heated metal substrate. On Cu, 5 to 8 layers of graphene are grown uniformly across the substrate. Due to a different growth mechanism, Ni offers lower graphene disorder, but at a cost of more layers created. The configuration allows for detailed probing of the local gas-phase temperature and relevant chemical species such that the fundamental growth mechanisms of graphene on various substrates can be identified. Finally, the method is scalable and capable of continuous operation in an open-ambient environment, presenting the possibility of large-area processing.

4.5 References

- [1] Wu Y, Lin Y, Bol AA, Jenkins KA, Xia F, Farmer DB et al. High-frequency, scaled graphene transistors on diamond-like carbon. *Nature* 2011;472:74-8.
- [2] Bonaccorso F, Sun Z, Hasan T, Ferrari AC. Graphene photonics and optoelectronics. *Nat Photon* 2010;4:611-22.
- [3] Aristov VY, Urbanik G, Kummer K, Vyalikh DV, Molodtsova OV, Preobrajenski AB et al. Graphene Synthesis on Cubic SiC/Si Wafers. Perspectives for Mass Production of Graphene-Based Electronic Devices. *Nano Letters* 2010; 2010;10:992-5.
- [4] Emtsev KV, Bostwick A, Horn K, Jobst J, Kellogg GL, Ley L et al. Towards wafer-size graphene layers by atmospheric pressure graphitization of silicon carbide. *Nat Mater* 2009;8:203-7.
- [5] Obraztsov AN, Obraztsova EA, Tyurnina AV, Zolotukhin AA. Chemical vapor deposition of thin graphite films of nanometer thickness. *Carbon* 2007;45:2017-21.

- [6] Chae SJ, GÃ¼neÅŸ F, Kim KK, Kim ES, Han GH, Kim SM et al. Synthesis of Large-Area Graphene Layers on Poly-Nickel Substrate by Chemical Vapor Deposition: Wrinkle Formation. *Adv Mater* 2009;21:2328-33.
- [7] Li X, Cai W, An J, Kim S, Nah J, Yang D et al. Large-Area Synthesis of High-Quality and Uniform Graphene Films on Copper Foils. *Science* 2009;324:1312-4.
- [8] Bhaviripudi S, Jia X, Dresselhaus MS, Kong J. Role of Kinetic Factors in Chemical Vapor Deposition Synthesis of Uniform Large Area Graphene Using Copper Catalyst. *Nano Letters* 2010; 2010;10:4128-33.
- [9] Bae S, Kim H, Lee Y, Xu X, Park J, Zheng Y et al. Roll-to-roll production of 30-inch graphene films for transparent electrodes. *Nat Nano* 2010;5:574-8.
- [10] Mattevi C, Kim H, Chhowalla M. A review of chemical vapour deposition of graphene on copper. *J Mater Chem* 2011;21:3324-34.
- [11] Kammler HK, MÃ¶dler L, Pratsinis SE. Flame Synthesis of Nanoparticles. *Chem Eng Technol* 2001;24:583-96.
- [12] Xu F, Liu X, Tse SD, Cosandey F, Kear BH. Flame synthesis of zinc oxide nanowires. *Chemical Physics Letters* 2007;449:175-81.
- [13] Xu F, Tse SD, Al-Sharab JF, Kear BH. Flame synthesis of aligned tungsten oxide nanowires. *Appl Phys Lett* 2006;88:243115-3.
- [14] Height MJ, Howard JB, Tester JW, Vander Sande JB. Flame synthesis of single-walled carbon nanotubes. *Carbon* 2004;42:2295-307.
- [15] Xu F, Liu X, Tse SD. Synthesis of carbon nanotubes on metal alloy substrates with voltage bias in methane inverse diffusion flames. *Carbon* 2006;44:570-7.
- [16] Ossler F, Wagner JB, Canton SE, Wallenberg LR. Sheet-like carbon particles with graphene structures obtained from a Bunsen flame. *Carbon* 2010;48:4203-6.
- [17] Li Z, Zhu H, Wang K, Wei J, Gui X, Li X et al. Ethanol flame synthesis of highly transparent carbon thin films. *Carbon* 2011;49:237-41.
- [18] Li Z, Zhu H, Xie D, Wang K, Cao A, Wei J et al. Flame synthesis of few-layered graphene/graphite films. *Chem Commun* 2011;47:3520-2.
- [19] Sidebotham GW, Glassman I. Flame temperature, fuel structure, and fuel concentration effects on soot formation in inverse diffusion flames. *Combust Flame* 1992;90:269,272, IN1, 273-283.

- [20] Li X, Cai W, Colombo L, Ruoff RS. Evolution of Graphene Growth on Ni and Cu by Carbon Isotope Labeling. *Nano Letters* 2009; 2009;9:4268-72.
- [21] Deck CP, Vecchio K. Prediction of carbon nanotube growth success by the analysis of carbon-catalyst binary phase diagrams. *Carbon* 2006;44:267-75.
- [22] Ferrari AC, Meyer JC, Scardaci V, Casiraghi C, Lazzeri M, Mauri F et al. Raman Spectrum of Graphene and Graphene Layers. *Phys Rev Lett* 2006;97:187401.
- [23] Reina A, Jia X, Ho J, Nezich D, Son H, Bulovic V et al. Large Area, Few-Layer Graphene Films on Arbitrary Substrates by Chemical Vapor Deposition. *Nano Letters* 2008; 2009;9:30-5.
- [24] Robertson AW, Warner JH. Hexagonal Single Crystal Domains of Few-Layer Graphene on Copper Foils. *Nano Letters* 2011; 2011;11:1182-9.
- [25] Nair RR, Blake P, Grigorenko AN, Novoselov KS, Booth TJ, Stauber T et al. Fine Structure Constant Defines Visual Transparency of Graphene. *Science* 2008;320:1308-.
- [26] Li X, Magnuson CW, Venugopal A, An J, Suk JW, Han B et al. Graphene Films with Large Domain Size by a Two-Step Chemical Vapor Deposition Process. *Nano Letters* 2010; 2010;10:4328-34.
- [27] Wei D, Liu Y, Wang Y, Zhang H, Huang L, Yu G. Synthesis of N-Doped Graphene by Chemical Vapor Deposition and Its Electrical Properties. *Nano Letters* 2009; 2009;9:1752-8.
- [28] Ferrari AC, Robertson J. Interpretation of Raman spectra of disordered and amorphous carbon. *Phys.Rev.B* 2000;61:14095-107.
- [29] Cuesta A, Dhamelincourt P, Laureyns J, Martínez-Alonso A, Tascón JMD. Raman microprobe studies on carbon materials. *Carbon* 1994;32:1523-32.
- [30] D'Áz J, Paolicelli G, Ferrer S, Comin F. Separation of the sp^3 and sp^2 components in the C1s photoemission spectra of amorphous carbon films. *Phys Rev B* 1996;54:8064-9.
- [31] Liu W, Chung C, Miao C, Wang Y, Li B, Ruan L et al. Chemical vapor deposition of large area few layer graphene on Si catalyzed with nickel films. *Thin Solid Films* 2010;518:S128-32.

Chapter 5

5. Role of Substrate, Temperature, and Hydrogen on the Flame Synthesis of Graphene Films

5.1 Introduction

Transition metals allow the growth of the graphene lattice and provide a low energy pathway for hydrocarbon dissociation [1]. Graphene growth has been demonstrated on a number of metals, i.e. gold (Au), copper (Cu), cobalt (Co), iridium (Ir), nickel (Ni), palladium (Pd), platinum (Pt), rhenium (Re), and ruthenium (Ru) [2,3]. Transition metals in the first row from Iron (Fe) to Cu are of particular interest, due to their low cost and availability. Fe {[Ar] 3d⁶ 4s²} has an asymmetrical distribution of electrons in the d-shell, which gives rise to its high carbon solubility, [Table 5.1](#). When the solubility of C in γ and α phases is exceeded, an intermediate phase Fe₃C (cementite) appears. Cu has a filled 3d shell, with the lowest carbon solubility of the metals examined. Co and Ni, with orbital configurations of 3d⁷ and 3d⁸, respectively, have carbon solubilities that fall in between Fe and Cu. The growth of graphene on Ni occurs primarily in two-steps: (a) carbon atoms are adsorbed onto and incorporated within the Ni substrate, and (b) graphene grows layer by layer due to precipitation (out-diffusion) of carbon atoms from the Ni substrate upon cooling. In contrast, the formation of graphene on Cu occurs purely by a surface growth process [1]. While surface growth also exists for Ni [4], the primary growth mechanism is due to carbon dissolution-precipitation. Hence, owing to its low carbon solubility, Cu is an ideal metal for limiting-the number of graphene layers formed [5]. With Ni and Co, the formation of several layers of graphene is common [2].

Ruoff and co-workers [6] examined the difference in CVD growth of graphene on Ni and Cu, by using carbon isotope (^{12}C and ^{13}C) labeling and examining the Raman spectrum of the graphene, which is different for each isotope. Employing a sequenced delivery of $^{12}\text{CH}_4$ followed by $^{13}\text{CH}_4$, the Ni case showed that the formation of graphene had a random mix of ^{12}C and ^{13}C . Conversely, Cu had regions of only ^{12}C graphene, with the overall growth pattern following the precursor time sequence. Using Fe, CVD growth of graphene is especially challenging, only occurring under very specific conditions [2]. Using flame synthesis [7], we disclosed recently that on Cu, 5 to 8 layers of graphene are grown uniformly across the substrate; while on Ni, the number of layers grown is difficult to control due to the different growth mechanism. With carbon solubility being a critical parameter involved in the growth of graphene, we investigate synthesis on Cu, Ni, Co, Fe, and Cu-Ni alloy. Alloys such as Cu-Ni permit adjustment of the overall carbon solubility, and hence can play an important role in the optimization of the graphene growth process [8].

Metal/Alloy	Carbon Solubility (maximum)	Melting Point
Cu	0.04 at %	1085 °C
Ni	2.7 at %	1455 °C
Co	4.1 at %	1495 °C
Fe*	~7.5 at % (γ)*	1538°C
Cu-Ni alloy ^a	0.04 – 2.7 at %	1085-1455 °C

^a Properties vary according to the atomic ratio of Ni and Cu.

* Carbide formation (e.g. Fe_3C) with >25 at %.

Table 5.1 Properties of the different metals and alloys examined as substrates for graphene growth

Pressure, crystal structure, temperature, and hydrogen also play important roles. In a previous CVD study using acetylene as the carbon source [9], graphene quality improved significantly when increasing the temperature from 700°C to 1000°C. Hydrogen has been shown to impact nucleation, domain size, and growth rate in CVD synthesis [10]. Thus, in this work, the influences of temperature and hydrogen on the growth of graphene are investigated for our flame synthesis method.

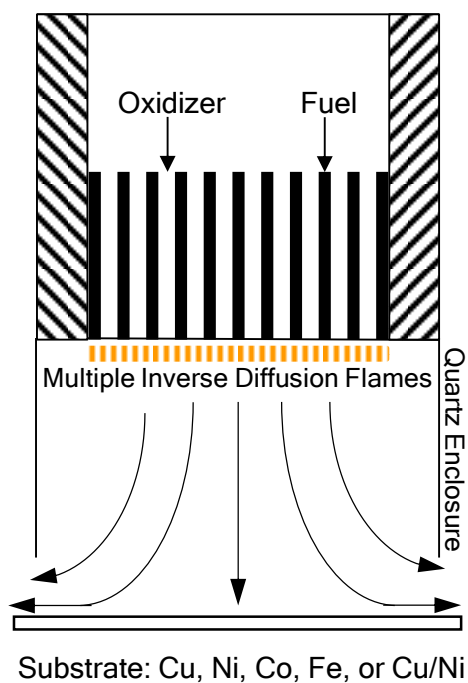


Figure 5.1 Schematic of the experimental setup. Product species of multiple inverse-diffusion flames impinge on a metal substrate (i.e. Cu, Ni, Co, Fe, or Cu/Ni) growing graphene.

5.2 Experimental Procedure

Graphene film growth is examined on 25 μm thick foils of Co, Cu, Fe, Ni, and Cu-Ni (Ni 67% wt, Cu 33% wt) (Alfa Aesar). Prior to synthesis, the metal substrates are reduced by operating the burner with hydrogen as the sole fuel under “globally-rich” conditions for 10 min, thereby removing oxide layers. Afterwards, CH_4 is introduced (with a “global” equivalence ratio of ~ 3) for 5 or 10 min. The 5 min condition is used for Co, Ni, Fe, and Cu-Ni, which helps to control the number of graphene layers. The growth time for Cu is 10 min. The input fuel ratio for CH_4 and H_2 is maintained at 1:10. The substrate is held at a fixed position from the burner and is cooled to regulate the temperature, which is measured using both thermocouple and pyrometer. The typical growth temperature for Cu is 950°C and for Co, Fe, Ni, and Cu-Ni is 850°C . The graphene films are characterized using Raman spectroscopy (Renishaw 1000, laser excitation 514.5 nm), X-ray photoelectron spectroscopy (XPS, Thermo Scientific K-Alpha), transmission electron microscopy (TEM, Topcon 002B), and scanning electron microscopy (FESEM, Zeiss Sigma 8100).

5.3 Results and Discussion

5.3.1 Effect of substrate material

Raman spectroscopy identifies single to few-layer graphene (FLG) [11]. The first order Raman spectra of graphite, is comprised of the D, G, and 2D bands, which are located at shifts of $\sim 1350\text{ cm}^{-1}$, $\sim 1580\text{ cm}^{-1}$, and $\sim 2700\text{ cm}^{-1}$, respectively. The G band is produced by the C-C stretching mode of sp^2 bonded carbon atoms. The 2D band, which is related to the second-order zone boundary phonons, can be used to determine the number of graphene layers. For graphite, this Raman shift is $\sim 2727\text{ cm}^{-1}$; and for a single layer of

graphene, it is $\sim 2660\text{cm}^{-1}$. A 2D peak between these wavenumbers is typically associated with FLG. The ratio between the intensity of the G peak (I_G) and the 2D peak (I_{2D}) can be used to approximate the number of graphene layers. For graphene film synthesized on Cu, $I_G/I_{2D} = 1.35$, Fig. 5.2a, indicating FLG. In combination with Raman, atomic force microscopy, and UV-vis spectroscopy, 5 to 8 layers of graphene are assessed to have grown uniformly on the substrate [7]. The D peak is due to the first-order zone boundary phonons and is used to determine the disorder present in the graphene film. For pristine single-layer graphene, there should be no D peak present. However, as the number of graphene layers increases, a D peak is normally encountered. The intensity ratio between the D peak (I_D) and I_G is used as a metric for the disorder present in the graphene, which develops from domain boundaries, wrinkles, edges, impurities, and other factors. In the case of Cu, due to a surface growth mechanism, small graphene domains are formed, giving rise to a higher D peak. The domain size of the graphene film can be calculated using the following equation [11].

$$\text{Eq. 1: } I_D/I_G = C(\lambda) / L_a,$$

where L_a [nm] is the domain size, λ [nm] wavelength of the incident light, and $C(\lambda)$ is calculated as $2.4 \times 10^{-10} \times \lambda^4$. The typical domain size of graphene on Cu is $\sim 45\text{nm}$. Most applications require the transfer of graphene onto an insulating surface. In the case of Cu, the transfer of the graphene film can be performed by spin-coating a thin layer of polymethylmethacrylate (PMMA) on top of the film and etching away the Cu metal substrate below. The PMMA is then dissolved using hot acetone. Figure 5.2b shows a transferred graphene film onto quartz, and the inset shows the transfer onto SiO_2/Si .

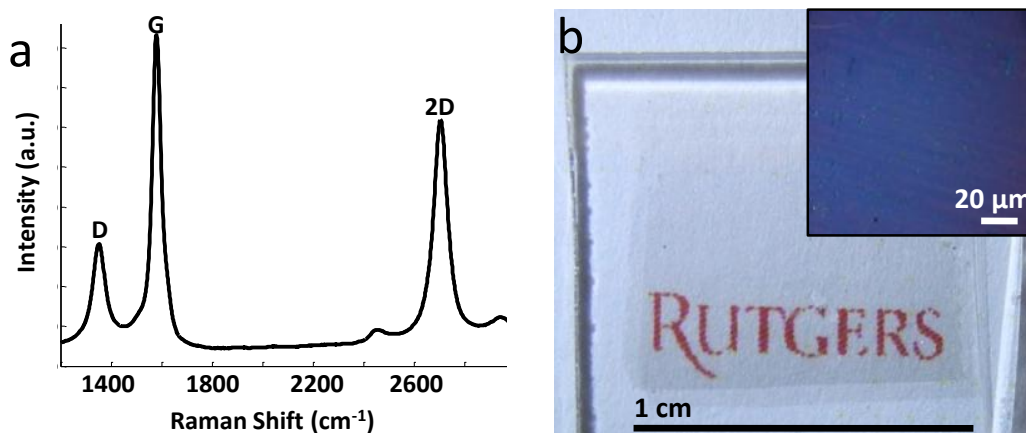


Figure 5.2 Growth of few-layer graphene (FLG) film on Cu. (a) Raman spectrum of the film. (b) Photograph of the film transferred on quartz; the inset shows the film transferred onto a SiO_2/Si substrate.

Growth characteristics of graphene films grown on Ni, Co, and Cu-Ni alloy are shown in [Fig 5.3a](#). The Raman spectra illustrate similar growth on all three substrates. Carbon atoms readily dissolve within the Ni and Co substrates (given higher solubilities compared to Cu), with graphene growth ensuing upon cooling. A lower D peak, compared to that for Cu, is observed for all three substrates, where the typical domain sizes of the graphene films are 150nm, 70nm, and 50nm for Ni, Co, and Cu-Ni, respectively,. The relatively higher D peak for the Cu-Ni alloy is likely due to the presence of Cu, and to the increased role of a surface growth mechanism. TEM shows the well-defined crystalline structure of the graphene film on Ni, [Fig. 5.3b](#).

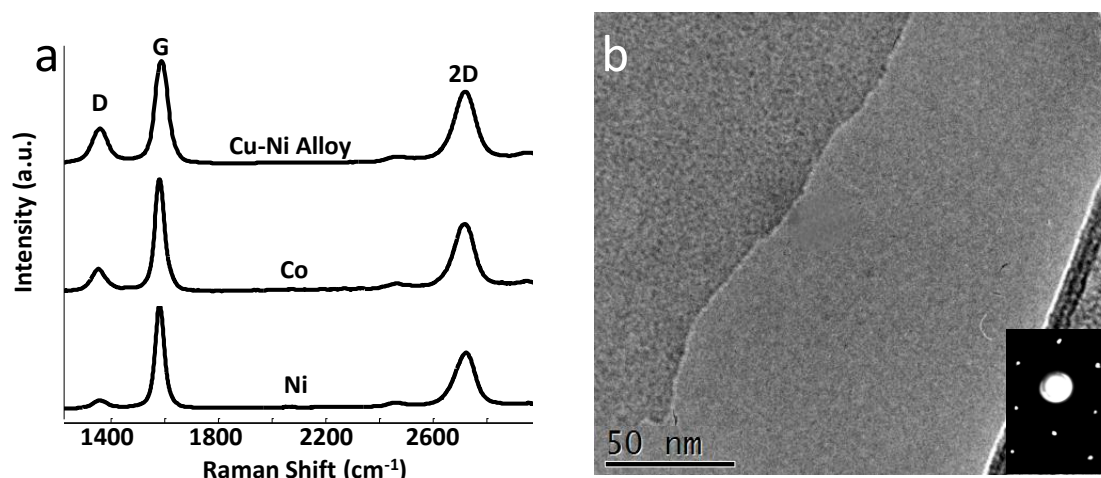


Figure 5.3 Growth of few-layer graphene (FLG) film on Ni, Co, and Cu-Ni. (a) Raman spectra of the graphene films. (b) TEM image of the graphene film synthesized on Ni, with the inset showing the diffraction pattern.

From the phase diagram of nickel and carbon, at temperatures above 800°C , Ni and C form a metastable solid phase Ni_3C [2]. Upon cooling, the carbon diffuses out of the Ni to form graphene layers. A similar process occurs for Co, except that diffusion and nucleation of graphene takes place at the grain boundaries. As a result, controlling the number of graphene layers on a large Ni or Co substrate is difficult. Additionally, the number of graphene layers is typically greater at the grain boundaries, resulting in the formation of wrinkles [2]. As seen in the local contrasts within the FESEM image, [Fig.5.4c](#), the number of graphene layers across Ni varies. [Figure 5.4d](#) shows the formation of wrinkles at the grain boundaries of the underlying Ni. Graphene growth on Cu is not caused by the out-diffusion of carbon atoms, given that only a trivial amount of carbon is absorbed into bulk copper, but rather by breakdown of the hydrocarbon gas on the surface. Once the copper surface is covered by graphene, the formation of any additional carbon structure [1] is deactivated. Hence Cu has proven to be especially

effective in limiting the growth of graphene layers. A uniform graphene film on Cu is observed from the FESEM image, Fig. 5.4a. Moreover, no wrinkles form at the Cu grain boundaries. The additional layers formed on Ni seem to be confirmed by Figs. 5.4c and 5.4d, which show darker areas where FLG has detached locally from the substrate, probably due to a combination of growth stresses and thermal expansion misfit stresses during cooling after deposition. These effects are dependent critically on film thickness; the fewer the layers, the less susceptible the film is to delamination. Although lower D peaks typify Ni and Co, Cu is preferred normally because it yields more uniform graphene.

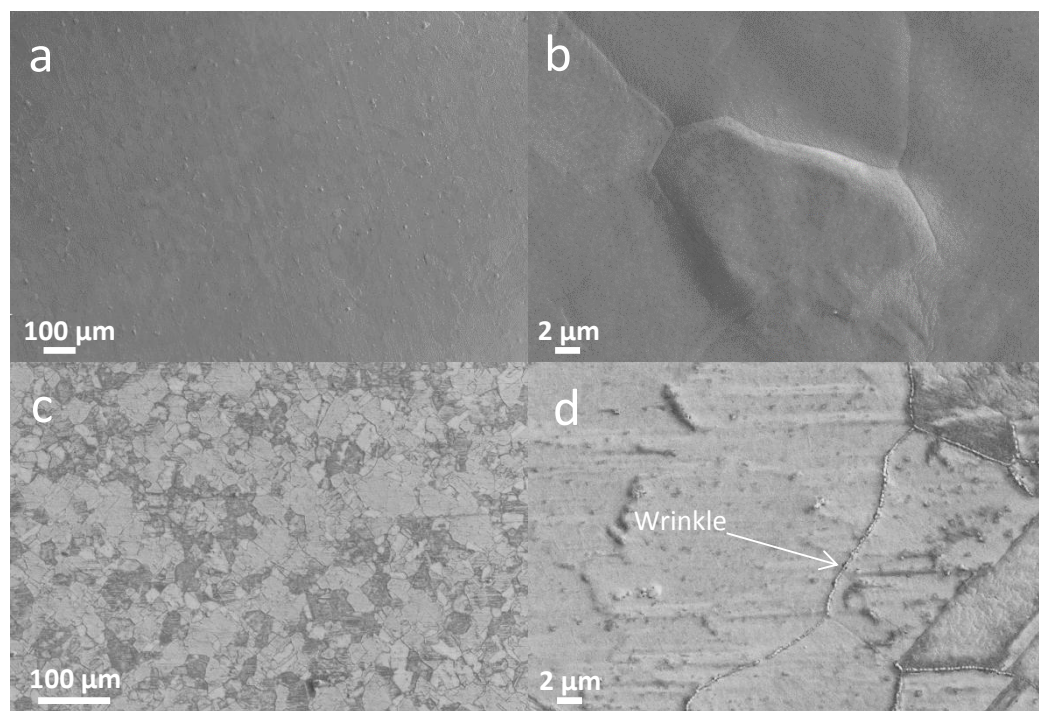


Figure 5.4 FESEM images comparing the growth of graphene on Cu and Ni. (a) Low magnification image of graphene film on Cu. (b) High magnification image of graphene film on Cu. (c) Low magnification image of graphene film on Ni. (d) High magnification image of graphene film on Ni.

Unlike the cases for Cu, Ni, and Co, the growth of graphene is not exclusively observed on Fe, despite the presence of a Raman 2D peak (Fig 5.5a) indicating graphitic-type structure [11]. Although carbon is highly soluble within Fe (see Table 5.1), Fe_3C readily forms, which can break up the Fe substrate surface. As a result, a disordered structure can result, Fig. 5.5b, with Raman corroborating a large D peak (Fig 5.5a). . For the cases of Ni and Co, which have higher carbon solubilities than that for Cu, lower D peaks are observed compared to that for Cu. However, for the case of Fe, which has higher carbon solubility than that for Ni and Co, a higher D peak is observed compared to those for Ni, Co, or Cu. Similarly, a higher D peak is observed for Co compared to that for Ni. While growth of FLG has been observed on Fe using CVD [12], no such growth is observed in our flame synthesis process. In typical thermal CVD, hydrocarbon dissociation on the metal surface constrains the amount of carbon atoms present [1]. As such, single-layer graphene is attainable on various metals. In our setup, the post-flame gases are already comprised of relevant carbon-rich pyrolysis species and radicals, supplying carbon atoms at quantities that are perhaps too copious for constrained graphene formation, overgrowing into a disordered structure.

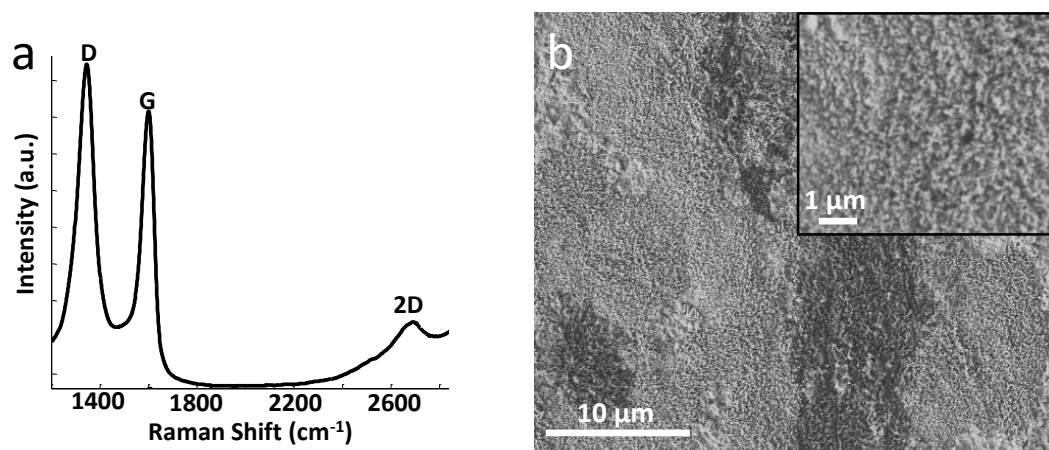


Figure 5.5 Growth of a disordered graphitic structure on Fe. (a) Raman spectrum of the material. (b) Low magnification FESEM image of the material growth on Fe; the inset shows a high magnification image.

5.3.2 Effect of substrate temperature

Conventional CVD synthesis of graphene on transitional metals involves high substrate temperatures, which are critical for hydrocarbon dissociation within the thermal boundary layer. At substrate temperatures below 850 °C, no growth of graphene occurs on Cu [13]. However, lower temperature growth is critical for industrial feasibility and economic cost. Recently, low temperature growth of graphene has been reported using microwave [14] and plasma enhanced [15] CVD. The plasma or microwave source provides hydrocarbon dissociation to enable low-temperature growth of graphene. However, in such cases, a large D (disorder) is typically encountered. In our setup, combustion provides hydrocarbon dissociation such that post-flame gases are comprised of relevant carbon-rich pyrolysis species (such as CO and C_n); therefore high substrate temperatures are not necessary for graphene growth.

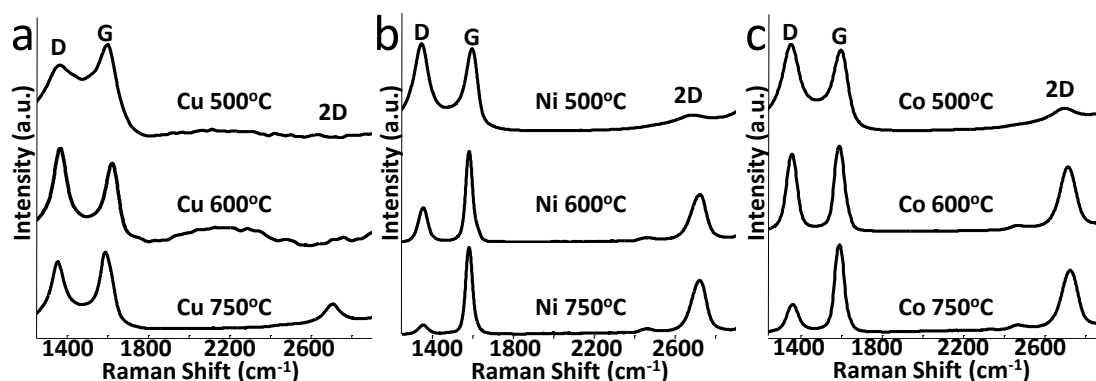


Figure 5.6 Analysis of the influence of temperature on the growth of graphene. (a) Raman spectrum on Cu. (b) Raman spectrum on Ni. (c) Raman spectrum on Co.

Raman spectroscopy analyzes the influence of substrate temperature on graphene growth, [Fig. 5.6](#). For Cu at 750°C, the 2D peak indicates the presence of graphitic-type structure. However, the large D peak stems from a small domain size of 20nm for the film. The graphene film at this temperature is easily transferred onto an insulating surface. Further reduction of the temperature to 600°C or 500°C results in the formation of an amorphous carbon film [16], with no 2D peak present, [Fig 5.6a](#). For Ni and Co, growth of high quality graphene films is observed at 750°C, where the domain sizes are 100nm and 50nm, for Ni and Co, respectively. At a temperature of 600°C, graphene films on Ni or Co are still observed, although higher D peaks are associated, with the D peak for Co being usually higher than that for Ni. The surface growth mechanism for Cu requires higher growth temperatures, while the precipitation growth mechanism upon cooling can transpire at lower temperatures. Thus, the choice of metal substrate can play an important factor in the growth of low temperature graphene. In all three cases of Cu,

Ni, and Co, higher D peaks are encountered at lower temperatures; therefore, the temperature of the substrate also determines the domain size of the graphene film.

When the growth temperature of Ni or Co is further lowered to 500°C, a small 2D peak appears, [Fig. 5.6b](#) and [Fig. 5.6c](#), representative of graphitic-type structure. FESEM divulges the growth of carbon nanotubes (CNTs), [Fig. 5.7a](#). Flame synthesis of CNTs is facilitated by catalytic nanoparticle formation, which precedes the initiation and growth of CNTs. On bulk metals, nanoparticle formation can follow due to the carbide-induced breakup of the substrate [17,18]. Nevertheless, at 500°C, carbon solubility of Ni and Co is limited, inhibiting the formation of carbides. Thus, nanoparticle formation likely happens during hydrogen flame reduction of the thin oxide layers, which are present on Co and Ni. In both cases, the growth of CNTs on Ni and Co is not uniform across the substrate, presumably due to a paucity of nanoparticles. In previous flame synthesis studies, albeit for different configurations and conditions, alloys of Ni yielded higher densities of CNTs [19]. Likewise, for Cu-Ni substrate at 500°C, CNTs grow uniformly across the substrate, [Fig 5.7b](#) and [Fig 5.7c](#). This higher yield may be due to breakup of the surface oxide, [Fig. 5.7d](#), leading to plentiful nanoparticles on the substrate. Notwithstanding, it is not entirely clear if the breakup occurs due to it being an alloy or to the method in which it is manufactured. No CNTs are grown on the Cu substrate.

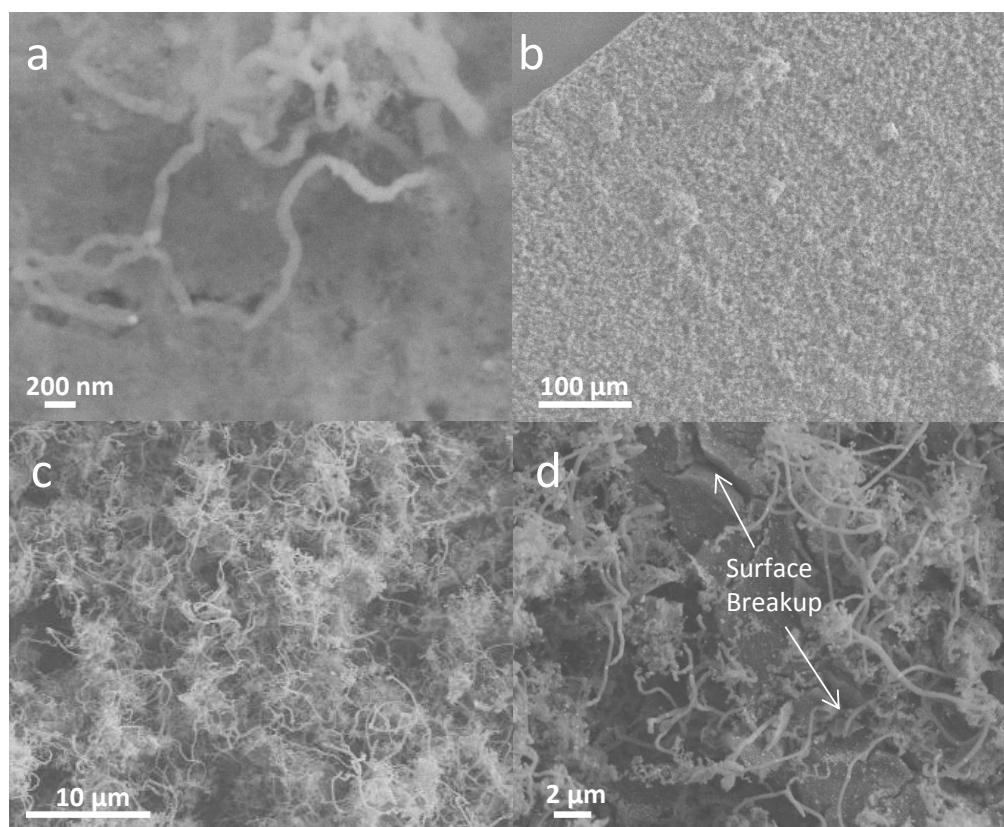


Figure 5.7 FESEM image showing the low-temperature (500 °C) growth condition. (a) High magnification image on Ni. (b,c) Low magnification image on Cu-Ni. (d) High magnification image on Cu-Ni.

5.3.3 Effect of hydrogen

The effect of hydrogen on the growth of graphene is investigated for Cu as substrate. Cu has an oxide surface layer that can inhibit graphene growth [2]. XPS is performed on the Cu substrate before and after graphene growth, Fig. 5.8a. The broad Cu(2p_{3/2}) and Cu(2p_{1/2}) peaks, for the as-received Cu foil, confirm the presence of various copper oxides (Cu₂O, CuO) [[20]. After graphene growth, sharper Cu(2p_{3/2}) and Cu(2p_{1/2}) peaks are observed, indicating removal of the oxide layer [20]. A hydrogen reducing environment enables removal of the oxide layer. When the Cu foil is not treated in a

hydrogen reducing environment prior to the growth of graphene, the Raman spectrum reveals that the film is highly disordered, [Fig. 5.8b](#), and non-uniform across the substrate. The hydrogen reduction pre-treatment also enlarges the Cu grain size for higher quality graphene [2]. Besides the initial reduction of the oxide layer, hydrogen is needed during the growth process of graphene. Carbon atoms are thermodynamically unfavorable on Cu [21]; and hydrogen aids the formation of active carbon species (primarily CH_x) on the Cu surface for graphene growth. Moreover, hydrogen etches away unwanted weak carbon-carbon bonds [10]. In atmospheric pressure CVD (APCVD), the growth of graphene is strongly dependent on hydrogen concentration. With insufficient hydrogen, the graphene film tends to be disordered [1], and no graphene is grown in the absence of hydrogen [10]. On the other hand, the growth of graphene is achievable during flame synthesis, without externally-added hydrogen, [Fig. 5.8b](#), because the fuel-rich combustion of methane inherently produces hydrogen along with carbon-rich pyrolysis species. However, the quality of the graphene film is modest, as evident from the Raman spectrum. Thus, hydrogen addition is needed to grow high-quality graphene films with large domain size.

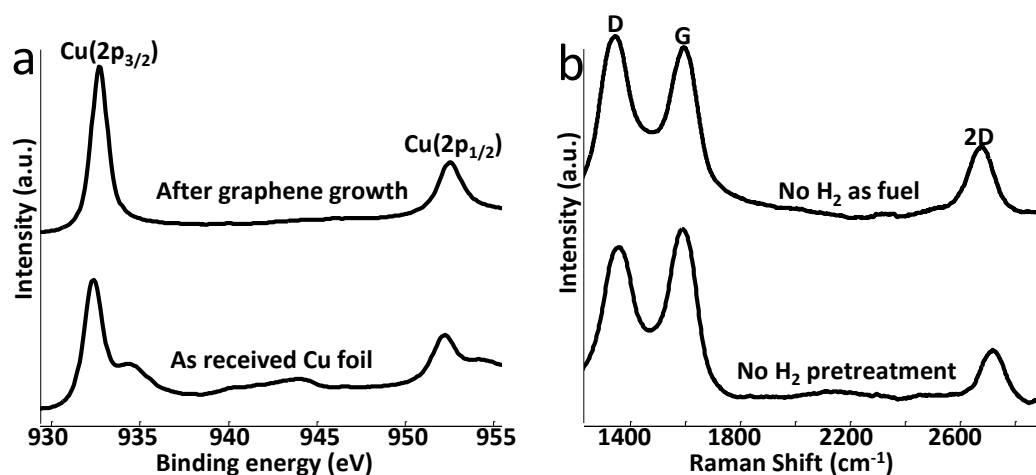


Figure 5.8 (a) XPS core-level Cu 2p spectrum of the Cu foil before and after the growth of graphene. (b) Raman spectrum of the film with no H_2 pretreatment (but H_2 is used during the growth process) and no external H_2 as fuel during the growth process (but H_2 is used during the pretreatment process).

5.4 Concluding Remarks

Flame synthesis of graphene is investigated on Cu, Ni, Co, Fe, and Cu-Ni substrates. On Cu, FLG is grown uniformly across the substrate. Ni offers the advantage of a lower disorder graphene, but the growth is not uniform across the substrate, with formation of wrinkles appearing along the grain boundaries. The graphene quality is slightly higher on Ni compared to that on Co or Cu-Ni alloy. On Fe, no graphene film is found to grow.

Flame synthesis offers the advantage of providing various gaseous carbonaceous species, which can enable the low temperature growth of graphene. Graphene films are observed on Ni and Co at temperatures from 600°C to 750°C. In the case of Cu, graphene grows at 750°C, but amorphous carbon develops at 600°C. In all cases, higher temperatures produce better quality graphene films. Starting at 500°C, CNTs grow on Ni, Co, and Ni-Cu. CNT yield on Ni-Cu alloy is abundant due to ready breakup of the

surface oxide. Hydrogen plays crucial roles in graphene growth by removing oxide layers on and by modifying grain size of the substrate prior to synthesis (without which the graphene film is not uniform and highly disordered), facilitating the formation of active species for synthesis, and etching away sp^3 carbon during synthesis to produce high quality graphene films. Other parameters such as pressure, crystal structure, and cooling rate are currently being investigated, along with measuring species concentrations using laser-based diagnostics to determine local growth conditions. The novel multiple inverse-diffusion flame burner is expected to enable the scalable production of advanced sp^2 carbon nanomaterials, from 0D fullerenes to 1D CNTs to 2D graphene.

5.5 References

- [1] Bhaviripudi S, Jia X, Dresselhaus MS, Kong J. Role of Kinetic Factors in Chemical Vapor Deposition Synthesis of Uniform Large Area Graphene Using Copper Catalyst. *Nano Lett* 2010;10:4128-33.
- [2] Mattevi C, Kim H, Chhowalla M. A review of chemical vapour deposition of graphene on copper. *J Mater Chem* 2011;21:3324-34.
- [3] Oznuluer T, Pince E, Polat EO, Balci O, Salihoglu O, Kocabas C. Synthesis of graphene on gold. *Appl Phys Lett* 2011;98:183101-3.
- [4] Weatherup RS, Bayer BC, Blume R, Ducati C, Baehtz C, Schlögl R et al. In Situ Characterization of Alloy Catalysts for Low-Temperature Graphene Growth. *Nano Lett* 2011;11:4154-60.
- [5] Li X, Cai W, An J, Kim S, Nah J, Yang D et al. Large-Area Synthesis of High-Quality and Uniform Graphene Films on Copper Foils. *Science* 2009;324:1312-4.
- [6] Li X, Cai W, Colombo L, Ruoff RS. Evolution of Graphene Growth on Ni and Cu by Carbon Isotope Labeling. *Nano Lett* 2009;9:4268-72.
- [7] Memon NK, Tse SD, Al-Sharab JF, Yamaguchi H, Goncalves AB, Kear BH et al. Flame synthesis of graphene films in open environments. *Carbon* 2011;49:5064-70.

- [8] Chen S, Cai W, Piner RD, Suk JW, Wu Y, Ren Y et al. Synthesis and Characterization of Large-Area Graphene and Graphite Films on Commercial Cu–Ni Alloy Foils. *Nano Lett* 2011;11:3519-25.
- [9] Chae SJ, Güneş F, Kim KK, Kim ES, Han GH, Kim SM et al. Synthesis of Large-Area Graphene Layers on Poly-Nickel Substrate by Chemical Vapor Deposition: Wrinkle Formation. *Adv Mater* 2009;21:2328-33.
- [10] Vlassioulakos I, Regmi M, Fulvio P, Dai S, Datskos P, Eres G et al. Role of Hydrogen in Chemical Vapor Deposition Growth of Large Single-Crystal Graphene. *ACS Nano* 2011;5:6069-76.
- [11] Andrea C. F. Raman spectroscopy of graphene and graphite: Disorder, electron–phonon coupling, doping and nonadiabatic effects. *Solid State Commun* 2007;143:47-57.
- [12] Yao Y, Li Z, Lin Z, Moon K, Agar J, Wong C. Controlled Growth of Multilayer, Few-Layer, and Single-Layer Graphene on Metal Substrates. *J Phys Chem C* 2011;115:5232-8.
- [13] Regmi M, Chisholm MF, Eres G. The effect of growth parameters on the intrinsic properties of large-area single layer graphene grown by chemical vapor deposition on Cu. *Carbon* 2012;50:134-41.
- [14] Yuan GD, Zhang WJ, Yang Y, Tang YB, Li YQ, Wang JX et al. Graphene sheets via microwave chemical vapor deposition. *Chemical Physics Letters* 2009;467:361-4.
- [15] Kim J, Ishihara M, Koga Y, Tsugawa K, Hasegawa M, Iijima S. Low-temperature synthesis of large-area graphene-based transparent conductive films using surface wave plasma chemical vapor deposition. *Appl Phys Lett* 2011;98:091502-3.
- [16] Cuesta A, Dhamelincourt P, Laureyns J, Martínez-Alonso A, Tascón JMD. Raman microprobe studies on carbon materials. *Carbon* 1994;32:1523-32.
- [17] Xu F, Liu X, Tse SD. Synthesis of carbon nanotubes on metal alloy substrates with voltage bias in methane inverse diffusion flames. *Carbon* 2006;44:570-7.
- [18] Xu F, Zhao H, Tse SD. Carbon nanotube synthesis on catalytic metal alloys in methane/air counterflow diffusion flames. *Proceedings of the Combustion Institute* 2007;31:1839-47.
- [19] Merchan-Merchan W, Saveliev AV, Kennedy L, Jimenez WC. Combustion synthesis of carbon nanotubes and related nanostructures. *Progress in Energy and Combustion Science* 2010;36:696-727.

- [20] Chen S, Brown L, Levendorf M, Cai W, Ju S, Edgeworth J et al. Oxidation Resistance of Graphene-Coated Cu and Cu/Ni Alloy. *ACS Nano* 2011;5:1321-7.
- [21] Zhang W, Wu P, Li Z, Yang J. First-Principles Thermodynamics of Graphene Growth on Cu Surfaces. *J Phys Chem C* 2011;115:17782-7.

Chapter 6

6. CNT Synthesis on Transitional Metal Alloys

6.1 Introduction

The unique flame setup employed in this chapter is the multiple inverse-diffusion flame. Earlier reports for CNT synthesis using flames involved the use of normal diffusion flames (NDFs) [1] and premixed flames (PFs) [2]. More recently, the growth of CNTs was demonstrated using a single inverse-diffusion flame (IDF) [3]. IDF offers several key advantages for the growth of CNTs when compared to NDF and PF [3]. However, due to large gradients present in a single diffusion flame, it is difficult to scale the growth of CNTs across a large substrate. The multiple inverse-diffusion flame enables has no scaling problems, as the flow velocity is independent of the overall burner diameter. Since many small diffusion flames are used, overall radially-flat profiles of temperature and chemical species occur downstream from the burner. This ensures uniform growth across the substrate.

The growth of CNTs is investigated on various transition-metal alloy substrates. Under suitable conditions, the formation of catalytic nanoparticles occurs, and carbon-based species undergo dissociative adsorption and diffuse into the catalytic nanoparticles for CNT growth [4]. The nanoparticles either detach from the substrate and are situated at the tip of the CNT or remain attach to the surface of the substrate and are situated at the base of the CNT. For the growth of CNTs directly on transition-metals, catalytic nanoparticle formation primarily occurs due to surface breakup induced by surface carbonization. Carbide induced breakup of the surface is commonly reported as the CNT

growth mechanism for rich hydrocarbon-based flames [3,5]. Once the dissolved carbon reaches a threshold concentration, the formation of carbide occurs, and due to lattice mismatch between the carbide phase and the transition-metal stresses form on the substrate surface. Surface breakup typically appears along the weakest regions, such as grain boundaries and edge dislocations, due to the increased lattice stress and higher carbon concentration. Such growth mechanism results in the formation of a wide variety of geometries and sizes [6-8]. Other mechanisms for the formation of nanoparticles on a substrate, include hydrogen reduction and evaporation-condensation [3]. For the hydrogen reduction mechanism, the presence of oxygen species, such as OH near the flame front, can result in the local oxidation of the substrate, which can then be reduced due to any hydrogen species within the flame. Under the evaporation-condensation mechanism the surface metal evaporates and then diffuses back, where it can condensate as nanoparticles. Based on prior studies [3], the hydrogen reduction and evaporation-condensation mechanism play a limited role in the growth of CNTs. Firstly, oxygen species that readily breakdown, such as OH, only exist near the flame front, which is not suitable for the growth of CNTs. Secondly, with a growth temperature much lower than the melting point, the production of metal vapor is minimal. Hence the dominant mechanism for CNT growth is due to the carbide breakup of the surface. Due to different carbon solubilities within metals, the type of metal or metal alloy plays a critical factor in the growth of CNTs.

6.2 Experimental Setup

CNTs are grown on different transition-metal substrates (Fe, Ni/Cr/Fe, and Ni/Ti), which are listed in [Table 6.1](#). The substrates are cleaned in ethanol using an ultrasonic cleaner, and then are air-dried. The same multiple inverse diffusion-flame that was used for the growth of graphene, (Chapter 4 [Fig. 1](#)), is used for CNT synthesis, with ethylene as the sole fuel source. The substrate is held within the flame for 10 minutes. A silica-coated 125 μm Pt/Pt-10%Rh thermocouple (S-type) measures the gas phase temperature to be around 800°C. After synthesis, the substrate is examined directly using Field Emission Scanning Electron Microscopy (FESEM).

Chemical Composition	Melting Point (K)
99.95% Fe	1808
56% Ni / 44% Ti	1583
60% Ni / 16% Cr / 24% Fe	1623

Table 6.1 Catalytic metal alloys investigated

6.3 Results and Discussion

The growth of CNTs using combustion is a complex process, where both nanoparticle formation and CNT growth occur under very specific conditions. Using the multiple diffusion flame setup, the growth of CNTs only occurs under inverse (fuel rich) conditions, where the oxygen is completely consumed. In this chapter the growth of CNTs is investigated on different alloy composition. The growth of micro- and nano-scale carbon fibers and tubes are observed on the Fe substrate, [Fig 6.1](#). Large scale

growth is observed across the substrate, Fig. 6.1a, however the tubes tend to be twisted, coiled, and entangled. While there is a large distribution in the diameter of the CNTs grown using the Fe substrate, CNTs with a diameter of 100nm to 150nm are commonly observed using FESEM, Fig. 6.1d. Next the growth of CNTs is investigated using Ni/Cr/Fe, where large quantities of CNTs cover the substrate, Fig. 6.2a. The CNTs are of fairly uniform diameter, ranging from 30nm to 50nm. Additionally, regions of vertically-aligned CNTs are obtained from the Ni/Cr/Fe substrate, Fig. 6.2d.

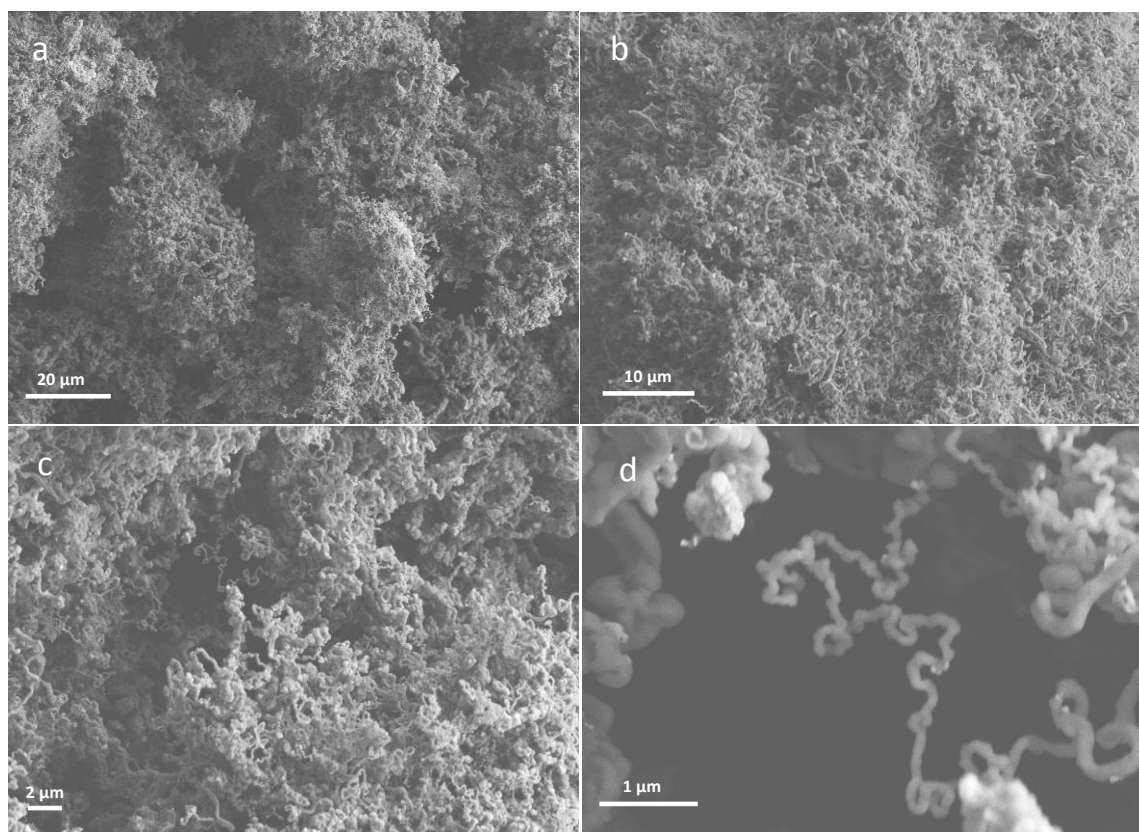


Figure 6.1 FESEM images of CNT morphology using a Fe substrate.

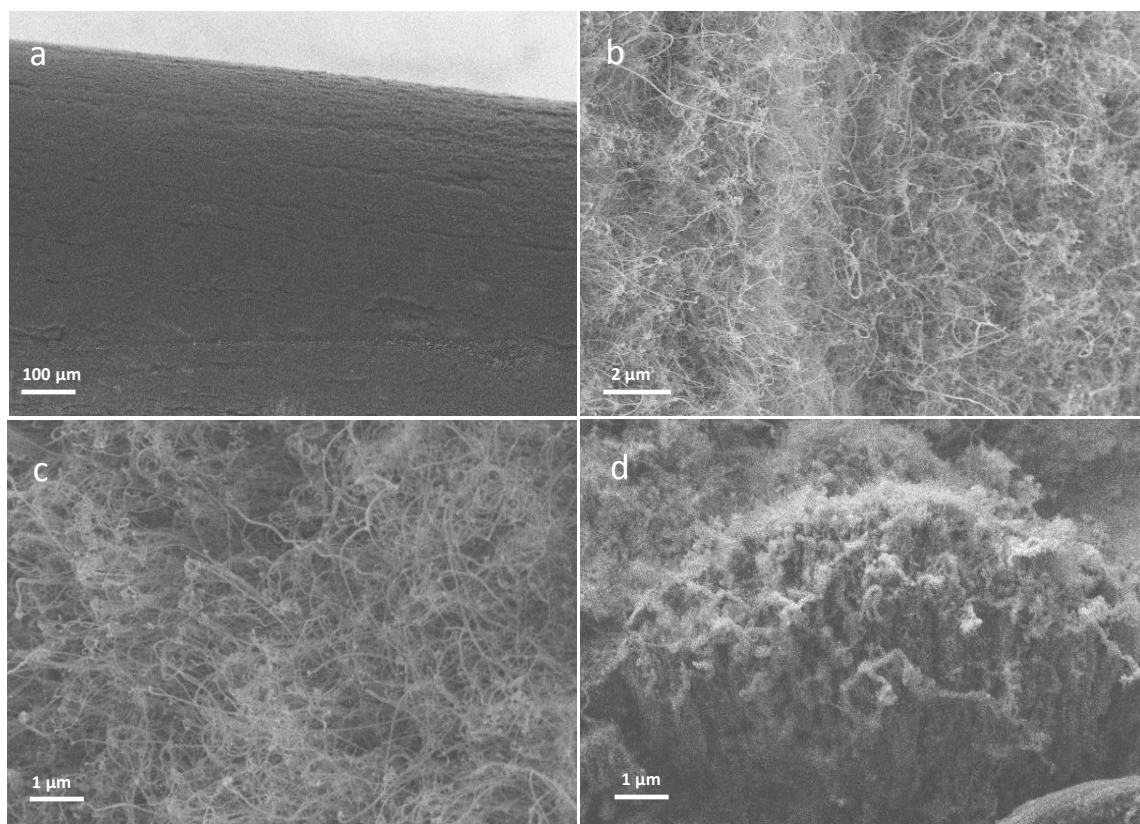


Figure 6.2 FESEM images of CNT morphology using a Ni/Cr/Fe substrate.

The difference in the quality of CNTs obtained from the Fe substrate, compared to the Ni/Cr/Fe substrate, can possibly be attributed to the difference in the carbon solubility between Fe and Ni. Fe has higher carbon solubility [9] when compared to Ni, which can result in significant quantities of micro- and nano-sized particles. Hence, larger diameter CNTs are observed on the Fe substrate. In the case of Ni, the formation of nanoparticles is more uniform and limited [5], thus explaining the smaller diameter of CNTs. Similar to the growth on Ni/Cr/Fe, large quantities of CNTs cover the Ni/Ti substrate, [Fig. 6.3a](#). The CNTs grown on Ni/Ti are fairly uniform with a typical diameter that is less 50nm. Based on these results, nickel alloys result in higher quality CNT growth with small

diameters when compared to the growth of CNTs using Fe. Similar results have been observed in prior flame synthesis studies [3,5].

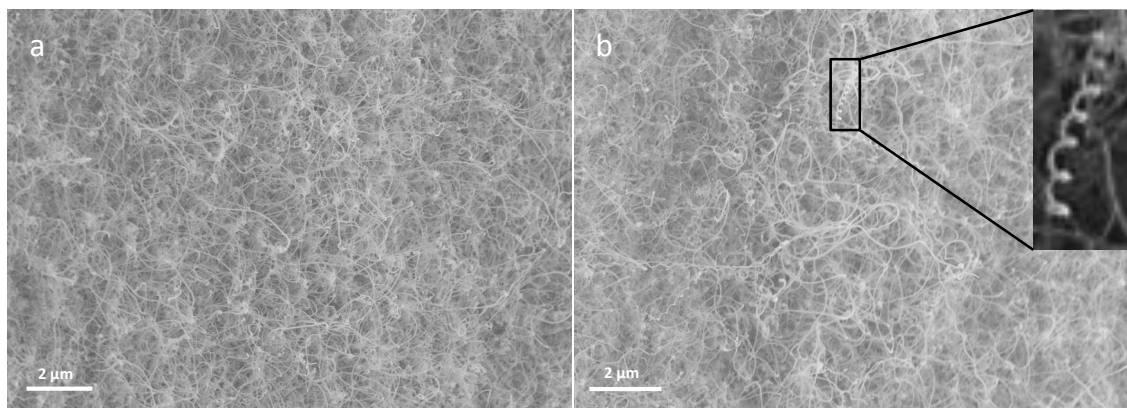


Figure 6.3 FESEM images of CNT morphology using a Ni/Ti substrate.

The growth of coiled CNT structures is also observed on the Ni/Ti substrate, [Fig. 6.3b](#) inset. Such growth occurs due to the introduction of defects (pentagon rings and heptagon rings) into the hexagonal rings [10], which is caused by the shape of the catalyst particle. Distinct crystalline facets of the catalyst particle can have different carbon precipitation rates during the CNT growth process. This results in an uneven extrusion velocity of carbon, which can introduce pentagon and heptagon rings ([Fig. 6.4](#)).

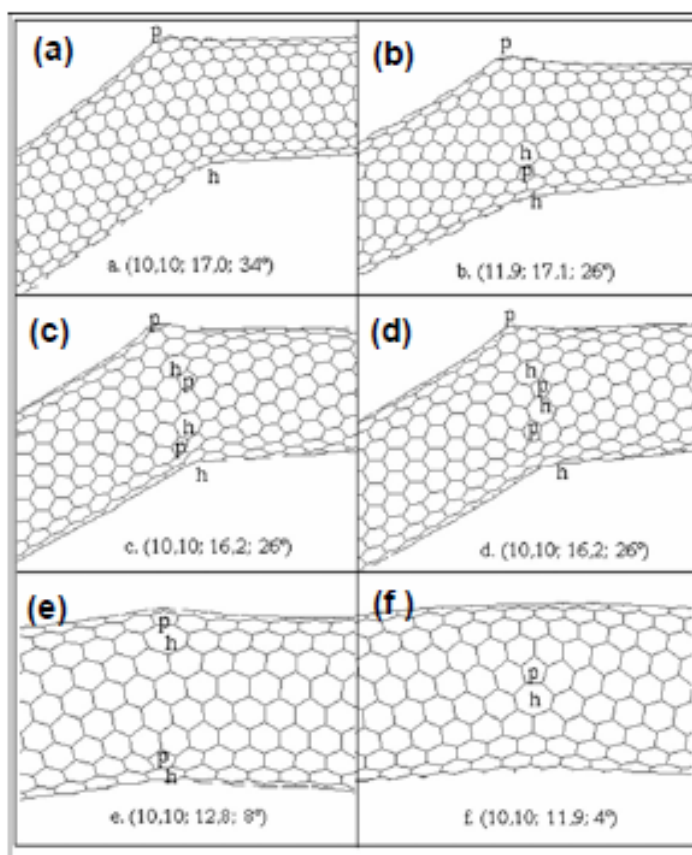


Figure 6.4 Simulated SWNT bends. (a) A 34° bend from a pentagon and heptagon defect on opposite sides. (b) – (d) from three pentagon-heptagon defects on different sides. (e) A 8° bend from two fused defects. (f) A 4° bend from a fused defect. (Reproduced with citation [10])

6.4 Concluding Remarks

Transition metals (e.g. Ni, Co, and Fe) and their alloys are well known to serve as catalysts for CNT growth. Under the right conditions, catalyst nanoparticles are formed, and carbon-based precursor species readily undergo dissociative adsorption and diffuse through the catalyst nanoparticles and grow into CNTs. Using our flame setup, no pretreatment of the substrate is needed; our single-step method induces catalyst nanoparticle formation along with subsequent CNT growth. With the temperature and

chemical species concentrations in the post-flame gases radially flat, uniform synthesis of CNTs is possible across large substrates. The growth of CNTs is demonstrated on Fe, Ni/Cr/Fe/, and Ni/Ti substrates and it is shown that the alloy composition strongly impacts CNT morphology. Higher quality CNTs with smaller diameters are observed on Ni/Cr/Fe and Ni/Ti when compared to the CNTs from Fe.

6.5 References

- [1] Yuan L, Saito K, Pan C, Williams FA, Gordon AS. Nanotubes from methane flames. *Chemical Physics Letters* 2001;340:237-41.
- [2] Randall L VW. Fe-catalyzed single-walled carbon nanotube synthesis within a flame environment. *Combust Flame* 2002;130:37-47.
- [3] Xu F, Liu X, Tse SD. Synthesis of carbon nanotubes on metal alloy substrates with voltage bias in methane inverse diffusion flames. *Carbon* 2006;44:570-7.
- [4] Merchan-Merchan W, Saveliev AV, Kennedy L, Jimenez WC. Combustion synthesis of carbon nanotubes and related nanostructures. *Progress in Energy and Combustion Science* 2010;36:696-727.
- [5] Xu F, Zhao H, Tse SD. Carbon nanotube synthesis on catalytic metal alloys in methane/air counterflow diffusion flames. *Proceedings of the Combustion Institute* 2007;31:1839-47.
- [6] Jablonski GA, Geurts FW, Sacco jr. A, Biederman RR. Carbon deposition over Fe, Ni, and Co foils from CO-H₂-CH₄-CO₂-H₂O, CO-CO₂, CH₄-H₂, and CO-H₂-H₂O gas mixtures: I. Morphology. *Carbon* 1992;30:87-98.
- [7] Jablonski GA, Geurts FWAH, Sacco Jr. A. Carbon deposition over Fe, Ni, and Co foils from CO-H₂-CH₄-CO₂-H₂O, CO-CO₂, CH₄-H₂, and CO-H₂-H₂O gas mixtures: II. Kinetics. *Carbon* 1992;30:99-106.
- [8] Soneda Y, Makino M. Formation and texture of carbon nanofilaments by the catalytic decomposition of CO on stainless-steel plate. *Carbon* 2000;38:478-80.

- [9] Liu N, Fu L, Dai B, Yan K, Liu X, Zhao R et al. Universal Segregation Growth Approach to Wafer-Size Graphene from Non-Noble Metals. *Nano Lett* 2011;11:297-303.
- [10] Han J, Anantram MP, Jaffe RL, Kong J, Dai H. Observation and modeling of single-wall carbon nanotube bend junctions. *Phys Rev B* 1998;57:14983-9.

Chapter 7

7. Transitioning Growth from CNTs to Graphene Films on Nickel Alloys

7.1 Introduction

Allotropes of carbon, specifically graphene and carbon nanotubes (CNTs) are the subject of great scientific interest. Graphene and CNTs, comprised of sp^2 -bonded carbon atoms, exhibit remarkable electrical and mechanical properties, with the potential to replace silicon in electronic devices [1,2]. The growth of carbon nanomaterials on metals has been well studied using chemical vapor deposition (CVD). Graphene can be grown on Copper (Cu) [3] and Nickel (Ni) [4] foils at temperatures $\sim 1000^\circ\text{C}$. The temperature and substrate composition are of critical importance in the growth of graphene [5,6]. For CNTs, the substrate is normally seeded with catalytic nanoparticles (Ni, Co, or Fe), with a typical growth temperature $\sim 500^\circ\text{C}$ [7]. While CVD has emerged as the leading technology for the production of graphene and CNTs, the processes are costly, require lengthy processing times, and are restricted to confined synthesis.

A common requirement in the growth of carbon nanomaterials is a carbon feedstock and heat. Flame synthesis offers the advantage of efficiently providing both elevated temperature and precursor carbon species for growth. Recently, we reported the growth of few-layer graphene (FLG) films on Cu and Ni substrates using flame synthesis [8] in open environments (chapter 4). The growth of CNTs [9-11] using flame synthesis has been widely demonstrated, however this chapter evinces that by varying the temperature, growth can transition between CNTs and FLG. Additionally, while the growth of CNTs has been demonstrated on a number of Nickel alloys [9,10,12] (Cu-Ni,

Ni-Fe-Cr, Ni-Ti, and Co-Ni), the growth of graphene has only been demonstrated on Cu-Ni [13]. Finally, our system requires no prior substrate preparation, permits open-environment processing, and affords high growth rates.

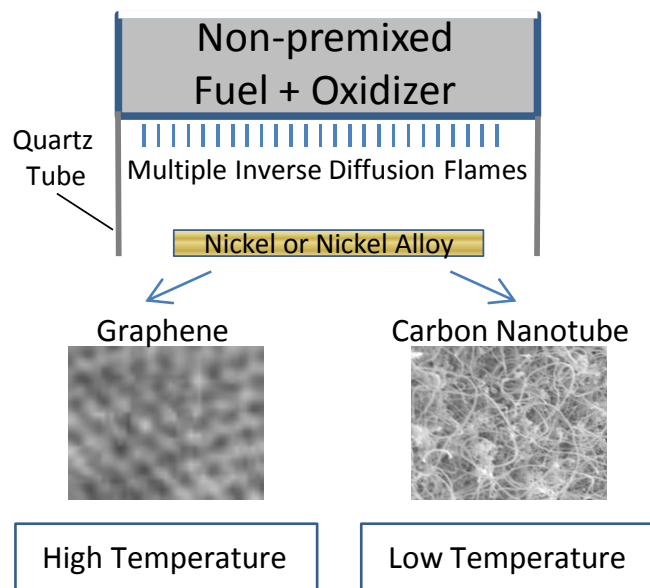


Figure 7.1 Schematic diagram of the experimental setup. The substrate (Ni, Cu-Ni, Inconel, or nitinol) is held at a high temperature (850°C) or a low temperature (500°C).

7.2 Experiment

In our setup, the pyrolysis gases of a multiple-diffusion-flame burner [8] impinges on a substrate, enabling the growth of carbon nanomaterials (see Fig. 7.1). The burner operates in an inverse mode, where for each distinct flame in the planar array, oxidizer is in the center, and fuel (e.g. H_2 , CH_4) surrounds it [8]. This design results in: (i) input oxygen being completely consumed, (ii) large quantities of hydrogen and carbon-rich species being generated, and (iii) radially uniform scalar properties being established axially downstream. Ni, Cu-Ni (Ni 67% wt, Cu 33% wt), Inconel 600 (Ni 72% wt, Cr 16% wt, Fe 12% wt) and nitinol (Ni 55% wt, Ti 45% wt) are investigated as substrates.

Prior to any carbon-based synthesis, the metal substrates are reduced by operating the burner under a globally-rich hydrogen condition for 10min. Subsequently, CH₄ is introduced (with a global equivalence ratio of ~3) for 5 to 10min. The gas input ratio between CH₄ and H₂ is kept constant at 1:10. For a fixed substrate distance of 15mm above the flame, the temperature of the substrate is varied from 850°C to 500°C (by cooling), and is measured using both thermocouple and pyrometer. The reduction pre-treatment temperature is the same as the growth temperature. Although the flame temperature is kept constant, the type and concentrations of the hydrocarbon species at the substrate could differ for the two different surface temperatures. Thus, future work will involve measuring the species concentrations using laser-based diagnostics to explicitly determine the local growth conditions.

7.3 Results and Discussion

Raman spectroscopy identifies FLG [14], where the first order Raman spectra is comprised of the D, G, and 2D bands, which are located at shifts of ~1350 cm⁻¹, ~1580cm⁻¹, and ~2700cm⁻¹, respectively [15]. For Ni, the growth of FLG growth occurs at 850°C (Fig. 7.2a). Characterization using TEM corroborates the growth of FLG (Fig. 7.2b). At 850°C, no CNTs are grown on Ni for fixed flame conditions, as verified by FESEM (Fig. 7.2c). When the substrate temperature is lowered to 500°C, multi-wall carbon nanotubes (MWNTs) are observed, as shown in Fig. 2d. The direct growth of CNTs using bulk metals involves initial catalytic nanoparticle formation on the substrate followed by initiation and growth [11]. Nanoparticle formation on bulk metals can be due to carbide-induced breakup of the substrate or mechanical roughening. However, at

500°C the carbon solubility in Ni is minimal, hence nanoparticle formation likely occurs during the hydrogen flame reduction of the thin oxide layer on the Ni substrate. A critical parameter that determines the growth of graphene versus CNTs is related to the carbon solubility of the bulk metal. At high temperatures, carbon atoms are soluble in Ni [16]; and upon cooling, the carbon precipitates out to form FLG. In contrast, at low temperatures, hydrocarbon pyrolysis gases adsorb on the substrate, leading to the formation of CNTs [17].

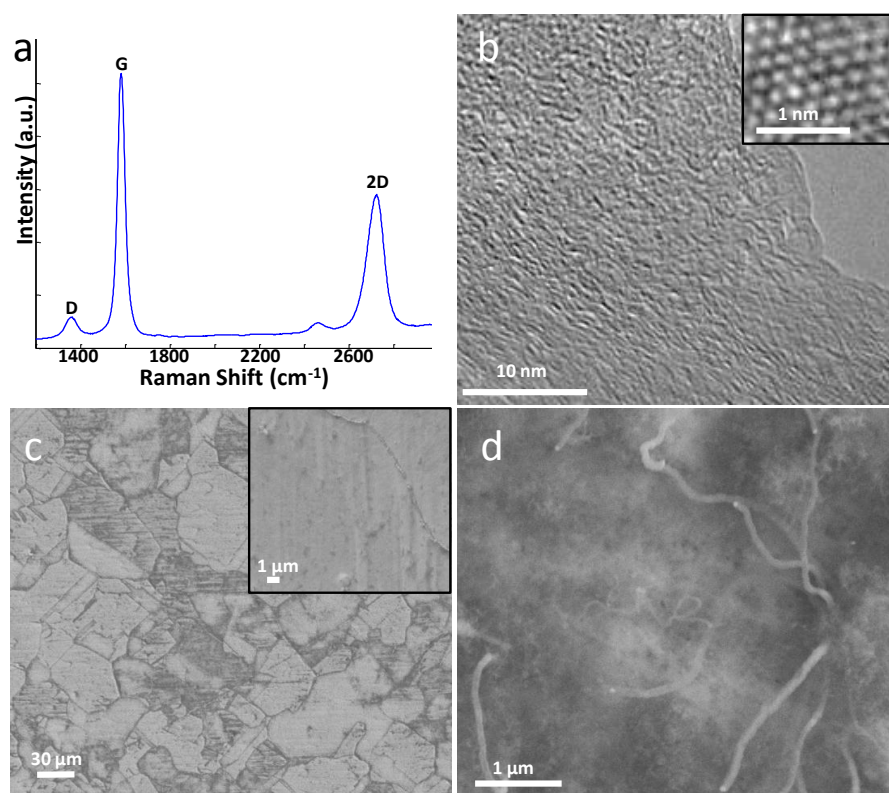


Figure 7.2 Carbon nanomaterial growth on Ni. (a) Raman spectrum of the few-layer graphene (FLG) synthesized on Ni at a temperature of 850°C. (b) HRTEM image of the FLG, the top right inset is magnified image of the graphene lattice. (c) SEM image of the FLG on Ni, the top right inset is a magnified image of Ni. No CNTs are observed. (d) CNTs grown on Ni at 500°C.

CVD growth of graphene on metals involves a high substrate temperature, which is necessary for hydrocarbon dissociation within the boundary layer. Lower temperature growth is important for industrial feasibility and economic cost. In our setup, combustion provides hydrocarbon dissociation such that post-flame gases are comprised of relevant carbon-rich pyrolysis species (such as CO and C_n); hence a high substrate temperature is not necessary for graphene growth. Figure 7.3 shows the Raman spectrum of the graphene growth on Ni at different temperatures. The growth of FLG is observed at 750°C and 600°C, without the presence of CNTs. At 600°C a higher D peak is observed, Fig. 7.3. The D peak is related to the disorder present in the graphene film and a larger disorder peak is typically encountered in the low temperature growth of graphene [18]. The growth of CNTs on Ni is only observed at temperatures starting at around 500°C, where a small 2D peak is observed within the Raman spectrum, Fig. 7.3.

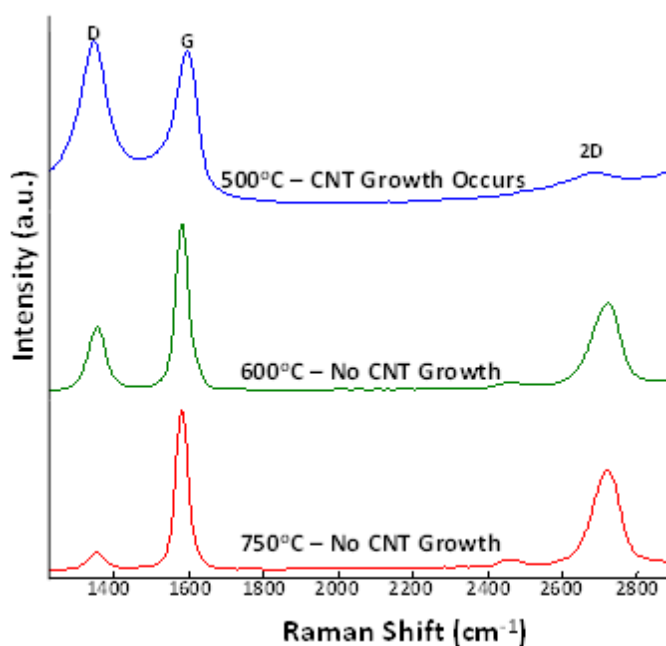


Figure 7.3 Raman spectrum showing the influence of temperature on the growth of FLG on Ni.

The carbon solubility of a metal plays a critical role in the growth of graphene. Copper due to its low carbon solubility is an ideal metal for limiting the growth of graphene layers [8]. Alloys such as Cu-Ni can adjust the overall carbon solubility, and hence are expected to be an important alloy in the optimization of graphene synthesis [13]. The Raman spectrum, [Fig. 7.4a](#), confirms the growth of FLG on Cu-Ni at a temperature of 850°C. The disorder (D) peak is higher for Cu-Ni as compared to Ni. Using the FESEM, [Fig. 7.4b](#), no CNTs are observed at this temperature. When the temperature of the Cu-Ni substrate is lowered to 600°C, the growth of CNTs occurs on the substrate, [Fig. 7.4c](#). Higher yields of CNTs occur at a temperature of 500°C for Cu-Ni, [Fig. 7.4d](#). Hydrogen etching results in the production of small Ni nanoparticles from Cu-Ni alloy; however this process does not readily occur on pure Ni [19]. Due to the formation of numerous Ni nanoparticles, a higher yield of CNTs occurring at a wider temperature range is observed on the Cu-Ni, when compared to pure Ni. A larger concentration of nanoparticles seems to occur at the grain boundaries, as large quantities of CNTs are visible near the grain boundaries, [Fig. 7.4c](#). No growth of CNTs occurs at 850°C on Cu-Ni, as it is possible the high temperature increases the pyrolytic process on the substrate and hydrocarbons adsorb too fast to be incorporated as CNTs [17]. Additionally, carbon atoms are soluble within Ni at 850°C that results in the formation of FLG upon cooling.

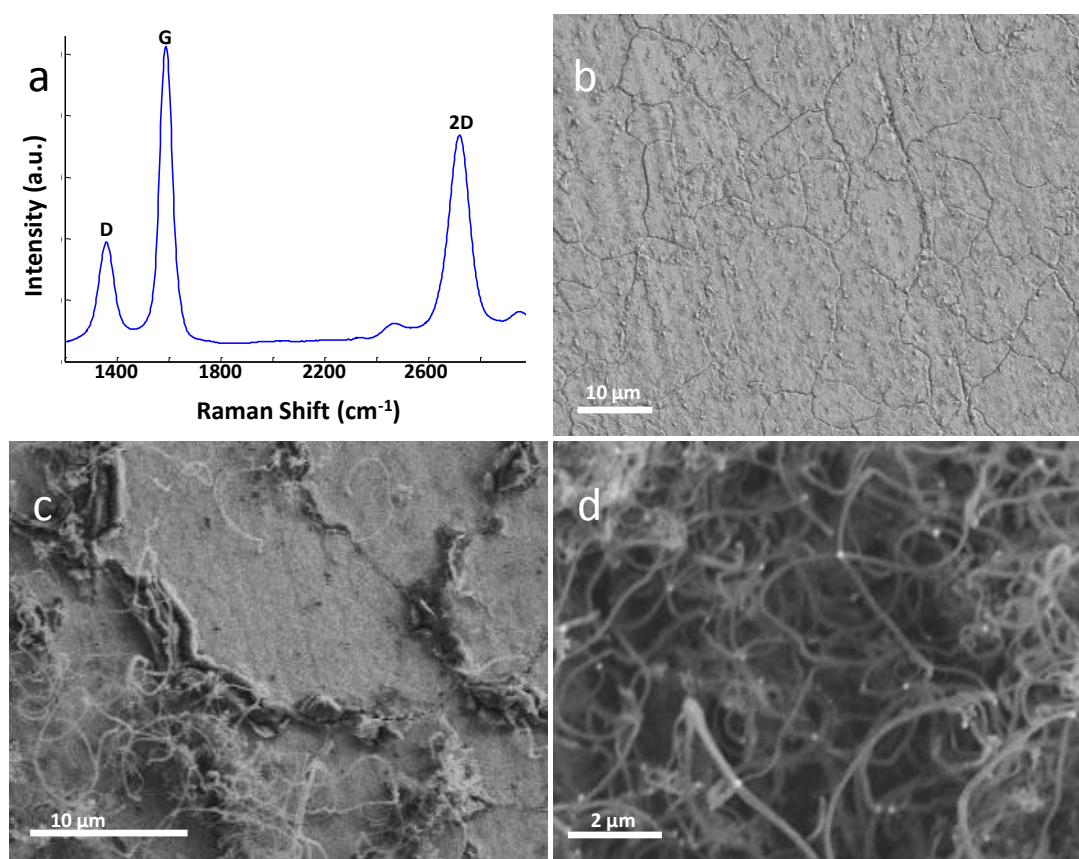


Figure 7.4 Carbon nanomaterial growth on Cu-Ni. (a) Raman spectrum of the few-layer graphene (FLG) synthesized on Cu-Ni at a temperature of 850°C. (b) SEM image of the FLG on Cu-Ni. No CNTs are observed. (c) CNTs grown on Cu-Ni at 600°C. (d) CNTs grown on Cu-Ni at 500°C.

Next the transitional growth between graphene and CNTs is investigated on Inconel and nitinol. At a temperature of 850°C the growth of FLG is observed on Inconel, [Fig 7.5a](#). The exclusive growth of FLG is not observed on nitinol for the examined experimental conditions. Although carbon is highly soluble within Ni-Ti [20], TiC_{1-x} readily forms [12], which can break up the substrate surface. This results in a disorder structure at a temperature of 850°C, [Fig 7.5b](#). When the temperature is lowered to 500°C, the growth of CNTs is verified on Inconel and nitinol using FESEM, [Figs. 7.5c and 7.5d](#), respectively. The yield of CNTs as assessed from the FESEM, is noticeably

lower on the pure Ni substrate (Fig. 7.2d) as compared to the Inconel and nitinol substrate (Figs. 7.5c and 7.5d). Such results match those from prior flame synthesis studies, albeit in different flame configurations, where alloys of Ni/Cr/Fe and Ni/Ti [9,10] result in the optimal growth of CNTs. The diameter of CNTs observed on Ni, Cu-Ni, Inconel, and nitinol is between 50 to 100 nm. H_2 is known to etch sp^2 bonded carbon atoms, and a high H_2 to CH_4 ratio for the feed gas leads to defective and large diameter CNTs [21]. Additionally, H_2 can etch away smaller diameter CNTs. Controlled experiments on Inconel and nitinol, where no hydrogen was added to the fuel, reduced etching of sp^2 bonded carbon atoms, producing CNTs that are more uniform and of smaller diameter, less than 50 nm (Figs. 7.5e and 7.5f).

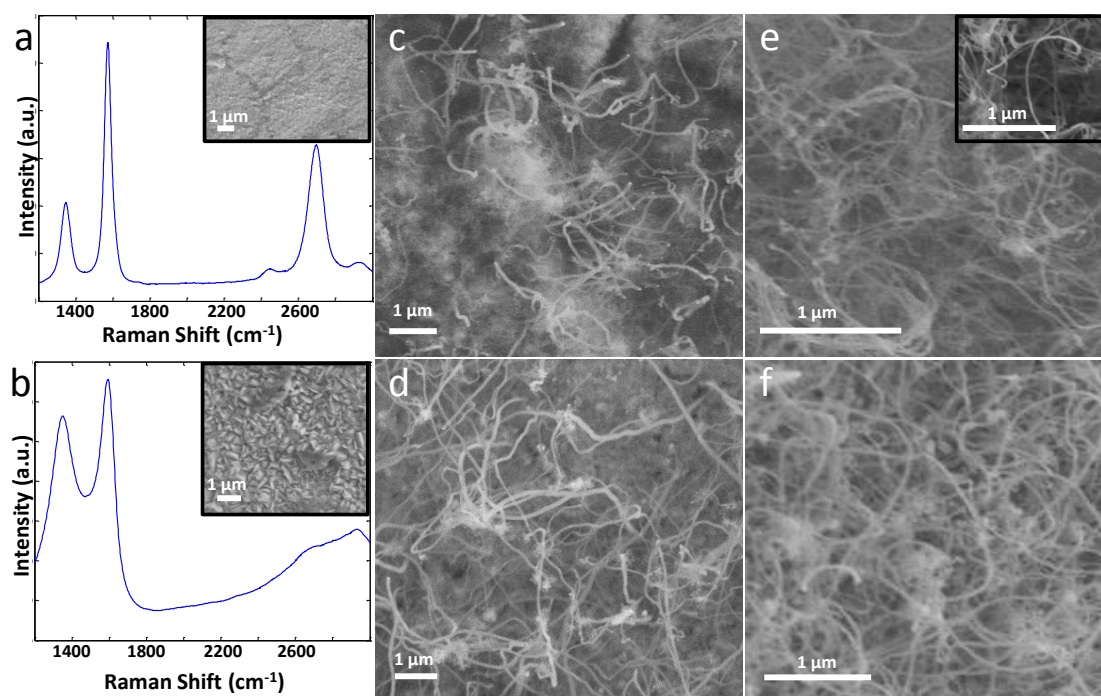


Figure 7.5 Carbon nanomaterial growth on Inconel and nitinol. (a) Raman spectrum of the few-layer graphene (FLG) synthesized on Inconel at a temperature of 850°C. The top right inset is the SEM image of the FLG on Inconel. (b) Raman spectrum of the growth on nitinol at a temperature of 850°C. The top right inset is the SEM image showing the disorder structure on nitinol. (c) CNTs grown on Inconel at 500°C. (d) CNTs grown on nitinol at 500°C. (e) CNTs grown on Inconel without the addition of hydrogen as fuel. (f) CNTs grown on nitinol without the addition of hydrogen as fuel.

7.4 Concluding Remarks

The importance of Ni alloys and temperature on the flame synthesis of carbon nanomaterials is highlighted. At a substrate temperature of 500°C, the growth of CNTs is observed on Ni, Cu-Ni, Inconel, and nitinol. When the substrate temperature is increased to 850°C, growth can transition from CNTs to FLG on Ni, Cu-Ni and Inconel. The advantages of our process are tunability to produce graphene and CNTs; synthesis at atmospheric conditions without a confining chamber; continuous rapid growth process (minutes versus hours); and efficient and economical use of CH₄ and H₂ in providing the elevated temperature and species necessary for growth.

7.5 References

- [1] Geim AK, Novoselov KS. The rise of graphene. *Nat Mater* 2007;6:183-91.
- [2] Baughman RH, Zakhidov AA, de Heer WA. Carbon Nanotubes--the Route Toward Applications. *Science* 2002;297:787-92.
- [3] Li X, Cai W, An J, Kim S, Nah J, Yang D et al. Large-Area Synthesis of High-Quality and Uniform Graphene Films on Copper Foils. *Science* 2009;324:1312-4.
- [4] Kim KS, Zhao Y, Jang H, Lee SY, Kim JM, Kim KS et al. Large-scale pattern growth of graphene films for stretchable transparent electrodes. *Nature* 2009;457:706-10.
- [5] Yao Y, Li Z, Lin Z, Moon K, Agar J, Wong C. Controlled Growth of Multilayer, Few-Layer, and Single-Layer Graphene on Metal Substrates. *J Phys Chem C* 2011;115:5232-8.
- [6] Liu N, Fu L, Dai B, Yan K, Liu X, Zhao R et al. Universal Segregation Growth Approach to Wafer-Size Graphene from Non-Noble Metals. *Nano Lett* 2011;11:297-303.
- [7] Tanemura M, Iwata K, Takahashi K, Fujimoto Y, Okuyama F, Sugie H et al. Growth of aligned carbon nanotubes by plasma-enhanced chemical vapor deposition: Optimization of growth parameters. *J Appl Phys* 2001;90:1529.
- [8] Memon NK, Tse SD, Al-Sharab JF, Yamaguchi H, Goncalves AB, Kear BH et al. Flame synthesis of graphene films in open environments. *Carbon* 2011;49:5064-70.
- [9] Xu F, Liu X, Tse SD. Synthesis of carbon nanotubes on metal alloy substrates with voltage bias in methane inverse diffusion flames. *Carbon* 2006;44:570-7.
- [10] Xu F, Zhao H, Tse SD. Carbon nanotube synthesis on catalytic metal alloys in methane/air counterflow diffusion flames. *Proceedings of the Combustion Institute* 2007;31:1839-47.
- [11] Merchan-Merchan W, Saveliev AV, Kennedy L, Jimenez WC. Combustion synthesis of carbon nanotubes and related nanostructures. *Progress in Energy and Combustion Science* 2010;36:696-727.
- [12] Sato S, Kawabata A, Kondo D, Nihei M, Awano Y. Carbon nanotube growth from titanium-cobalt bimetallic particles as a catalyst. *Chemical Physics Letters* 2005;402:149-54.

- [13] Chen S, Cai W, Piner RD, Suk JW, Wu Y, Ren Y et al. Synthesis and Characterization of Large-Area Graphene and Graphite Films on Commercial Cu–Ni Alloy Foils. *Nano Lett* 2011;11:3519-25.
- [14] Reina A, Jia X, Ho J, Nezich D, Son H, Bulovic V et al. Large Area, Few-Layer Graphene Films on Arbitrary Substrates by Chemical Vapor Deposition. *Nano Lett* 2009;9:30-5.
- [15] Ferrari AC, Meyer JC, Scardaci V, Casiraghi C, Lazzeri M, Mauri F et al. Raman Spectrum of Graphene and Graphene Layers. *Phys Rev Lett* 2006;97:187401.
- [16] Mattevi C, Kim H, Chhowalla M. A review of chemical vapour deposition of graphene on copper. *J Mater Chem* 2011;21:3324-34.
- [17] Seidel R, Duesberg GS, Unger E, Graham AP, Liebau M, Kreupl F. Chemical Vapor Deposition Growth of Single-Walled Carbon Nanotubes at 600 °C and a Simple Growth Model. *J Phys Chem B* 2004;108:1888-93.
- [18] Yuan GD, Zhang WJ, Yang Y, Tang YB, Li YQ, Wang JX et al. Graphene sheets via microwave chemical vapor deposition. *Chemical Physics Letters* 2009;467:361-4.
- [19] Miao HY, Lue JT, Chen SY, Chen SK, Ouyang MS. Growth of carbon nanotubes on transition metal alloys by microwave-enhanced hot-filament deposition. *Thin Solid Films* 2005;484:58-63.
- [20] DU Y, C. S. Experimental investigation and thermodynamic modeling of the Ni-Ti-C system. 1998;89.
- [21] Behr MJ, Gaulding EA, Mkhoyan KA, Aydil ES. Effect of hydrogen on catalyst nanoparticles in carbon nanotube growth. *J Appl Phys* 2010;108:053303.

\

Chapter 8

8. Synthesis of CNTs and Graphene Films using Metal-Oxide Spinel

8.1 Introduction

Nano-sized metal oxides are a promising material for enhancing the rate capability of electrodes, however due to particle agglomeration and low electrical conductivity their use has resulted in very limited improvement in the rate capability [1]. Composite materials, involving metal oxides and nano-carbon (graphene or CNTs), can improve electrical conductivity and reduce particle agglomeration. Hence such materials can significantly improve the performance of various electrodes [2]. The use of solid oxide solutions containing transition metal ions (spinel) can enable the scalable growth of CNTs and graphene on arbitrary substrates. Strategically selected metal oxides, such as $\text{Mg}_{1-x}\text{Co}_x\text{O}$, can be easily removed from the substrate by a mild non-oxidative washing with aqueous HCl [3,4]. This can enable the direct growth of graphene on an insulating surface, which has been a major focus of the CVD community [5]. Other applications include hot pressing the CNT (or graphene) and spinel composite into larger massive composites [6].

As a precursor to catalytic CNT growth with CVD, spinels subjected to high temperature reduction, resulting in the formation of metal catalysts. Peigney's group [7-13] has successfully produced CNTs (high purity SWNT bundles) and CNTs/metal-oxide nanocomposites using CVD with H_2 and CH_4 as the precursor. Additionally, the group has extensively investigated the effects of various solid solutions on the growth of CNTs

and nanocomposites. Some of the drawbacks of this CVD method include a long processing time (reaching 4 hours [11]), cumbersome batch processing, and the sizable consumption of both H_2/CH_4 gas and electrical energy.

The growth of a composite material involving spinels and reduced graphene oxide has been reported using a solution synthesis method [2,14]. However, graphene oxide does not exhibit the unique properties of graphene [15]. To the best of our knowledge, composite materials involving the synthesis of spinels and graphene has yet to be reported. Additionally, flame synthesis of CNTs using spinels has yet to be demonstrated. In this study, the catalytic synthesis of CNTs and graphene using metal oxide solutions of Cobalt Aluminate ($CoAl_2O_4$), Nickel Aluminate ($NiAl_2O_4$), Zinc Ferrite ($ZnFe_2O_4$), and Copper Ferrite ($CuFe_2O_4$) is demonstrated using a counter flow diffusion flame (CDF) and a multiple inverse-diffusion flame. The CDF was first used for the production of various oxide nanomaterials such as Al_2O_3 , SiO_2 , and GeO_2 [16,17], and more recently, the CDF burner has commonly been used for the growth of CNTs [18] along with other nanomaterials [19,20]. Our group [21] has previously demonstrated the growth of CNTs using a CDF burner on various metal alloys (i.e., Fe, Fe/Cr, Ni/Cu, Ni/Ti, Ni/Cr, and Ni/Cr/Fe). It was shown that the alloy composition strongly impacts the growth of CNTs, along with gas-phase temperature, and local C_2H_2 concentration. Merchan-Merchan and co-workers [22,23] also demonstrated the growth of CNTs using the CDF burner on a Ni alloy probe. Their study investigates the flame parameters and the application of an external electric field on the growth of CNTs. Li et al. [24] investigated the growth of CNTs using the CDF burner on a Ni alloy probe and a Si substrate coated with porous anodic aluminum oxide. The flame profile of a CDF burner is well understood by the

combustion community and is well-suited for the fundamental investigation of nanomaterial synthesis. Hence, the CDF flame is used to study the influence of different metal oxide solutions on the growth of CNTs. A limitation of the CDF flame is the inability to grow CNTs across large regions due to the temperature and concentration gradients. Additionally, the growth typically occurs on a wire probe, as any large substrate would impact the flow structure of the CDF flame. For scalable growth of CNTs on metal-oxide spinels, the multiple inverse-diffusion flame is employed, where the burner operates in a novel inverse mode. Recently we reported the growth of CNTs and few-layer graphene (FLG) films using this burner in an open environment [25]. In the setup, for each individual flame, the oxidizer is in the center and the fuel (H_2 , CH_4) surrounds it. This enables the generation of large quantities of hydrogen and carbon-rich species, the complete consumption of oxygen, and the formation of radially uniform scalar properties (e.g. temperature, carbon species). Graphene synthesis normally occurs on large substrates, for this reason we only use the multiple-inverse diffusion flame for graphene growth on spinels. Additionally, the multiple-diffusion-flame readily provides the large quantities of hydrogen, which is necessary for the synthesis of graphene.

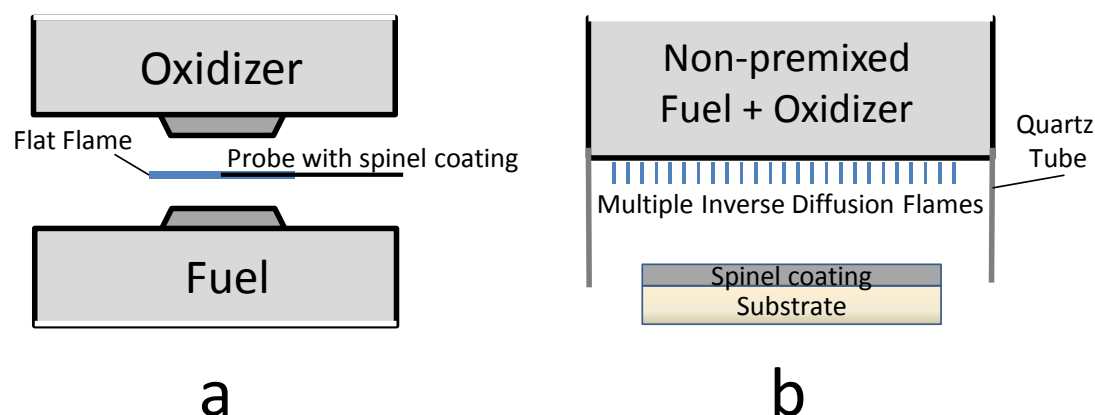


Figure 8.1 Schematic of the experimental setup (a) Counterflow diffusion flame (CDF) with a probe inserted for CNT growth. (b) Product species of multiple inverse-diffusion flames impinge on a substrate for CNT or graphene growth.

8.2 Experiment

8.2.1 Spinel preparation

All spinel powders are prepared by a co-precipitation process that is different from the combustion route used by Peigney's group.

8.2.1.1 Cobalt aluminate (CoAl_2O_4)

While maintaining a pH of 10.0 with dilute ammonia, an aqueous mixture of 1:2 $\text{CoSO}_4 \cdot 7\text{H}_2\text{O}$ and $\text{Al}(\text{NO}_3)_3 \cdot 9\text{H}_2\text{O}$ is titrated into an alkali solution. The resulting suspension is allowed to stir for 12 hours, after which the precipitates (a mixture of cobalt hydroxide and aluminum hydroxide) are separated from the solution with a wet filter, and washed with de-ionized water and ethyl alcohol. After drying at 70°C overnight, the samples are heated for 1 hour at 950°C in a hot air oven and the CoAl_2O_4 product is ground to a fine powder with a pestle and mortar.

8.2.1.2 Nickel aluminate (NiAl_2O_4)

Using $\text{Ni}(\text{NO}_3)_2 \cdot 6\text{H}_2\text{O}$ as the starting reagent, NiAl_2O_4 powders are obtained with much the same approach as CoAl_2O_4 , with the exception that final annealing temperature is 900°C .

8.2.1.3 Zinc ferrite (ZnFe_2O_4)

The preparation is again identical to that used for CoAl_2O_4 , but the starting reagents are ZnCl_2 and $\text{FeSO}_4 \cdot 7\text{H}_2\text{O}$ and the annealing process takes place at 1000°C .

8.2.1.4 Copper Ferrite (CuFe_2O_4)

The production of CuFe_2O_4 is similar to the co-precipitation process described elsewhere [26]. A mixture of $\text{Cu}(\text{NO}_3)_2 \cdot 3\text{H}_2\text{O}$ and $\text{Fe}(\text{NO}_3)_3 \cdot 9\text{H}_2\text{O}$ in a 1:20 ratio is dissolved in de-ionized water (50 ml) and titrated with 37.5 ml of 4M NaOH at 90°C . The solution is allowed to age at 90°C for 2 hours, and following wet filtration, the precipitate is dried overnight at 80°C . Finally the sample is heated in air at 600°C for 4 hours.

8.2.2 Spinel coating onto the support substrates

The as-prepared spinel powders are put into ethanol with a weight ratio of 20% spinel, and ultrasonicated for 20 minutes to form homogeneous suspension. For CNT growth using the CDF, the CoAl_2O_4 , NiAl_2O_4 , or ZnFe_2O_4 suspension is dropped onto the surface of a spatula-shaped copper substrate with a dimension of 0.8mm wide and 0.2mm thick (at the flat end). For CNT growth using the multiple inverse-diffusion flame, the CoAl_2O_4 , NiAl_2O_4 , or ZnFe_2O_4 suspension is dropped onto a $25\mu\text{m}$ thick Cu foil or 1.5mm thick quartz substrate. For graphene growth using the multiple inverse-diffusion

flame, the CuFe_2O_4 suspension is dropped onto a 1.5mm thick quartz substrate. In all cases the substrates are ready to use after being dried in air.

8.2.3 Flame setup

8.2.3.1 Counter flow diffusion flame (CDF)

The CDF utilized in this work is the same setup that was used for the synthesis of CNTs using a metal probe [21] and tungsten oxide nanowires [19]. The burner consists of two convergent nozzles, [Fig. 8.1a](#), with a 15-mm separation distance. Air acts as an oxidizer, entering from the top burner and a nitrogen (N_2) diluted fuel (CH_4) flows from the bottom burner, thus establishing a flat flame. The ratio between $\text{N}_2:\text{CH}_4$ is held constant at 1:1. A spinel-coated copper substrate is inserted into the hydrocarbon-rich fuel side of the flow field by mounting the substrate to a linear translation stage. After dwelling there for 10 minutes, the substrate is removed.

8.2.3.2 Multiple-inverse diffusion flame

The same multiple-inverse diffusion flame, [Fig. 8.1b](#), has been employed for the scalable growth of FLG using Cu or Ni and CNTs using Ni/Ti [25]. Graphene growth is examined on a Cu foil and CuFe_2O_4 covered quartz substrate. Prior to synthesis the substrates are reduced by operating the burner with hydrogen as the sole fuel for 10 min. Afterwards, CH_4 is introduced (with a “global” equivalence ratio of ~ 3) for 10 min. The input fuel ratio for CH_4 and H_2 is maintained at 1:10. The substrate is held at a fixed position from the burner and the temperature is measured using a thermocouple and pyrometer. The growth temperature for FLG is 950°C . For CNT synthesis on CoAl_2O_4 , NiAl_2O_4 , or

ZnFe_2O_4 either methane or ethylene is used as the fuel with minimal hydrogen. The substrate temperature is held between 500°C to 750°C .

8.2.4 Characterizations of the spinels, as-grown CNTs and FLG

The as-prepared spinels are studied by X-ray diffraction (XRD) using $\text{Cu-K}\alpha$ radiation ($\lambda=0.15418\text{nm}$), and the as-grown CNTs are investigated directly using scanning electron microscopy (FESEM) to assess CNT morphology. After ultrasonic treatment, low magnification transmission electron microscopy (TEM) and high resolution TEM (HRTEM) characterize the individual CNT and bundles. The graphene films are characterized using Raman spectroscopy (laser excitation 514.5 nm), X-ray photoelectron spectroscopy (XPS), and FESEM.

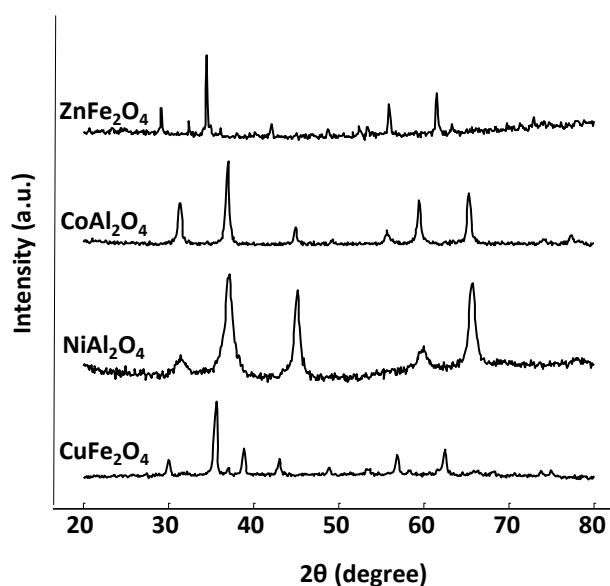


Figure 8.2 XRD patterns of as-prepared spinel solid solutions

8.3 Results and Discussion

8.3.1 XRD analysis of as-prepared spinels

The as-prepared spinel solid solution powders are analyzed by XRD, and their patterns are shown in Fig. 8.2. For CoAl_2O_4 , all peaks correspond to cobalt aluminate without impurities. Although all the peaks are accounted for the NiAl_2O_4 phase in the nickel aluminate solution, they are a bit wider than the CoAl_2O_4 peaks reflecting a smaller crystallization size and a poorer crystallization level [11]. For zinc ferrite, the peaks are attributed to the ZnFe_2O_4 phase, where the peaks are the sharpest, showing a better crystallization level when compared to CoAl_2O_4 or NiAl_2O_4 . The XRD result of CuFe_2O_4 is similar to that of ZnFe_2O_4 .

8.3.2 CNT Synthesis

Three spinel solid solutions, NiAl_2O_4 , CoAl_2O_4 , and ZnFe_2O_4 , are investigated for the growth of CNTs. The catalyst nanoparticles (Ni, Co, and Fe) form by reducing the spinel in an H_2 environment. The catalytic nanoparticles can either form on the interior of the reduced grain, where they will remain inactive, or attach to the surface of the reduced grain where CNT growth primarily occurs [27]. Carbon precursors present in the flame (CH_4 , CO, and C_2H_2), readily undergo dissociative adsorption on the surface of the catalytic nanoparticles and diffuse to grow into CNTs [28]. The nanoparticles either remain attached to the surface of the substrate and the base of the CNTs, or detached from the substrate surface and situated at the tip of the CNTs.

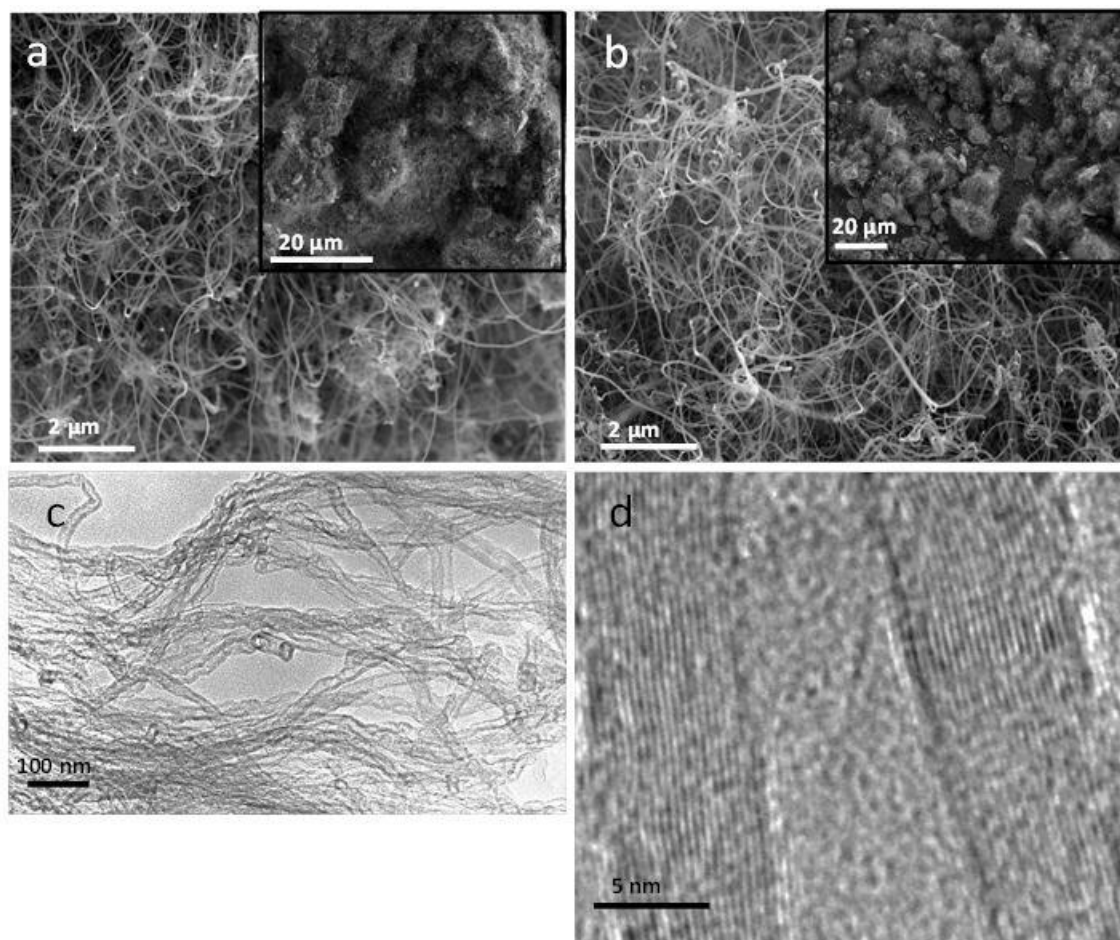


Figure 8.3 CNT growth using NiAl_2O_4 and CoAl_2O_4 . (a) High magnification FESEM image of CNTs covering a single reduced NiAl_2O_4 grain. The top right inset shows a low magnification image of CNTs from NiAl_2O_4 . (b) High magnification FESEM image of CNTs covering a single reduced CoAl_2O_4 grain. The top right inset shows a low magnification image of CNTs from CoAl_2O_4 . (c) TEM image of CNTs from NiAl_2O_4 . (d) HRTEM image of a CNT from NiAl_2O_4 (adapted from [29]).

Figures 8.3a and 8.3b show the typical FESEM images of CNTs grown from NiAl_2O_4 and CoAl_2O_4 using the CDF. Figure 8.3a depicts the growth of CNTs from a single grain of NiAl_2O_4 . The grain is uniformly and densely covered with CNTs, which have an outer diameter range of 20-50 nm and a length of more than 10 μm . From the inset in Fig. 8.3a, it is observed that all reduced grains are covered with densely packed CNTs. A similar growth pattern occurs for CoAl_2O_4 , Fig. 8.3b. From detailed FESEM observations, the overall yield of CNTs from NiAl_2O_4 is a bit higher when compared to CoAl_2O_4 . The higher yield of CNTs on NiAl_2O_4 is possibly due to the poorer crystallization level of the nickel aluminate solution (as observed from XRD). Since CNT growth occurs due to metal particles that are present on the surface of the reduced grain, the obtainability of active particles is related to the surface area of the grain. Poorly crystallized oxide solid solutions [11] have a higher specific surface area, thus a higher concentration of Ni nanoparticles form on the surface of the reduced grain, resulting in an increased CNT yield. The detailed structure of the as-grown CNTs is studied by performing TEM. Figure 8.3a shows several CNTs grown from NiAl_2O_4 , whose diameters spread from ~20 to 40nm. A HRTEM in Fig. 8.3d shows that the graphitic walls of the CNTs are of high quality and parallel to each other.

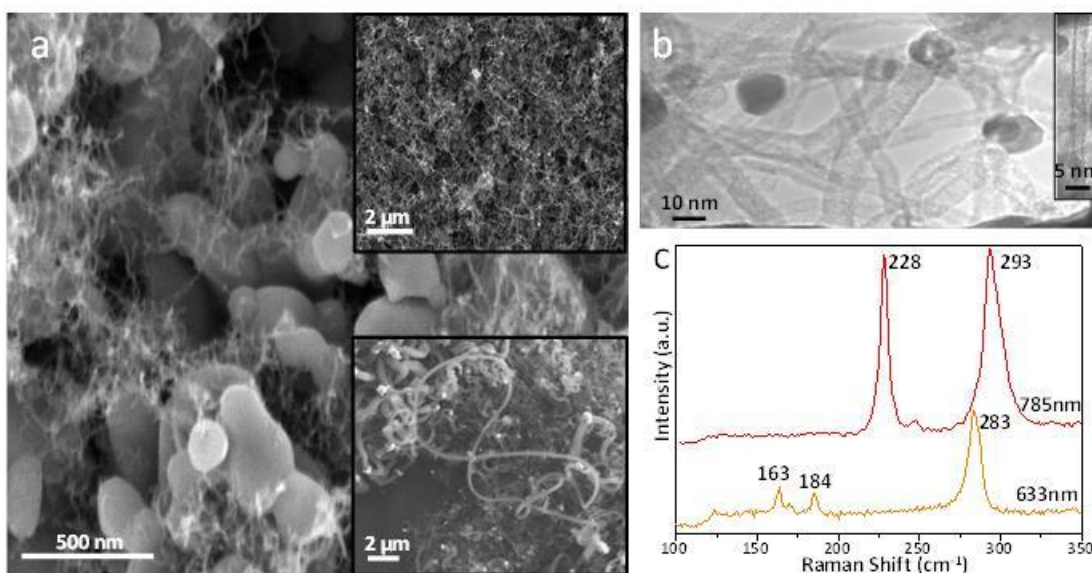


Figure 8.4 CNT growth using ZnFe₂O₄. (a) High magnification FESEM image of CNTs covering reduced ZnFe₂O₄ grains. The top right inset shows a low magnification image. The bottom right inset shows larger diameter CNTs prepared from poorly crystallized ZnFe₂O₄. (b) TEM images of CNTs from ZnFe₂O₄. The right inset is a HRTEM image of a CNT. (c) Raman spectra of as-grown CNTs from ZnFe₂O₄ (adapted from [29]).

CNTs synthesized from ZnFe₂O₄ are a mixture of MWNTs and SWNTs, [Fig. 8.4](#). Comparing the FESEM images from the growth of NiAl₂O₄ and CoAl₂O₄, it can be seen that the CNTs synthesized from ZnFe₂O₄ ([Fig. 8.4a](#)) are much thinner, with a diameter less than 15nm, and also shorter with a typical length of 2μm. From HRTEM observation, [Fig. 8.4b](#), the growth of SWNTs range in diameter from 3nm to 10nm. The presence of SWNTs is also confirmed by evaluating the as-grown CNTs using Raman Spectroscopy, excited at two laser wavelengths: 633nm and 785nm. From [Fig. 8.4c](#), the Radial Breathing Modes (RBM) frequencies are collected, corresponding to the two excitations. Using the RBM, the following values are calculated for the SWNT diameters, 0.87nm, 1.34nm, 1.52nm, 0.84nm, and 1.08nm [30,31]. These values

correspond to the following RBM peak positions (λ , cm^{-1}) 283, 184, 163 (from the 633nm excitation), 293 and 228 (from the 785nm excitation), respectively. The small diameter CNTs could possibly be a result of the well-crystallized level of the zinc ferrite solution, as pointed out in XRD patterns. The well crystallized solid solution has a low specific surface area, hence favoring the formation of metal particles of smaller size [11]. This results in a low yield of CNTs, where the average diameter is smaller.

The crystallinity of the zinc ferrite solution is modified by lowering the annealing temperature from 950°C to 600°C. XRD confirms that this modification lowers the crystallization level of the spinel. The bottom right inset in [Fig. 8.4a](#) depicts the CNTs synthesized from the poorly crystallized ZnFe_2O_4 spinel. CNTs are primarily comprised of MWNTs with a diameter ranging from 20 to 40 nm to greater than 200 nm. While poorly crystallized oxide solution can increase the yield of CNTs, as was observed when comparing the growth of NiAl_2O_4 and CoAl_2O_4 , similar results are not observed for ZnFe_2O_4 . The poorly crystallized ZnFe_2O_4 can have a very high specific surface area, which results in most of the metallic ions being located at or near the surface of the unreduced grains. After reduction to the metallic states, these particles coalesce at the surface of the reduced grain to form much larger particles [32]. Rather than increasing CNT yield, this leads to fewer CNTs of a larger average diameter. Moreover, upon heating in the CNT growth process, the recrystallization of the poorly crystallized solid solution provokes the entrapment of carbon within the reduced grain and deteriorates the mechanical property of any CNT containing composites [11]. Hence, the crystalline quality of the spinel solution plays a critical role in the growth of CNTs. Typically, well crystallized solutions result in SWNTs or MWNTs with a small diameter. The yield of

CNTs obtained from ZnFe_2O_4 is lower when compared to both NiAl_2O_4 and CoAl_2O_4 . For ZnFe_2O_4 , while zinc reduces fairly easily, Fe is slower and more difficult to reduce. Hence the formed Fe nanoparticles are less numerous, possibly resulting in a lower yield of CNTs.

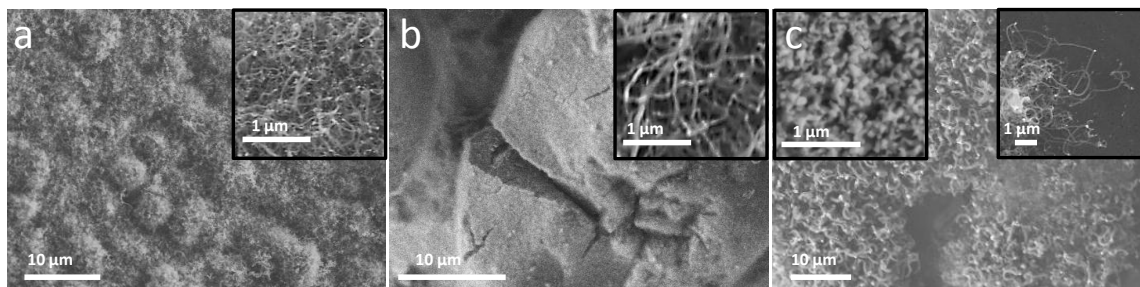


Figure 8.5 Growth of CNTs using the multiple inverse-diffusion flame. (a) Low magnification FESEM image on CoAl_2O_4 . The top right inset shows a high magnification image. (b) Low magnification FESEM image on NiAl_2O_4 . The top right inset shows a high magnification image. (c) Low magnification FESEM image on ZnFe_2O_4 . The top right inset shows a high magnification image. The top left inset shows the growth of no CNTs at a temperature of 500°C on ZnFe_2O_4 .

Because of the impact on the flow structure of the flame, a limitation of the CDF is an inability to synthesize materials on large substrates. Scalable growth of CNTs on arbitrary large substrates is demonstrated using the multiple inverse-diffusion flame, with similar results observed by coating either a quartz or copper substrate with the spinel solution. Figure 8.5 shows typical CNTs grown using CoAl_2O_4 , NiAl_2O_4 , and ZnFe_2O_4 . The temperature of the substrate is measured using a pyrometer and thermocouple. Optimal growth of CNTs using NiAl_2O_4 and CoAl_2O_4 occurs in the temperature range from 500°C to 750°C . However, for ZnFe_2O_4 no CNT growth is observed at a temperature of 500°C (top left inset in Fig. 8.5c). This result is consistent with the

findings of others, where the use of Fe in the catalytic growth of CNTs normally requires a higher temperature than equivalent growth with Ni or Co [33].

8.3.3 Graphene Synthesis

Graphene is typically synthesized on Cu foils at a growth temperature of 1000°C. Due to its low carbon solubility, Cu is the preferred metal for the growth of graphene [34]. A key difference in the optimal growth conditions between CNTs and graphene is the role of hydrogen. For graphene, a large partial pressure of hydrogen ensures the growth of graphene grains and etches away unwanted carbon bonded atoms [35]. However, a high partial pressure of hydrogen is not optimal for CNT growth, leading to defective and larger diameter CNTs [36]. For graphene synthesis, the CH₄:H₂ ratio is held constant at 1:10. Another difference is the growth temperature, the optimal temperature for CNT growth is 750°C, while for graphene, the substrate temperature is held at 950°C. In order to precisely control conditions over the entire substrate, the growth of graphene on CuFe₂O₄ is investigated using the multiple inverse-diffusion flame setup and the results are compared with the growth of graphene directly on Cu [25]. The CuFe₂O₄ solution is coated directly on quartz, which eliminates the influence of the underlying transitional metal on the growth of graphene.

Raman spectroscopy is commonly used in the identification of graphene and FLG [37,38]. Three peaks are typically associated with single to few-layer graphene. A D peak at ~1350 cm⁻¹, which is associated with the first-order zone boundary and measures the defect in the graphene, a G peak at ~1580 cm⁻¹, which is caused by the C-C stretching mode of sp² bonded carbon atoms, and a 2D peak at ~2700cm⁻¹, which is related to the

second-order zone boundary phonons. The ratio between the intensity of the G peak (I_G) and the 2D peak (I_{2D}) is used to approximate the number of graphene layers. For single to bi-layer graphene, this ratio is less than 1 and greater than 1 for FLG. The I_G/I_{2D} ratio for the synthesis on Cu is 1.35, Fig. 8.6a, which is consistent with FLG. The results of the Raman spectrum are consistent with atomic force microscopy, and UV-vis spectroscopy, where 5 to 8 layers of graphene are grown uniformly on the substrate [25]. For graphene film synthesized on CuFe_2O_4 , $I_G/I_{2D} = 1.23$, Fig. 8.6a, indicating FLG similar to that of Cu. The intensity ratio between the D peak (I_D) and I_G is used as a measure for the disorder present in the graphene, which arises from domain boundaries, edges, wrinkles, impurities, and other factors. The domain size of the graphene film can be calculated using the following equation [39].

$$\text{Eq. 1: } I_D/I_G = C(\lambda) / L_a,$$

where L_a [nm] is the domain size, λ [nm] wavelength of the incident light, and $C(\lambda)$ is calculated as $2.4 \times 10^{-10} \times \lambda^4$. The typical domain size of graphene on Cu and CuFe_2O_4 is ~45nm and ~12nm, respectively. The smaller domain on CuFe_2O_4 is possibly due to the crystalline structure of the spinel.

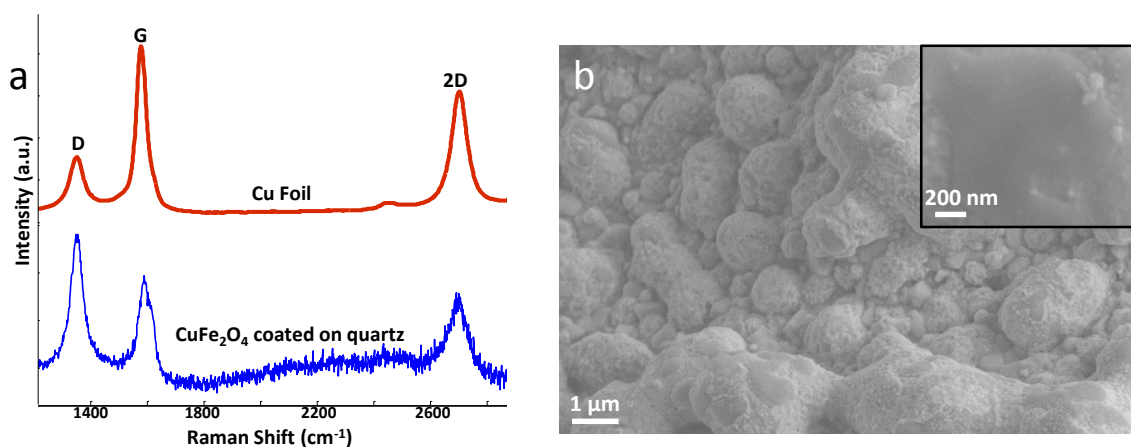


Figure 8.6 Growth of graphene using the multiple inverse-diffusion flame. (a) Raman spectrum of few-layer graphene (FLG) on Cu and CuFe₂O₄ coated on quartz. (b) FESEM image of the CuFe₂O₄ coated with graphene. The top right inset is a high magnification image.

The quality of the graphene film on CuFe₂O₄ is assessed using X-ray photoelectron spectroscopy (XPS) spectrum of the C 1s speak and the results are compared with the growth of graphene on Cu, Fig. 8.7. For CuFe₂O₄, the main C 1s peak is at 284.2 eV, which indicates most of the atoms are in the sp² C state [40]. Other peaks indicate the presence of oxygen incorporation, which can be possible due to the structure of the copper ferrite spinel. Lower oxygen concentration is observed for the growth of graphene on Cu, where the oxygen concentration is even lower than CVD-grown graphene near vacuum conditions [41]. The carbon - oxygen bond for the graphene on CuFe₂O₄ is similar to that of CVD grown graphene, therefore it is postulated here that the abundance of H₂ in the post-flame species of the multiple inverse-diffusion flame, limits the oxidation of the graphene film.

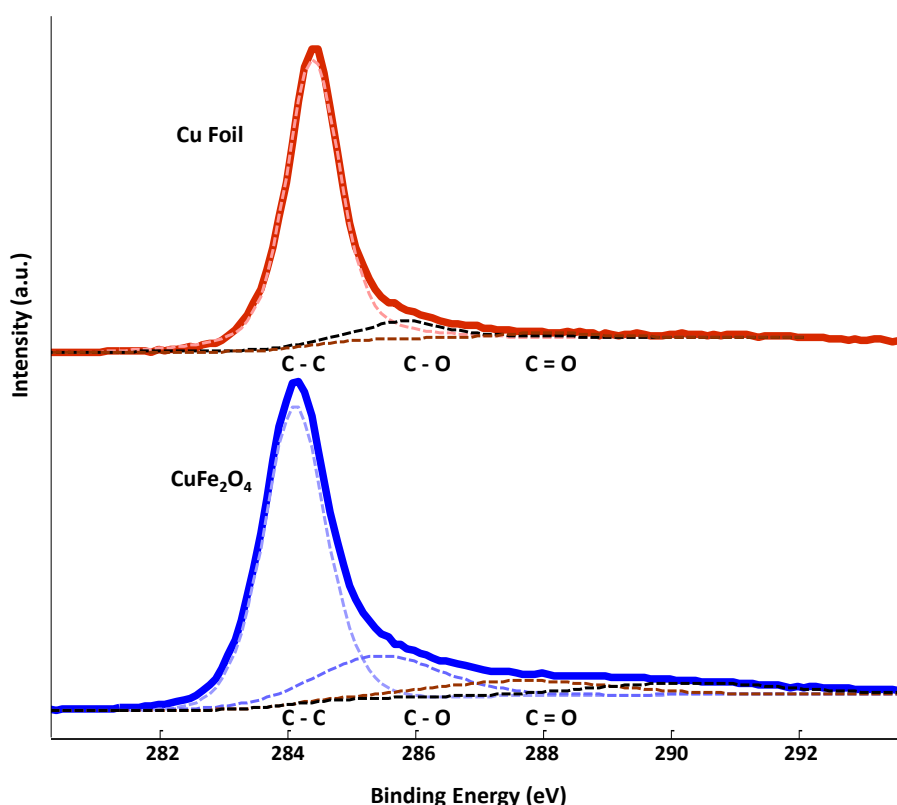


Figure 8.7 XPS C 1s spectrum of FLG synthesized using Cu foil and CuFe_2O_4 .

8.4 Concluding Remarks

MWNTs, SWNTs, and FLG are synthesized through the decomposition of carbon precursors (e.g. CH_4 , CO and C_2H_2) over nanoparticles (i.e. Cu, Ni, Co and Fe) prepared from reduced spinel solid solutions (i.e. NiAl_2O_4 , CoAl_2O_4 , ZnFe_2O_4 , CuFe_2O_4). The spinels are prepared by a co-precipitation method, and the production process of CNTs and FLG under atmospheric pressure is continuous and energy-efficient. CNT growth activities are investigated as functions of spinel solid solutions and substrate temperature using the CDF and multiple inverse-diffusion flame. MWNTs are observed on NiAl_2O_4 and CoAl_2O_4 , while a mixture of MWNTs and SWNTs are observed on ZnFe_2O_4 . The crystallinity of the spinel solution plays a critical role in the yield and size of the CNTs.

Low temperature growth of CNTs at 500°C occurs for NiAl_2O_4 and CoAl_2O_4 , whereas a high growth temperature of 750°C is required for ZnFe_2O_4 . The growth of graphene using the multiple inverse-diffusion flame occurs on CuFe_2O_4 at a temperature of 950°C. Raman spectroscopy confirms the growth of FLG on CuFe_2O_4 , which is similar to the growth of FLG on Cu foil. XPS confirms the limited oxidation of the FLG on CuFe_2O_4 . The as-grown CNTs/FLG and metal-oxide nanocomposites can be further used to prepare dense massive composites, for which the mechanical and electric properties would benefit greatly from the properties of the CNTs or FLG.

8.5 References

- [1] Arico AS, Bruce P, Scrosati B, Tarascon J, van Schalkwijk W. Nanostructured materials for advanced energy conversion and storage devices. *Nat Mater* 2005;4:366-77.
- [2] Bak S, Nam K, Lee C, Kim K, Jung H, Yang X et al. Spinel LiMn_2O_4 /reduced graphene oxide hybrid for high rate lithium ion batteries. *J Mater Chem* 2011;21.
- [3] Bacsa RR, Laurent C, Peigney A, Bacsa WS, Vaugien T, Rousset A. High specific surface area carbon nanotubes from catalytic chemical vapor deposition process. *Chemical Physics Letters* 2000;323:566-71.
- [4] Flahaut E, Laurent C, Peigney A. Catalytic CVD synthesis of double and triple-walled carbon nanotubes by the control of the catalyst preparation. *Carbon* 2005;43:375-83.
- [5] Ismach A, Druzgalski C, Penwell S, Schwartzberg A, Zheng M, Javey A et al. Direct Chemical Vapor Deposition of Graphene on Dielectric Surfaces. *Nano Lett* 2010;10:1542-8.
- [6] Laurent C, Peigney A, Dumortier O, Rousset A. Carbon nanotubes–Fe–Alumina nanocomposites. Part II: microstructure and mechanical properties of the hot-Pressed composites. *Journal of the European Ceramic Society* 1998;18:2005-13.
- [7] de Resende VG, De Grave E, Cordier A, Weibel A, Peigney A, Laurent C. Catalytic chemical vapor deposition synthesis of single- and double-walled carbon nanotubes from $\alpha\text{-(Al}_{1-x}\text{Fe}_x)_2\text{O}_3$ powders and self-supported foams. *Carbon* 2009;47:482-92.

- [8] Flahaut E, Peigney A, Laurent C, Rousset A. Synthesis of single-walled carbon nanotube-Co-MgO composite powders and extraction of the nanotubes. *J Mater Chem* 2000;10.
- [9] Flahaut E, Peigney A, Laurent C, Marlière C, Chastel F, Rousset A. Carbon nanotube-metal-oxide nanocomposites: microstructure, electrical conductivity and mechanical properties. *Acta Materialia* 2000;48:3803-12.
- [10] Landois P, Peigney A, Laurent C, Frin L, Datas L, Flahaut E. CCVD synthesis of carbon nanotubes with W/Co-MgO catalysts. *Carbon* 2009;47:789-94.
- [11] Laurent C, Peigney A, Rousset A. Synthesis of carbon nanotube-Fe-Al₂O₃ nanocomposite powders by selective reduction of different Al_{1.8}Fe_{0.2}O₃ solid solutions. *J Mater Chem* 1998;8.
- [12] Peigney A, Flahaut E, Laurent C, Chastel F, Rousset A. Aligned carbon nanotubes in ceramic-matrix nanocomposites prepared by high-temperature extrusion. *Chemical Physics Letters* 2002;352:20-5.
- [13] Peigney A, Coquay P, Flahaut E, Vandenberghe RE, De Grave E, Laurent C. A Study of the Formation of Single- and Double-Walled Carbon Nanotubes by a CVD Method. *J Phys Chem B* 2001;105:9699-710.
- [14] Wang H, Hu Z, Chang Y, Chen Y, Wu H, Zhang Z et al. Design and synthesis of NiCo₂O₄-reduced graphene oxide composites for high performance supercapacitors. *J Mater Chem* 2011;21.
- [15] Bonaccorso F, Sun Z, Hasan T, Ferrari AC. Graphene photonics and optoelectronics. *Nat Photon* 2010;4:611-22.
- [16] Chung S, Katz JL. The counterflow diffusion flame burner: A new tool for the study of the nucleation of refractory compounds. *Combust Flame* 1985;61:271-84.
- [17] Rosner DE. Flame Synthesis of Valuable Nanoparticles: Recent Progress/Current Needs in Areas of Rate Laws, Population Dynamics, and Characterization. *Ind Eng Chem Res* 2005;44:6045-55.
- [18] Merchan-Merchan W, Saveliev AV, Kennedy L, Jimenez WC. Combustion synthesis of carbon nanotubes and related nanostructures. *Progress in Energy and Combustion Science* 2010;36:696-727.
- [19] Xu F, Tse SD, Al-Sharab JF, Kear BH. Flame synthesis of aligned tungsten oxide nanowires. *Appl Phys Lett* 2006;88:243115-3.

- [20] Merchan-Merchan W, Saveliev AV, Jimenez WC, Salkar G. Flame synthesis of hybrid nanowires with carbon shells and tungsten-oxide cores. *Carbon* 2010;48:4510-8.
- [21] Xu F, Zhao H, Tse SD. Carbon nanotube synthesis on catalytic metal alloys in methane/air counterflow diffusion flames. *Proceedings of the Combustion Institute* 2007;31:1839-47.
- [22] Merchan-Merchan W, Saveliev AV, Kennedy LA. High-rate flame synthesis of vertically aligned carbon nanotubes using electric field control. *Carbon* 2004;42:599-608.
- [23] Saveliev AV, Merchan-Merchan W, Kennedy LA. Metal catalyzed synthesis of carbon nanostructures in an opposed flow methane oxygen flame. *Combust Flame* 2003;135:27-33.
- [24] Li TX, Zhang HG, Wang FJ, Chen Z, Saito K. Synthesis of carbon nanotubes on Ni-alloy and Si-substrates using counterflow methane-air diffusion flames. *Proceedings of the Combustion Institute* 2007;31:1849-56.
- [25] Memon NK, Tse SD, Al-Sharab JF, Yamaguchi H, Goncalves AB, Kear BH et al. Flame synthesis of graphene films in open environments. *Carbon* 2011;49:5064-70.
- [26] Tao S, Gao F, Liu X, Toft Sørensen O. Preparation and gas-sensing properties of CuFe₂O₄ at reduced temperature. *Materials Science and Engineering: B* 2000;77:172-6.
- [27] Bacsa RR, Laurent C, Peigney A, Vaugien T, Flahaut E, Bacsa WS et al. (Mg,Co)O Solid-Solution Precursors for the Large-Scale Synthesis of Carbon Nanotubes by Catalytic Chemical Vapor Deposition. *J Am Ceram Soc* 2002;85:2666-9.
- [28] Xu F, Liu X, Tse SD. Synthesis of carbon nanotubes on metal alloy substrates with voltage bias in methane inverse diffusion flames. *Carbon* 2006;44:570-7.
- [29] Xu F. Investigating flame-based synthesis of carbon nanotubes and metal-oxide nanowires. Rutgers University 2007.
- [30] Jorio A, Saito R, Hafner JH, Lieber CM, Hunter M, McClure T et al. Structural (n, m) Determination of Isolated Single-Wall Carbon Nanotubes by Resonant Raman Scattering. *Phys Rev Lett* 2001;86:1118-21.
- [31] Saito R, Dresselhaus G, Dresselhaus MS. Trigonal warping effect of carbon nanotubes. *Phys Rev B* 2000;61:2981-90.
- [32] Devaux X, Laurent C, Rousset A. Chemical synthesis of metal nanoparticles dispersed in alumina. *Nanostructured Materials* 1993;2:339-46.

- [33] Seidel R, Duesberg GS, Unger E, Graham AP, Liebau M, Kreupl F. Chemical Vapor Deposition Growth of Single-Walled Carbon Nanotubes at 600 °C and a Simple Growth Model. *J Phys Chem B* 2004;108:1888-93.
- [34] Mattevi C, Kim H, Chhowalla M. A review of chemical vapour deposition of graphene on copper. *J Mater Chem* 2011;21:3324-34.
- [35] Vlassiuk I, Regmi M, Fulvio P, Dai S, Datskos P, Eres G et al. Role of Hydrogen in Chemical Vapor Deposition Growth of Large Single-Crystal Graphene. *ACS Nano* 2011;5:6069-76.
- [36] Behr MJ, Gaulding EA, Mkhoyan KA, Aydil ES. Effect of hydrogen on catalyst nanoparticles in carbon nanotube growth. *J Appl Phys* 2010;108:053303.
- [37] Ferrari AC, Meyer JC, Scardaci V, Casiraghi C, Lazzeri M, Mauri F et al. Raman Spectrum of Graphene and Graphene Layers. *Phys Rev Lett* 2006;97:187401.
- [38] Reina A, Jia X, Ho J, Nezich D, Son H, Bulovic V et al. Large Area, Few-Layer Graphene Films on Arbitrary Substrates by Chemical Vapor Deposition. *Nano Letters* 2008; 2009;9:30-5.
- [39] Andrea C. F. Raman spectroscopy of graphene and graphite: Disorder, electron-phonon coupling, doping and nonadiabatic effects. *Solid State Commun* 2007;143:47-57.
- [40] D'Áz J, Paolicelli G, Ferrer S, Comin F. Separation of the sp^3 and sp^2 components in the C1s photoemission spectra of amorphous carbon films. *Phys Rev B* 1996;54:8064-9.
- [41] Bae S, Kim H, Lee Y, Xu X, Park J, Zheng Y et al. Roll-to-roll production of 30-inch graphene films for transparent electrodes. *Nat Nano* 2010;5:574-8.

Chapter 9

9. CNT and Iron Oxide Flame Synthesis on Stainless Steel

9.1 Introduction

Iron oxide nanoparticles exhibit numerous unique and interesting properties [1], which depend strongly on the chemical composition and morphology of the nanoparticle. The most common forms of iron oxides that occur in nature include magnetite (Fe_3O_4), maghemite ($\gamma\text{-Fe}_2\text{O}_3$), and hematite ($\alpha\text{-Fe}_2\text{O}_3$). These three oxide materials continue to play a critical role in the development of advanced functional devices [2]. While chemical vapor deposition is commonly used in the synthesis of iron oxide nanostructures [3], flames readily offer an oxidizing environment for the growth of oxide nanomaterials. The growth of Fe_3O_4 nanowires was previously demonstrated using a counterflow flame [4,5] and the growth of $\alpha\text{-Fe}_2\text{O}_3$ and $\gamma\text{-Fe}_2\text{O}_3$ nanowires was reported using a normal multiple diffusion-flame [6,7]. Fe_2O_3 growth occurs in a wide range of equivalence ratios, from 0.4 to 1.7, using the multiple diffusion-flames [6,7]. The growth of iron oxide can occur due the presence of O_2 , H_2O , CO_2 , and CO within the flame [5,7].

The growth of hybrid materials based on CNTs and metal oxides can be used in various applications such as supercapacitors, lithium batteries, electrochemical sensors, photocatalysts, solar cells, and gas sensors [8], [Table 9.1](#). Common methods for the production of such materials include sol-gel, hydrothermal synthesis, and thermal evaporation-deposition [8]. Supercapacitors based on CNTs/ Fe_2O_3 show promising charging-discharging properties, high specific capacitance and respectable cycle stability [9]. Multiple inverse-diffusion flames can provide both the carbon species (CH_4 , CO ,

C₂H₂) and oxygen species (H₂O, CO₂, and CO) required for the growth of CNTs and oxide materials, respectively. Iron based substrates have been successfully used for the synthesis of iron-oxide [6] and CNTs [10] using fuel-rich flames. However, it is not entirely clear what results in the production of CNTs versus iron-oxide and yet the simultaneous growth of both materials is yet to be demonstrated. Hence, the growth of CNTs and iron oxide is investigated on stainless steel using the multiple inverse-diffusion flame.

Application	Material	Role of CNTs	Role of oxides
Supercapacitors	RuO ₂ /CNTs MnO ₂ /CNTs Fe ₂ O ₃ /CNTs NiO/CNTs Co ₂ O ₃ /CNTs V ₂ O ₅ ·xH ₂ O/CNTs	As a conducting path and providing electrical double layer capacitance	Pseudocapacitance
Li ⁺ -battery	SnO ₂ /CNTs TiO ₂ /CNTs MnO ₂ /CNTs	As a conducting path and Li ⁺ storage	Li ⁺ storage
Electrochemical sensors	MnO ₂ /CNTs CuO/CNTs Cu ₂ O/CNTs RuO _x /CNTs ZrO ₂ /CNTs TiO ₂ /CNTs MoO _x /CNTs WO ₃ /CNTs RuO ₂ /CNTs	As a conducting path and a support	Electrocatalysis
Photocatalysts	TiO ₂ /CNTs ZnO/CNTs	As a support and an electron sink	Photocatalysis
Solar cell	TiO ₂ /CNTs	As a conducting path and an electron sink	Charge separation
Gas sensor	SnO ₂ /CNTs ZnO/CNTs	As a conducting path and adsorbent	Catalysis

Table 9.1 Applications, compositions and functions of CNTs-oxides hybrid materials [8].

9.2 Experiment

In the experimental setup, pyrolysis gases from the multiple inverse-diffusion flame impinge on a substrate, enabling the growth of iron oxide or carbon nanomaterials (see Fig. 9.1). The burner operates in an inverse mode, where for each distinct flame in the planar array, oxidizer is in the center, and fuel (e.g. H₂, CH₄) surrounds it. This design

results in radially uniform scalar properties being established axially downstream. Stainless steel 304 foils are investigated as the substrate. Prior to any synthesis, the metal substrate is reduced by operating the burner under globally-rich hydrogen conditions for 10min. Subsequently, CH₄ is introduced (with a global equivalence ratio of ~3) for 5 to 20 minutes. The gas input ratio between CH₄ and H₂ is kept constant at 1:10. For a fixed substrate distance of 15mm above the flame, the temperature of the substrate is held at either 850°C or 500°C (by cooling), and is measured using both thermocouple and pyrometer. [Figure 9.1](#) summarizes the experimental conditions along with the nanomaterial obtained.

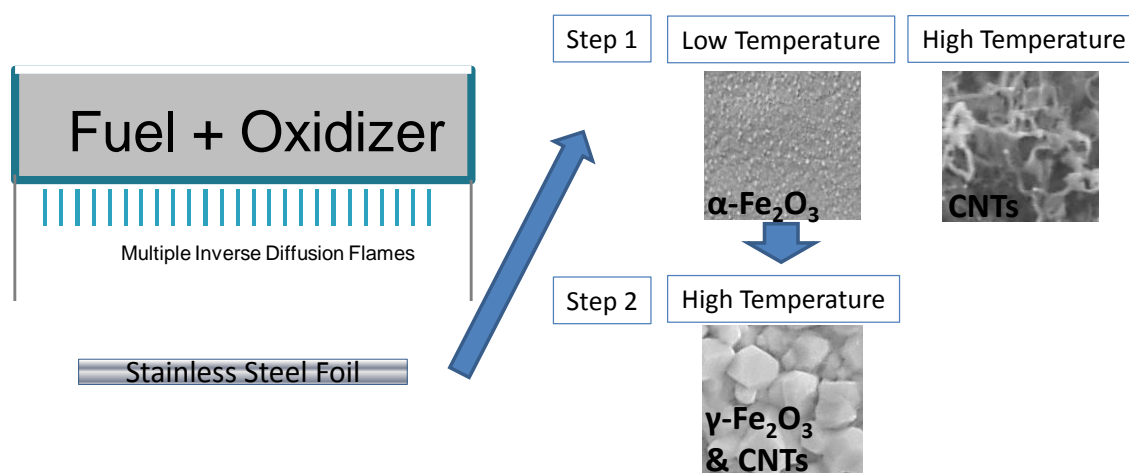


Figure 9.1 Schematic diagram of the experimental setup. The stainless steel substrate is held either at a high temperature (850°C) or a low temperature (500°C).

9.3 Results and Discussion

9.3.1 High Temperature Growth on Stainless-Steel

First the high temperature growth condition is examined on stainless-steel. Previously, under the same conditions, the growth of graphene is observed on copper, nickel, cobalt, and copper-nickel, chapter 5. While the synthesis of graphene on stainless-steel is observed for certain conditions using chemical vapor deposition (CVD) [11,12], the exclusive growth of graphene is not observed using the multiple inverse-diffusion flame for the examined experimental conditions. The growth of CNTs directly on stainless steel has been reported using CVD [13] and flame synthesis [10]. At a growth temperature of 850°C, the growth of micro- and nano-scale carbon fibers and tubes are observed, Figs. 9.2a and 9.2b. Under certain conditions, catalyst particles are formed on the stainless-steel substrate, and carbon-based species within the flame undergo dissociative adsorption and diffuse through the particles resulting in the growth of carbon fibers and CNTs. The high solubility of carbon within Fe results in the formation of Fe_3C and the breakup of the surface [14]. This results in the growth of CNTs rather than graphene. The influence of the growth time is examined using FESEM. After five minute growth, Fig. 9.2c, the dark spots correspond to regions of carbon growth, and it is observed that the substrate is not uniformly covered in CNTs. When the growth time is increased to 20 minutes, Fig. 9.2d, the substrate is uniformly covered with micro- and nano-scale carbon fibers and tubes.

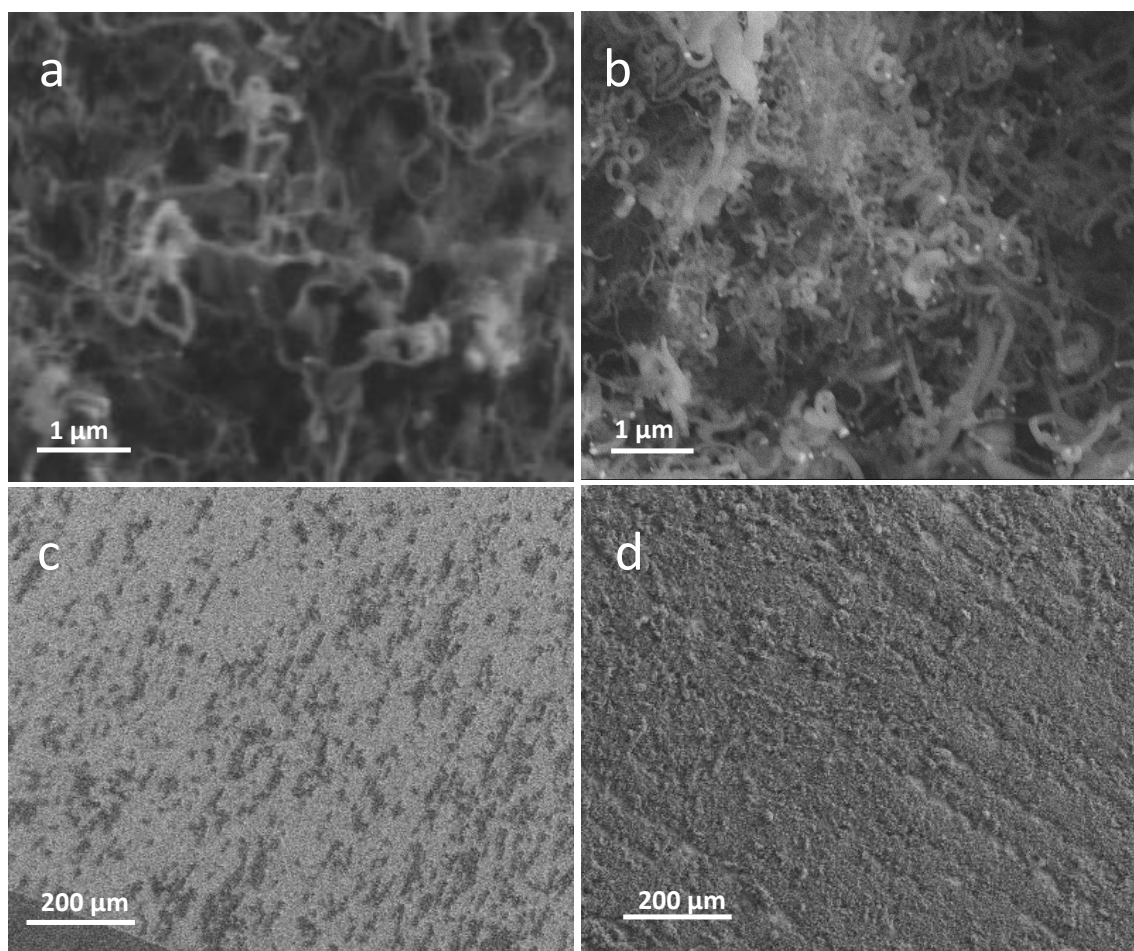


Figure 9.2 Carbon nanomaterial growth on stainless steel at a temperature of 850°C. (a,b) SEM image of the growth of micro- and nano-scale carbon fibers and tubes. (c) The growth after CH₄ is introduced for 5 minutes (dark regions correspond to CNTs). (d) The growth after CH₄ is introduced for 20 minutes.

Raman spectroscopy and XPS is further used to characterize the growth of CNTs on stainless-steel. The D, G, and 2D peak within the Raman spectrum, [Fig. 9.3a](#), confirm the graphitic structure of the CNTs. At high temperatures (corresponding to the CNT growth regime), the C 1s peak (from XPS) is located at ~284.6eV ([Fig. 9.3b](#)), which indicates that most of the atoms are in a sp^2 C state (binding energy 284.4 eV) [15].

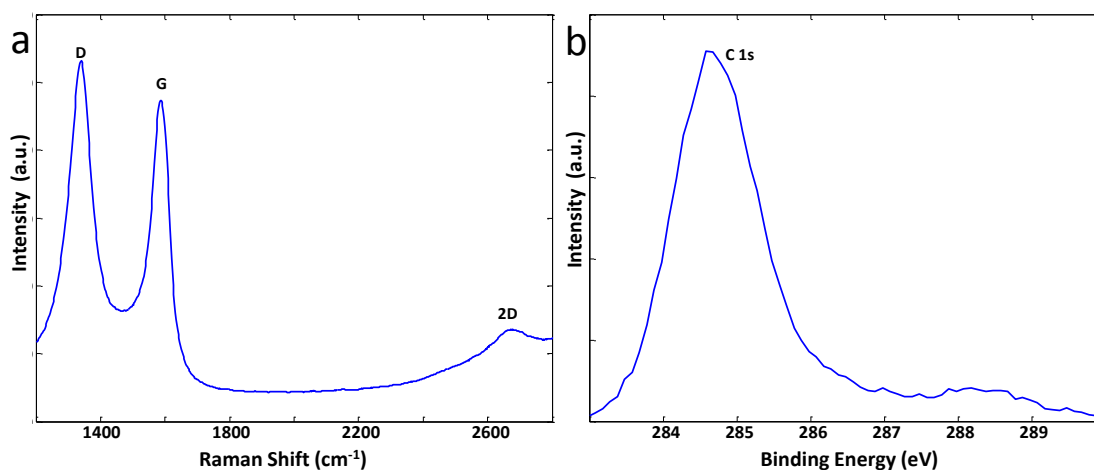


Figure 9.3 (a) Raman spectrum of the high temperature growth condition. (d) XPS spectrum of the of the high temperature growth condition.

9.3.2 Low Temperature Growth on Stainless-Steel

Intriguingly, when the stainless steel temperature is lowered to 500°C , a nanocrystalline iron-oxide film nucleates and grows on the substrate, as shown in Fig. 9.4a. While oxygen is completely consumed using the inverse-diffusion flame, the growth of iron-oxide occurs due to the presence of CO and H_2O within a fuel-rich flame [5,7]. Raman spectroscopy enables the identification of different iron-oxide phases [16-18]. The Raman spectrum taken of the film, Fig. 9.4b, show major peaks at 238, 300, 417, 500, 616, and 1320 cm^{-1} . These peaks are associated with $\alpha\text{-Fe}_2\text{O}_3$ (hematite) and several key features help to distinguish it from other iron phases. Hematite being an antiferromagnetic material has a collective spin movement, which when excited is called a magnon. The strong peak at 1320 cm^{-1} result from a two-magnon scattering that arises from the interaction of the antiparallel spin sites [17]. It is important to note that the 1320 cm^{-1} is commonly mistaken for carbonaceous materials (such as diamond); therefore

it is important to collect the entire spectra between 200 and 1800 cm^{-1} when distinguishing between $\alpha\text{-Fe}_2\text{O}_3$ and carbonaceous materials [19]. The narrow doublet at 238 and 300 cm^{-1} is associated with $\alpha\text{-Fe}_2\text{O}_3$ [16], where slight shifts in the range of 5 to 20 cm^{-1} occur due to different laser powers [17]. Hematite can have various colors [16] and the growth of $\alpha\text{-Fe}_2\text{O}_3$ result in the formation of a yellowish color on stainless-steel, Fig 4a (bottom right inset).

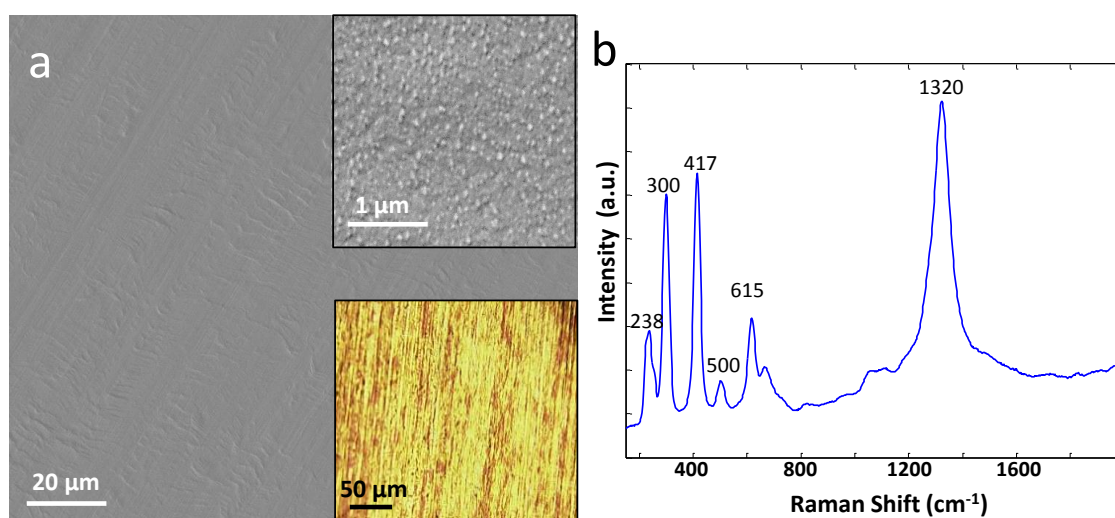


Figure 9.4 Iron oxide growth on stainless steel at a temperature of 500°C. (a) SEM image shows the growth of a nanocrystalline iron-oxide film at 500°C. The top right inset shows a magnified SEM image of the film. The bottom right inset shows an optical image of the film. (b) Raman spectrum confirms the growth of $\alpha\text{-Fe}_2\text{O}_3$.

Further characterization of nanocrystalline $\alpha\text{-Fe}_2\text{O}_3$ is performed using TEM and XPS. The TEM image, Fig. 9.5a, show that the particle sizes are in the range of 20 to 60 nm, however they tend to agglomerate and sinter. The pattern obtained from the selected area electron diffraction (SAED) (Fig. 9.5b) of the particles corresponds to $\alpha\text{-Fe}_2\text{O}_3$. Chemical composition of iron oxide can be distinguished by the XPS analysis of the Fe 2p orbital [20,21]. Peaks for Fe 2p_{3/2} and Fe 2p_{1/2} are located at 710.7 and 724.5 eV,

respectively, Fig. 9.6a. These peaks correspond to the 3+ ion in Fe_2O_3 , as the peaks for the 2+ ion in Fe_3O_4 are located at 709.8 eV ($\text{Fe } 2p_{3/2}$) and 722.8 eV ($\text{Fe } 2p_{1/2}$) [21]. Additionally the identified satellite peaks at 718.9 and 732.8 eV confirm the growth of Fe_2O_3 . Argon ion beam etching is performed for 10 seconds on the $\alpha\text{-Fe}_2\text{O}_3$ coated stainless substrate. XPS results for the etched substrate depict that the satellite peaks are no longer present, Fig. 9.6b, indicating the absence of Fe_2O_3 . Hence only a thin layer (under 5nm) of $\alpha\text{-Fe}_2\text{O}_3$ growth occurs on the substrate.

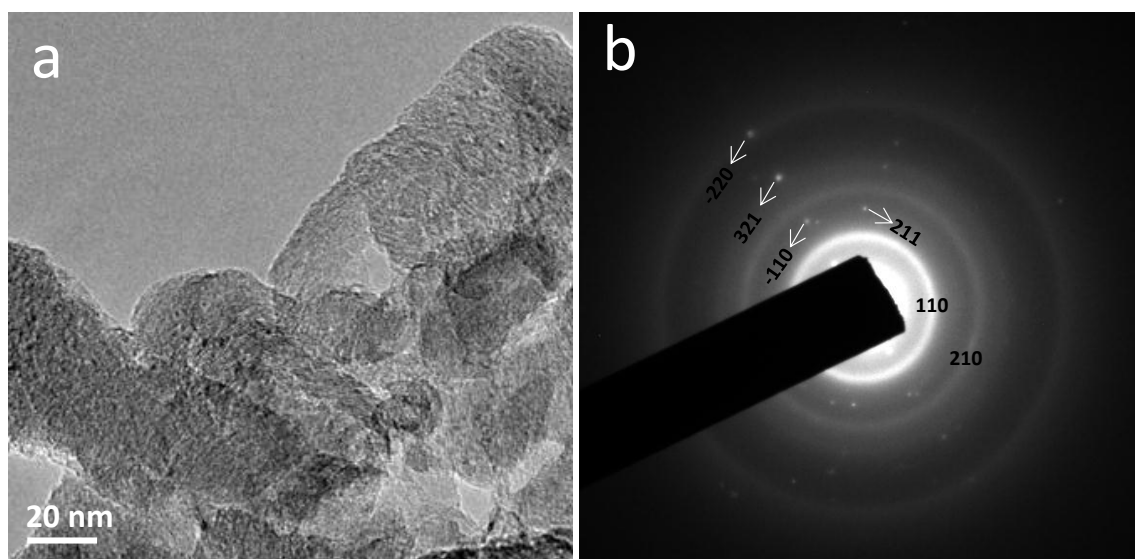


Figure 9.5 (a) TEM image of the iron oxide nanoparticles. (b) SAED confirming the growth of $\alpha\text{-Fe}_2\text{O}_3$.

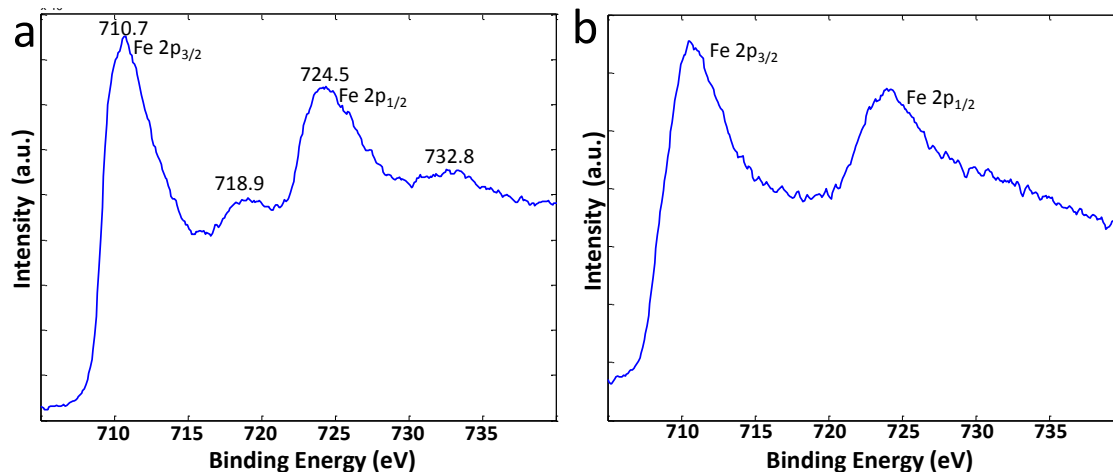


Figure 9.6 (a) Fe 2p XPS spectrum of α -Fe₂O₃. (b) Fe 2p XPS spectrum after argon ion beam etching.

9.3.3 Two-step Growth Process on Stainless-Steel

After a thin film of nanocrystalline α -Fe₂O₃ is grown across the substrate, the temperature is raised from 500°C to 850°C. The growth of larger nanocrystalline iron-oxide, up to 300nm, is observed (Fig. 9.7a). Additionally, the growth of CNTs can occur alongside iron-oxide, as shown in Fig. 9.7b. This result demonstrates the ability to grow hybrid materials of iron-oxide and CNTs, without the need of any additional catalyst on the same substrate. The characterization of the iron-oxide/CNT hybrid structure is performed using Raman spectroscopy, Fig. 9.8a. The peaks at 1350, 1593, and 2700 cm⁻¹ correspond to the growth of CNTs, while the peaks at 553, 687, and 714 cm⁻¹ correspond to the growth of γ -Fe₂O₃. A key feature of the Raman spectrum for γ -Fe₂O₃ is a broad and strong feature at 680-720cm⁻¹ with the presence of a shoulder peak [16]. The transformation from α -Fe₂O₃ to γ -Fe₂O₃ normally occurs in a reducing environment [22-24]. It is possible that the large quantity of hydrogen present within the flame enables the

transformation from α -Fe₂O₃ to γ -Fe₂O₃ and the water vapor enables the growth of larger iron-oxide crystals at high temperatures. The growth of larger iron-oxide crystals is further verified using TEM, Fig. 9.8b. Additionally, HRTEM confirms the commonly observed (313) plane of γ -Fe₂O₃, inset Fig. 9.8b.

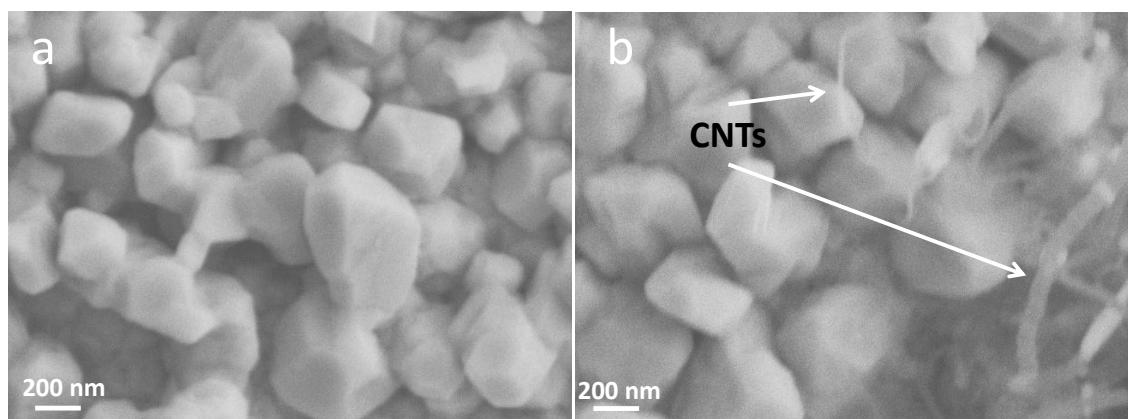


Figure 9.7 Growth on stainless steel after a two-step growth process. (a) The growth of nanocrystalline iron oxide. (b) Hybrid growth of CNTs and iron oxide.

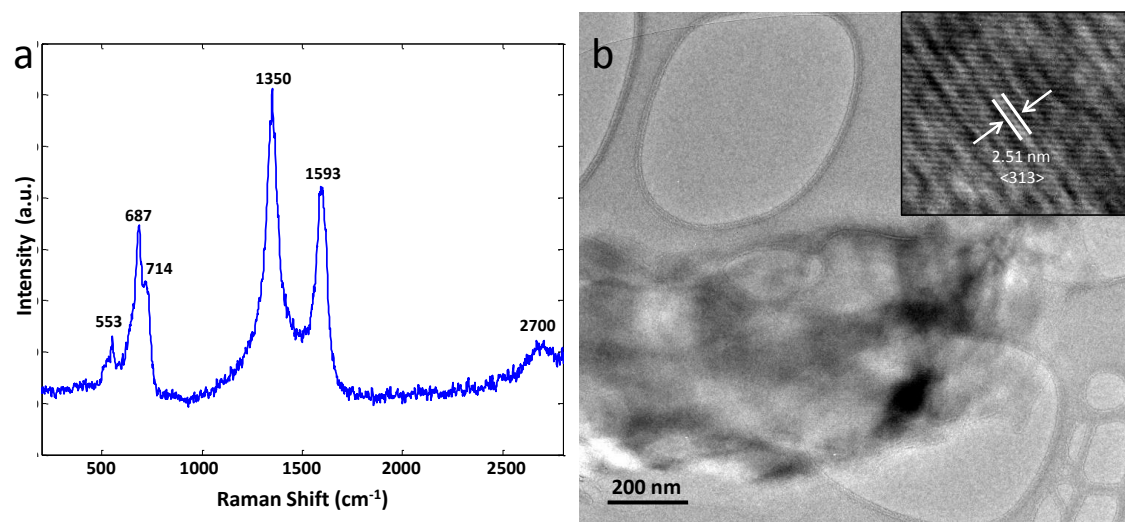


Figure 9.8 (a) Raman spectrum confirming the growth of γ -Fe₂O₃ and CNTs. (b) TEM analysis of the γ -Fe₂O₃ crystal. The top right inset shows a HRTEM image of γ -Fe₂O₃.

9.4 Concluding Remarks

The importance of substrate temperature on the flame synthesis of iron oxide and CNTs is highlighted. By varying the temperature, growth can transition from CNTs to iron oxide. At low temperatures (500°C) the growth of α -Fe₂O₃ is observed, while at higher temperatures (850°C) the growth of CNTs is observed. Additionally, by following a two-step growth process, where the temperature is changed from 500°C to 850°C, the growth of CNTs and γ -Fe₂O₃ occurs. The advantages of our process are tunability to produce CNTs, nano iron-oxide, and their composites; synthesis at atmospheric conditions without a confining chamber; continuous rapid growth process; and efficient and economical use of CH₄, H₂O and H₂ in providing the elevated temperature and species necessary for growth.

9.5 References

- [1] Gupta AK, Gupta M. Synthesis and surface engineering of iron oxide nanoparticles for biomedical applications. *Biomaterials* 2005;26:3995-4021.
- [2] Teja AS, Koh P. Synthesis, properties, and applications of magnetic iron oxide nanoparticles. *Progress in Crystal Growth and Characterization of Materials* 2009;55:22-45.
- [3] Laurent S, Forge D, Port M, Roch A, Robic C, Vander Elst L et al. Magnetic Iron Oxide Nanoparticles: Synthesis, Stabilization, Vectorization, Physicochemical Characterizations, and Biological Applications. *Chem Rev* 2008;108:2064-110.
- [4] W Merchan-Merchan and A V Saveliev and, A.M. Taylor. High rate flame synthesis of highly crystalline iron oxide nanorods. *Nanotechnology* 2008;19:125605.
- [5] D'Esposito C. Investigating local growth conditions in the flame synthesis of metal-oxide nanostructures. Rutgers University 2009.

- [6] Rao PM, Zheng X. Rapid Catalyst-Free Flame Synthesis of Dense, Aligned γ -Fe₂O₃ Nanoflake and CuO Nanoneedle Arrays. *Nano Lett* 2009;9:3001-6.
- [7] Rao PM, Zheng X. Unique Magnetic Properties of Single Crystal γ -Fe₂O₃ Nanowires Synthesized by Flame Vapor Deposition. *Nano Lett* 2011;11:2390-5.
- [8] Zhang W, Xu B, Jiang L. Functional hybrid materials based on carbon nanotubes and metal oxides. *J Mater Chem* 2010;20.
- [9] Zhao X, Johnston C, Grant PS. A novel hybrid supercapacitor with a carbon nanotube cathode and an iron oxide/carbon nanotube composite anode. *J Mater Chem* 2009;19.
- [10] Merchan-Merchan W, Saveliev AV, Kennedy L, Jimenez WC. Combustion synthesis of carbon nanotubes and related nanostructures. *Progress in Energy and Combustion Science* 2010;36:696-727.
- [11] Robin John and A Ashokreddy and C Vijayan and T. Pradeep. Single- and few-layer graphene growth on stainless steel substrates by direct thermal chemical vapor deposition. *Nanotechnology* 2011;22:165701.
- [12] Yuan GD, Zhang WJ, Yang Y, Tang YB, Li YQ, Wang JX et al. Graphene sheets via microwave chemical vapor deposition. *Chemical Physics Letters* 2009;467:361-4.
- [13] Vander Wal RL, Hall LJ. Carbon nanotube synthesis upon stainless steel meshes. *Carbon* 2003;41:659-72.
- [14] Xu F, Zhao H, Tse SD. Carbon nanotube synthesis on catalytic metal alloys in methane/air counterflow diffusion flames. *Proceedings of the Combustion Institute* 2007;31:1839-47.
- [15] Okpalugo TIT, Papakonstantinou P, Murphy H, McLaughlin J, Brown NMD. High resolution XPS characterization of chemical functionalised MWCNTs and SWCNTs. *Carbon* 2005;43:153-61.
- [16] Froment F, Tournié A, Colomban P. Raman identification of natural red to yellow pigments: ochre and iron-containing ores. *J Raman Spectrosc* 2008;39:560-8.
- [17] de Faria DLA, Venâncio Silva S, de Oliveira MT. Raman microspectroscopy of some iron oxides and oxyhydroxides. *J Raman Spectrosc* 1997;28:873-8.
- [18] Oh S, Cook DC, Townsend HE. Characterization of Iron Oxides Commonly Formed as Corrosion Products on Steel. *Hyperfine Interactions* 1998;112:59-66.

- [19] Marshall CP, Marshall AO. Hematite and carbonaceous materials in geological samples: A cautionary tale. *Spectrochimica Acta Part A: Molecular and Biomolecular Spectroscopy* 2011;80:133-7.
- [20] McIntyre NS, Zetaruk DG. X-ray photoelectron spectroscopic studies of iron oxides. *Anal Chem* 1977;49:1521-9.
- [21] Graat PCJ, Somers MAJ. Simultaneous determination of composition and thickness of thin iron-oxide films from XPS Fe 2p spectra. *Appl Surf Sci* 1996;100–101:36-40.
- [22] Aharoni A, Frei EH, Schieber M. Some properties of γ -Fe₂O₃ obtained by hydrogen reduction of α -Fe₂O₃. *Journal of Physics and Chemistry of Solids* 1962;23:545-54.
- [23] Yoshimi Watanabe and Kuniyoshi Ishii and Nobuhiro Ishikawa and Kazuo Furuya and Masaharu Kato. In situ observation of transformation in α -Fe₂O₃ under hydrogen implantation. *Journal of Physics: Condensed Matter* 2002;14:13643.
- [24] Randrianantoandro N, Mercier AM, Hervieu M, Grenèche JM. Direct phase transformation from hematite to maghemite during high energy ball milling. *Mater Lett* 2001;47:150-8.

Chapter 10

10. Concluding Remarks

10.1 Summary of results and conclusion

Over the past few years, graphene and other two-dimensional (2D) nanomaterials, with their remarkable photonic, electrical, and mechanical properties, have attracted significant research interest. A graphene layer of sp^2 -bonded carbon atoms can be folded into zero-dimensional (0D) fullerenes, rolled into one-dimensional (1D) nanotubes, or stacked into three-dimensional (3D) graphite. Flame synthesis, which readily provides high temperatures and precursor carbon species, serves as a scalable method for the production of 0D and 1D carbon nanostructures. In this thesis the growth of graphene using flame synthesis is demonstrated, further establishing the importance of this method in producing carbon nanomaterials at high rates.

The properties of graphene afford a wide range of applications, such as flexible touch panels, thin-film transistors, solar panels, and corrosion resistant coatings. With a unique band structure and bipolar carriers, a gate electrical field can control electrons and holes for usage in field effect transistors [1]. Graphene conductance changes as a function of surface absorption, making it a promising application in sensors to detect molecules. With transmittance and conductance values of $>90\%$ and $30\Omega/\text{sq}$ (sheet resistance) respectively, graphene has the potential to replace indium tin oxide [2] in numerous devices such as liquid crystal displays, solar panels, and EM shields. By way of increased research focused on graphene, new and exciting applications are constantly being uncovered.

Isolating monolayer graphene by microcleaving and discovering its amazing properties have generated intense experimental research on its fabrication. However, widespread use of graphene will require large-scale synthesis methods. Production methods that currently exist include ultrahigh vacuum (UHV), annealing of SiC, and chemical vapor deposition (CVD). CVD, where hydrocarbon gas is pyrolyzed near the substrate at temperatures $\sim 1000^{\circ}\text{C}$, has emerged as the primary method for the production of graphene. Although these techniques can fabricate graphene, the processes are typically expensive, require long processing times, and are limited to confined synthesis.

Flame synthesis of graphene offers several advantages, such as the potential for continuous production at reduced costs. When utilizing combustion, the hydrocarbon gas provides both the high temperature and carbon species necessary for growth, resulting in an efficient and robust process. In our setup, the product gases of multiple inverse-diffusion flames impinge on a substrate, enabling the growth of graphene. Specifically, each distinct flame burns in an inverse mode, where oxidizer is in the center with fuel (e.g. H_2 , CH_4) surrounding it. This novel synthesis configuration offers: (i) establishment of radially uniform properties downstream from the burner, (ii) production of large quantities of hydrogen and carbon-rich species, (iii) complete consumption (and gettering) of oxygen in the reaction zones, (iv) avoidance of instabilities and flame-speed constraints related to premixed flames, and (v) fabrication in open-environments. No visible soot is observed for the experimental conditions examined; in general, inverse diffusion flames (IDFs) tend to soot less than normal diffusion flames (NDF).

Few-layer graphene (FLG) is grown on copper and nickel substrates at high rates using a novel flame synthesis method in open-atmosphere environments. Transmittance

and resistance properties of the transferred films are similar to those grown by other methods, but the concentration of oxygen, as assessed by XPS, is actually less than that for CVD-grown graphene under near vacuum conditions. Substrate material (i.e. copper, nickel, cobalt, iron, and copper-nickel alloy), along with its temperature and hydrogen pretreatment, strongly impacts the quality and uniformity of the graphene films. On Cu, 5 to 8 layers of graphene are grown uniformly across the substrate. Ni offers the advantage of a lower disorder graphene, but the growth is not uniform across the substrate, with formation of wrinkles appearing along the grain boundaries. The graphene quality is slightly higher on Ni compared to that on Co or Cu-Ni alloy. On Fe, no graphene film is found to grow.

Flame synthesis offers the advantage of providing various gaseous carbonaceous species, which can enable the low temperature growth of graphene. The growth of FLG occurs in the temperature range 750-950°C for copper and 600-850°C for nickel and cobalt. In the case of Cu, graphene grows at 750°C, but amorphous carbon develops at 600°C. In all cases examined, higher temperatures produce better quality graphene films. Starting at 500°C, CNTs grow on Ni, Co, and Ni-Cu. CNT yield on Ni-Cu alloy is abundant due to ready breakup of the surface oxide. Hydrogen plays crucial roles in graphene growth by removing oxide layers on and by modifying grain size of the substrate prior to synthesis (without which the graphene film is not uniform and highly disordered), and by facilitating the formation of active species for synthesis, and etching away sp^3 carbon during synthesis to produce high quality graphene films.

For CNT growth, ethylene is used as the fuel source, with a Ni/Cr/Fe, Ni/Ti, or Fe substrate placed in the post-flame region. Transition metals (e.g. Ni, Co, and Fe) and

their alloys are well known to serve as catalysts for CNT growth. Under the right conditions, catalyst nanoparticles are formed, and carbon-based precursor species readily undergo dissociative adsorption and diffuse through the catalyst nanoparticles and grow into CNTs. Using our flame setup, no pretreatment of the substrate is needed; our single-step method induces catalyst nanoparticle formation along with subsequent CNT growth.

The transitional growth between CNTs and graphene films is investigated on nickel and nickel alloys. The input CH_4 to H_2 ratio (1:10) is held constant. For nickel, copper-nickel, nitinol, and Inconel substrates, CNTs grow at 500°C . The transitional growth to few-layer graphene is observed on nickel, copper-nickel, and Inconel by changing the substrate temperature to 850°C . The growth of graphene is not observed on nitinol for the examined experimental conditions.

Graphene films, multi-walled and single-walled carbon nanotubes (MWNTs and SWNTs) are grown directly on spinel solid solutions using flame synthesis. CNT and graphene growth occurs through decomposition of flame-generated carbon precursors (e.g. CH_4 , CO and C_2H_2) over nanoparticles (i.e. Cu, Ni, Co, and Fe) reduced from the solid oxide. The spinels are prepared by a co-precipitation method, and the production process of CNTs and FLG under atmospheric pressure is continuous and energy-efficient. The growth of CNTs occurs on NiAl_2O_4 , CoAl_2O_4 and ZnFe_2O_4 using counterflow diffusion flame and multiple inverse-diffusion flames. MWNTs are observed on NiAl_2O_4 and CoAl_2O_4 , while a mixture of MWNTs and SWNTs are observed on ZnFe_2O_4 . The crystallinity of the spinel solution plays a critical role in the yield and size of the CNTs. Low temperature growth of CNTs at 500°C occurs for NiAl_2O_4 and CoAl_2O_4 , whereas a high temperature of 750°C is required for growth of ZnFe_2O_4 . The growth of graphene

occurs on CuFe_2O_4 using multiple inverse-diffusion flames. Raman spectroscopy confirms the growth of FLG on CuFe_2O_4 , which is similar to the growth of FLG on Cu foil. XPS confirms the limited oxidation of the FLG on CuFe_2O_4 . The as-grown CNTs/FLG and metal-oxide nanocomposites can be further used to prepare dense massive composites, for which the mechanical and electric properties would benefit greatly from the properties of the CNTs or FLG.

When stainless steel foil is used as the substrate material, the growths of CNTs and iron oxide are observed. By varying the temperature, growth can transition from CNTs to iron oxide. At low temperatures (500°C) the growth of $\alpha\text{-Fe}_2\text{O}_3$ is observed, while at higher temperatures (850°C) the growth of CNTs is observed. Additionally, by following a two-step growth process, where the temperature is changed from 500°C to 850°C , the growth of CNTs and $\gamma\text{-Fe}_2\text{O}_3$ occurs. The growth of hybrid materials based on CNTs and metal oxides (such as iron oxide) can be used in various applications such as supercapacitors, lithium batteries, electrochemical sensors, photocatalysts, solar cells, and gas sensors.

The novel non-premixed flame synthesis process is expected to complement CVD-type processes in the growth of graphene and CNTs. Elevated gas-phase temperatures and flame chemistry provide the precursors for growth, making hydrocarbon (as well as doping precursor) decomposition more independent of substrate temperature, offering an additional degree of freedom in tailoring film characteristics. The encompassing quartz cylinder, which prevents oxidizer transport from the ambient, can also serve as a “reactor wall,” whose cooling/heating rate can be tuned to optimize gas-phase chemistry and temperature reaching the substrate for ideal carbon-based

growth. The present setup affords fast growth rates due to innately high flow rates of precursor species; control of temperature and reagent species profiles due to precise heating at the flame-front, along with self-gettering of oxygen; and reduced costs due to efficient use of fuel as both heat source and reagent. Growth is uniform because the configuration produces post-flame gases downstream that are quasi one-dimensional, i.e. radially-uniform in temperature and chemical species concentrations. Finally, the method is scalable and capable of continuous operation in an open-ambient environment, presenting the possibility of large-area processing.

10.2 Suggestions for future work

The growth of single-layer graphene should be further investigated using the multiple inverse-diffusion flame. In principle, the current flame synthesis technique is sufficiently versatile to deposit a single layer of graphene. One of the key parameters is the methane flux, which is documented as being about 2 orders of magnitude less for CVD grown single-layer graphene, when compared to the method in this thesis. The multiple inverse-diffusion flame system is presently optimized for high flow rates (and correspondingly high growth rates at atmospheric conditions). By lowering the pressure, the velocities through the multiple jets will increase, allowing stabilization of the inverse flames at smaller fluxes. As a result, using fluxes that are comparable to CVD graphene, the multiple inverse-diffusion flame should enable the growth of monolayer graphene. However, low pressure minimizes a key advantage of the current method, i.e. open environment processing. Therefore, it is important to investigate other parameters that

can enable a low flux, at atmospheric pressure, and still achieve high-quality monolayer graphene.

Typically CVD synthesis of graphene on transitional metals involves high temperatures (above 850°C), which is critical for hydrocarbon dissociation. In our setup when using methane and hydrogen as the fuel, the post-flame gases are already comprised of relevant carbon-rich pyrolysis species. This could possibly prevent the growth of single layer graphene; therefore, it is important to investigate the synthesis of graphene using a hydrogen flame, with methane introduced further downstream.

Crystal structure and cooling rate can impact the growth of graphene and should be further investigated. Additionally laser-based diagnostics can be used to determine local growth conditions such as species concentrations and temperature.

Alloying or doping of graphene with nitrogen and/or boron should be explored using the multiple inverse-diffusion flame. Precursors such as ammonia (NH_3) can be introduced with the fuel to provide a source of nitrogen. Similarly, borane (BH_3) or borane-ammonia (H_3NBH_3) can be used as a source for boron and/or nitrogen.

Furthermore, it is important to expand on the growth model for graphene in flames and at atmospheric conditions. For example, under atmospheric conditions it is not entirely clear if few-layer graphene is AB-stacked or turbostratic. Also investigation needs to be done to see if the formation of nanocrystalline graphite occurs. Various discussions presented in this thesis are referenced to results and discussions obtained from CVD growth of graphene, whose ultimate fundamental mechanisms may differ for flame synthesis of graphene. Additionally, in-situ experiments related to graphene growth are critical for the further development of CVD and flame synthesis of graphene.

It is hoped that by further exploring the growth of graphene, flame synthesis (or flame-assisted CVD) emerges as a viable complement to conventional-CVD graphene growth, thus further enabling large scale applications of graphene materials. In addition to graphene and CNTs, the multiple inverse-diffusion flame is suitable for the growth of other carbon nanomaterials, such as nanodiamond and fullerenes.

10.3 References

- [1] Novoselov KS, Geim AK, Morozov SV, Jiang D, Zhang Y, Dubonos SV et al. Electric Field Effect in Atomically Thin Carbon Films. *Science* 2004;306:666-9.
- [2] Bonaccorso F, Sun Z, Hasan T, Ferrari AC. Graphene photonics and optoelectronics. *Nat Photon* 2010;4:611-22.

Curriculum Vita

Nasir K. Memon

Education

Rutgers University - New Brunswick, School of Engineering, Piscataway, NJ
Doctor of Philosophy (Ph.D.), October 2012, GPA: 4.00/4.00
Major: Mechanical and Aerospace Engineering

Rutgers University - New Brunswick, School of Engineering, Piscataway, NJ
Master of Science (M.S.), October 2009, GPA: 4.00/4.00
Major: Mechanical and Aerospace Engineering

Cornell University, College of Engineering, Ithaca, NY
Bachelor of Science (B.S.), January 2005, *cum laude*
Majors: Computer Science and Industrial Engineering

Experience

2009 – 2012 Rutgers University, Piscataway, NJ, Combustion Lab

2009 – 2010 Rutgers University, Piscataway, NJ, Teaching Assistant

2008 – 2009 Rutgers University, Piscataway, NJ, Thermal Science Lab

2007 – 2008 New-York Presbyterian Hospital, New York, NY, Analyst

2005 – 2007 PricewaterhouseCoopers, New York, NY, Consultant

Publications

Memon N., and Jaluria Y. Flow Structure and Heat Transfer in a Stagnation Flow CVD Reactor. *Journal of Heat Transfer* 2011; 133(8)

Memon, N., Tse, S., Al-Sharab, J., Yamaguchi, H., Goncalves, A., Kear, B., Jaluria, Y., Andrei, E., and Chhowalla, M., "Flame Synthesis of Graphene Films in Open Environments," *Carbon*, 2011; 49(15):5064–70

Memon, N., Kear, B., Chhowalla, M., and Tse, S., "Role of Substrate, Temperature, and Hydrogen on the Flame Synthesis of Graphene Films" submitted to the *International Symposium on Combustion*.

Memon, N., A., Kear, B., Tse, S., “Transitioning Growth from Carbon Nanotubes to Graphene Films on Nickel Alloys in Open-Atmosphere Flame Synthesis,” Manuscript prepared.

Memon, N., Dunham, S., Xu F., A., Kear, B., Tse, S., “Flame Synthesis of Carbon Nanotubes and Graphene Films using Metal-Oxide Spinel,” Manuscript prepared.

Conferences

Memon, N., Tse, S.D, Al-Sharab, J., Yamaguchi, H., Jaluria, Y., Kear, B., Chhowalla, M. “Novel Flame Synthesis of Graphene Films .” *Materials Research Society Fall Conference, Boston MA, Nov 28 - Dec 2, 2011.*

Memon, N., Tse, S., Chhowalla, M., Kear, B., Jaluria, Y., “Flame Synthesis of Few-Layer Graphene.” *ASME International Mechanical Engineering Congress Conference, Denver CO, Nov 11 - 17, 2011.*

Memon, N. “Flame Synthesis of Graphene Films for Transparent Electrodes.” *Nanotechnology for Clean Energy IGERT Symposium, Piscataway NJ, Sep. 2011.*

Memon, N., Al-Sharab, J., Jaluria, Y., Kear, B., Chhowalla, M. and Tse, S.D. “Flame Synthesis of Nanostructured Carbon.” *2011-TPC-1232, The Twenty-First (2011) International Offshore (Ocean) and Engineering Conference, Maui, HI, Jun 19-24, 2011.*

Memon, N., Al-Sharab, J., Jaluria, Y., Kear, B. and Tse, S.D. “Scalable Flame Synthesis of Carbon Nanotubes on Substrates.” *Materials Research Society Fall Conference, Boston MA, Nov 29 - Dec 3, 2010.*

Memon, N. “Flame Synthesis of Carbon Nanomaterials as Supercapacitor Electrodes.” *Nanotechnology for Clean Energy IGERT Symposium, Piscataway NJ, Sep. 2010.*

Awards/Patents

National Science Foundation (NSF) Fellowship, IGERT Nanotechnology for Clean Energy, Sept. 2010 - Aug. 2012.

Provisional patent application: Scalable Flame Synthesis of Carbon-Based Nanostructures and Films on Substrates